

Time Series Searching, Forecasting, and Classification 1
with Applications in Bioinformatics 2
時系列の探索・予測・分類とその生命情報学へ 3
の応用 4

Coleman Yu 5
余 浩旻

Abstract

7

Time series data are ubiquitous across many different fields. Much of the data are inherently time series data. Additionally, some data, such as strings, images, and object shapes, that are not originally time series data, can be transformed into time series. Many data mining tasks, such as classification, clustering, and motif finding, have been defined for time series data. Hence, by developing appropriate transformation methods, we can apply a plethora of well-established time series methods to our problems.

This thesis contributes three aspects in time series data mining and bioinformatics. They are a novel application of time series classification to solve complex biological problems by transforming biological data into time series and developing a more expressive distance measure framework that removes certain underlying assumptions.

In the first part, we demonstrate the utility of time series analysis in bioinformatics by studying the problem of predicting Human Dicer Cleavage Sites. Recall that bioinformatics operates at the intersection of **biology**, **biotechnology**, and **informatics**. In this work, we formulate a specific **biology** problem, which is predicting Human Dicer Cleavage sites in microRNA biogenesis, into a machine learning framework. In particular, this is a multivariate time series classification problem, which is the **informatics** component of bioinformatics. Due to current limitations in **biotechnology**, we are constrained to using 1-D RNA sequence inputs rather than 2-D or 3-D data, because these are more expensive to obtain. We propose MTSCCleav, a method that encodes RNA sequences and the probabilities of base pairs in predicted secondary structures into time series data. To the best of our knowledge, we are the first to make use of the probabilities of base pairs in this kind of classification task on RNA data. By doing this, we frame the problem of predicting Human Dicer Cleavage sites into a Multivariate Time Series Classification (MTSC) problem. Existing approaches rely on opaque deep neural networks or complex feature engineering. They are slow, and the feature engineering is over-designed. In contrast, our approach is simple, intuitive, and computationally efficient. The proposed transformation methods allow us to use any well-established time series tools to analyze this biological problem. Experiments demonstrate that MTSCCleav achieves comparable and even better accuracy to state-of-the-art methods while delivering a 3.7X to 28.8X speedup. Furthermore, our perturbation experiments reveal that regions near the cen-

38 ter of pre-miRNAs are essential for cleavage-site prediction, consistent with the existing
39 literature.

40 In the second part, we address the limitations of existing similarity measures. Simi-
41 larity search is a core subroutine in time series data mining tasks. For example, recent
42 studies show that a simple 1-NN classifier with an appropriate distance measure can out-
43 perform many advanced, complicated methods. While Dynamic Time Warping (DTW)
44 and Uniform Scaling (US) are prevailing measures for handling local distortions and
45 global scaling, respectively, and some studies have demonstrated that combining both
46 DTW and US is necessary to obtain meaningful results. Current approaches apply a
47 single scaling factor to the entire sequence. We argue that since distinct phases of a pro-
48 cess often evolve at different speeds, a single scaling factor is insufficient. We introduce
49 the first distance measure framework, namely PSD, that achieves invariance to multiple
50 scaling factors. We also provide speed-up techniques to enable efficient computation of
51 the PSD. Experiments show that PSD better reflects the similarity between time series
52 with multiple phases, and that the identified phases (segmentation) provide a clearer
53 understanding of the data.

54 In the third part, we study a time series primitive, namely matrix profile, in the
55 application of time series forecasting. For a given time series T and an integer m , the
56 matrix profile provides the information about (1) the location of its nearest neighbor
57 and (2) the distance between it and the nearest neighbor of **each** m -subsequence in T .
58 Obviously, the matrix profile also provides us the information for the k -nearest neighbors
59 of each subsequence simply by running the same algorithm for k times. In our application,
60 we are only interested in the left nearest neighbors of each subsequence because they
61 refer to the historical occurrences. We can obtain the immediate subsequences of these
62 historical occurrences as covariates to feed into the forecaster to improve its accuracy.

63 Collectively, this thesis advances the fields of time series data mining and bioinfor-
64 matics by demonstrating the use of time series analysis to address fundamental biological
65 questions and proposing a new, more expressive distance measure framework.

Acknowledgements

66

To begin, I want to express my deepest gratitude to my PhD supervisor at Kyoto University, Prof. Tatsuya Akutsu. I thank him for his kindness and patience. He is a brilliant researcher who can explain complex concepts simply. In a seminar, he showed that simply using clear notation makes presentations much easier to follow. More importantly, he helps students when they are in “valleys” in their lives. When a car is off track, it needs a push—so do people. I am equally indebted to my MPhil supervisor at The Hong Kong University of Science and Technology (HKUST), Prof. Raymond Chi-Wing Wong. He has continued to help and advise me even after I graduated from HKUST.

Akutsu-sensei taught me the importance of reading good materials. In the weekly seminars, he organized reading seminars, assigning some of his favorite books for us to read and discuss. His favorite book is “Probability and Computing” by Mitzenmacher and Upfal. Additionally, through the journal club he organized, students were asked to present the core ideas from their ten selected papers published in leading venues, such as Nature, Science, Cell, and PNAS. Reading beyond my fields helped me identify research gaps others missed. I think some great ideas are born when we merge the ideas from different fields. He also emphasized the importance of mathematics and proof. It is what computer scientists can stand out in the field of bioinformatics. I think it becomes especially true now, since advances in AI make it possible for almost everyone to code (i.e., Vibe coding). He advised me to use the existing tools, libraries, and studies to leverage my own research. He also taught me that a good researcher must master both oral and written presentation; otherwise, others may misinterpret your talent and the effort you put in. When we are reading a paper, he urges us to identify the novelty and analyze the pros and cons of the paper.

Raymond taught me the power of focus and “First Principles”. I was always surprised that he did not use reference management software like Zotero, preferring to annotate hard copies and even type .bib files manually. He told me that when he starts to do research, he will print out the papers and get focused on the stack of papers (hard copies) in front of him. I am not saying it is beneficial not to use tools, but I want to emphasize the power of focus that underlies his work routine. He taught me that every good research starts with a set of good papers. He also emphasized that there is no right or wrong in research, only what you choose to do about it. His research receipt works as follows. When you

98 are tackling a problem, you first review the relevant existing studies to understand the
99 state of the art (SOTA) for it. If the existing work addresses your particular problem,
100 you can apply and adapt it to your problem setting. But most of the time, since your
101 problem must be a particular version of a general problem, the existing general solution
102 should not work well for it. It means that you have some room to improve it. And this
103 is the research gap!. It reminds me of when we deal with the NP-complete problem.
104 As Kleinberg and Tardos's Algorithm Design (Chapter 10) suggests, an NP-complete
105 problem (assuming $P \neq NP$) does not allow us to have an algorithm that possesses
106 all three of the following desired properties simultaneously: Efficiency, Correctness, and
107 Generalization. Hence, it is sometimes preferable to address a specific instance of the
108 problem rather than the general one. He also emphasized the theory. He consistently
109 noted that you need to add theory to the paper to strengthen it. He always mentioned
110 that you need three motivations (why you are doing it) and three contributions (what you
111 have done). Sometimes, I ask why he can write so fast, and he replies, "If you know what
112 you are doing, then you write fast.". He also taught me that when you don't know some
113 of the ideas, you just go back to the original idea. Doing a "deep first search" can help
114 you reach the first principle, a concept that Elon Musk, one of the greatest entrepreneurs
115 of our time, always emphasized. Without these two supervisors, I would not have made
116 it this far. I could not have finished this program.

117 I would like to take this opportunity to share some of my thoughts on my PhD journey.
118 I hope the readers may learn something from what I have gone through. My PhD journey
119 was, to quote Dickens, "the best of times and the worst of times", and to quote Churchill,
120 "This was their finest hour". For the best parts, it allows me to explore both in my daily
121 life and in my research. I tried many things, walked many roads, drank many colas and
122 alcohol, and met many people. This helped me see problems from new perspectives.
123 Regarding the worst parts, I am reminded of a quote from one of my favorite movies,
124 "Les Choristes": "Fond de l'étang". It literally means "Bottom of the Pond". At times, I
125 felt like a frog at the well's bottom, trying hard to get out. Research is fun but also hard.
126 Research is about exploring something new. It is about publishing (so others can learn
127 from it). When I am stuck, the best solution is to aim for a reachable, well-defined goal.
128 The goal should be clear, with obvious rewards and requirements. Also, make sure the
129 effort of your actions can be accumulated. Like the frog, do not jump randomly, but aim
130 to move to stable platforms towards escape. Then, each jump matters for your progress.
131 Two of the materials helped me; they are "Eat the Frog!" and "THE PH.D. GRIND".

132 I would like to thank my thesis committee members. I would like to acknowledge
133 Tamura-sensei and Mori-sensei (a former member) of the Akutsu laboratory. Tamura-
134 sensei taught me to focus on the input-output relationship when encountering new algo-
135 rithms/methods, and Mori-sensei introduced me to the fascinating application of time-
136 series analysis to gene expression data, especially in trajectory inferences (i.e., pseudo-

time). I would like to thank the many communities that made my life in Japan colorful. 137
Thank you to the people of the dormitories where I lived at the Uji and Yoshida cam- 138
puses. I am grateful to my Japanese language teachers. I also cherish the friends I met 139
through Akutsu’s laboratory and the extracurricular activities, including Kendo, Table 140
Tennis, Naginata, Karate, and Aikido. I also met many interesting people from various 141
international student events. 142

I am honored to receive the Asian Future Leaders Scholarship Program (AFLSP) 143
scholarship to support my studies in Japan. I have made a great choice by enrolling in 144
Kyoto University Design School, which has provided me with many valuable interdisci- 145
plinary experiences and opportunities to meet people outside my field. In this program, 146
I have conducted fieldwork in Okinawa, Hong Kong, and Bali, a rare opportunity for 147
researchers in computer science. I would also like to thank the Institute for Chemical 148
Research (ICR) for the Research Assistant position in the Akutsu laboratory. 149

Finally, I would like to express my deepest gratitude to my family and my friends who 150
have stayed by my side with their countless acts of support; I have nothing to return to 151
them but my love and time. 152

A special acknowledgment goes to my niece. As you grow up, I hope you explore the 153
world and fulfill your eagerness for knowledge. Find materials that interest you. One 154
day, you might find this thesis online and, I hope, find it worth reading and inspiring. 155

List of Publications

156

This thesis is based on the following papers.

157

- (Chapter 3) **Coleman Yu**, Raymond Chi-Wing Wong, and Tatsuya Akutsu, “MTSC-Cleav: a Multivariate Time Series Classification (MTSC)-based Method for Predicting Human Dicer Cleavage Sites”, submitted to *IEEE Access*, under review 158
159
160
 - (Chapter 4) **Coleman Yu**, Tatsuya Akutsu, and Raymond Chi-Wing Wong, “Scaling with Multiple Scaling Factors and Dynamic Time Warping in Time Series Searching”, submitted to *IEEE Access*, under review 161
162
163
 - (Chapter 5) **Coleman Yu**, Raymond Chi-Wing Wong, and Tatsuya Akutsu, “Leveraging Nearest Neighbors for Time Series Forecasting with Matrix Profile”, in preparation 164
165
166
- Other publications 167
- **Coleman Yu** and Raymond Chi-Wing Wong, “A Melody Composer for both Tonal and Non-Tonal Languages”, the 43rd International Computer Music Conference 2017, Shanghai, China on 16-20 Oct, 2017 168
169
170
 - In this study, we apply a data mining method called frequent pattern mining to capture the relationships between the pitch trend in the melody and the tone trend in lyrics and use these relationships to create a new melody for the user-given lyrics. The pitch trend and the melody trend are both time series data. It motivates me to do time series analysis from a data mining perspective. 171
172
173
174
175
176
 - Yi Zheng, Bogdan Enescu, Jiancang Zhuang, and **Coleman Yu**, “Data replenishment of five moderate earthquake sequences in Japan, with semi-automatic cluster selection”, *Earthquake Science*, 34:310-322, 2021 177
178
179
 - In this study, we apply a data mining method called DBSCAN, which is a clustering method, on seismicity data, to automatically select the nearest significant earthquake cluster of a given mainshock. The clustering results are 180
181
182

183 then fed into a downstream replenishment method to discover missing early
184 aftershocks, which follow relatively large or moderate earthquakes.

185 Poster presentations

- 186 • **Coleman Yu** and Tatsuya Akutsu, “Aligning gene expression time series with
187 invariance to uniform scaling with multiple scaling factors”, International Workshop
188 on Bioinformatics and Systems Biology, Boston, USA (IBSB 2018) on 16-18 July,
189 2018

190 – In this study, we present an idea that, for time series analysis, rather than
191 focusing on the whole sequence analysis, it is more important to focus on
192 the subsequences of a time series. In this poster, we use gene expression
193 data as an example to explain. Genes are expressed over time. But the
194 expression rate is not a constant. The varying rate would be discussed in
195 Chapter 4. The importance of the subsequence has been discussed in the
196 framework of time series forecasting in Chapter 5. We use a data mining
197 primitive called Matrix Profile. Given a subsequence Q with length m , we
198 can find the nearest neighbor (location and the similarity of it with Q) in
199 another time series A . The underlying distance metric is z-normalized ED.
200 If Q is an m -subsequence extracted from A , it means that we annotate each
201 m -subsequence with its nearest neighbor information. To demonstrate that
202 this nearest-neighbor information is useful, we use it to improve a time-series
203 forecasting model. If information is useful covariates, the performance can
204 be improved. In addition, the usage of finding useful covariates to improve
205 the final prediction results has also been demonstrated in Chapter 3. In that
206 example, we find a covariate, which is the secondary structure, associated with
207 the probability of each base pair, for the mRNA sequence data, as shown in
208 Figure 3.1.

Contents

209

Abstract	i	210
Acknowledgements	iii	211
List of Publications	vii	212
List of Figures	xiii	213
List of Tables	xv	214
1 Introduction	1	215
1.1 Background	1	216
1.2 Contributions	2	217
1.3 Organization	2	218
2 Preliminaries	3	219
2.1 Distance Measures	3	220
2.1.1 Euclidean Distance (ED)	4	221
2.1.2 Dynamic Time Warping (DTW)	4	222
2.1.3 Derivative Dynamic Time Warping (DDTW)	5	223
2.1.4 Weighted Dynamic Time Warping (WDTW)	5	224
2.1.5 Weighted Derivative Dynamic Time Warping (WDDTW)	6	225
2.1.6 Shape Dynamic Time Warping (shapeDTW)	6	226
2.1.7 Amercing Dynamic Time Warping (ADTW)	6	227
2.2 Classification	7	228
2.2.1 Ridge Classifier	7	229
3 MTSCCleav: a Multivariate Time Series Classification (MTSC)-based Method for Predicting Human Dicer Cleavage Sites	9	230
3.1 Background	10	232
3.2 Methods	12	233
3.2.1 Data Preparation	13	234

235	3.2.2	Time Series Encoding	16
236	3.2.3	Time Series Classification	19
237	3.2.4	Evaluation Metrics	23
238	3.3	Results	24
239	3.3.1	Channel Ablation Study	25
240	3.3.2	Predictive Performance	26
241	3.3.3	Running Time Analysis	28
242	3.3.4	Subsequence Importance	29
243	3.3.5	Summary	30
244	3.4	Discussion	30
245	3.5	Concluding Remarks	31
246	4	Scaling with Multiple Scaling Factors in Time Series Searching	33
247	4.1	Background	34
248	4.2	Related Work	37
249	4.3	Preliminaries	37
250	4.3.1	Euclidean Distance (ED)	38
251	4.3.2	Dynamic Time Warping (DTW)	39
252	4.3.3	Uniform Scaling (US)	41
253	4.3.4	Uniform Scaling & Dynamic Time Warping (USDTW)	42
254	4.3.5	Lower Bounds for DTW and USDTW	43
255	4.4	Piecewise Scaling Distance	46
256	4.4.1	Piecewise Scaling & Dynamic Time Warping (PSDTW)	47
257	4.4.2	Speedup Techniques	49
258	4.4.3	Guided Distance	54
259	4.5	Experiments	54
260	4.5.1	Experimental Setup	54
261	4.5.2	Experimental Results	57
262	4.6	Concluding Remarks	60
263	5	Leveraging Nearest Neighbors for Time Series Forecasting with Matrix Profile	63
264	5.1	Background	63
265	5.2	Related Work	66
266	5.3	Method	67
267	5.3.1	Problem Formulation	68
268	5.3.2	Evaluation Method	68
269	5.3.3	Gradient Boosting Regression Tree (GBRT)	70
270	5.3.4	Matrix Profile	71

5.4	Experiments	71	272
5.5	Concluding Remarks	72	273
5.5.1	Future Work	72	274
6	Conclusion and Future Directions	75	275

List of Figures

276

2.1 Alignments.	4	277
3.1 Predicted secondary structure of the sequence S of pri-miRNA “hsa-let-7a-1” ¹ . Experimental evidence suggests that the two deviated mature miRNAs are $UGA \cdots GUU$ and $CUA \cdots UUC$. They are $S(6 : 27)$ and $S(57 : 77)$ (Both ends are inclusive.). The ends are highlighted in bold . Since $S(6 : 27)$ ($S(57 : 77)$) is near the 5' (3') end, we call it “5p (3p) mature miRNA”. The two scissors indicate the two cleavage sites. The color intensity of the nodes reflects their base-pair probability in this predicted secondary structure. The deeper the color, the higher the probability. The unpaired nodes are uncolored. The raw figure is generated by RNAfold web server ²	11	287
3.2 The overall pipeline of this study. Symbol notations: Cylinder - Dataset, Rectangle - Process, Parallelogram - Input / Output, Rounded Rectangle - Component.	13	290
3.3 Relationship of the proposed encoding methods.	16	291
3.4 Features generation in the transformation	20	292
3.5 Convolutions of HYDRA for each input time series with a set of random kernels w , organized into g groups with k kernels each.	21	294
3.6 CD diagrams of channel ablation study.	26	295
3.7 CD diagrams to compare different classifiers.	27	296
3.8 CD diagrams to compare different encoding methods.	28	297
3.9 Results of the perturbation experiment.	30	298
4.1 Applying nearest neighbor interpolation on Q , which result in Scaled Q , that can better reflect its similarity with C	35	300
4.2 Q and C are in different rates. A stretching version of Q is similar to a prefix of C , but not the whole C	35	302
4.3 Intuition of piecewise scaling (PS).	36	303
4.4 Z-normalization. Resulting time series have mean = 0 and std = 1.	38	304
4.5 Visualization of D with local constraints. The black cells form the warping path.	40	305

307	4.6	Visualization of LB _{Keogh} and LB _{Shen}	44
308	4.7	Relationship of L_Q and L_C	51
309	4.8	Visualization of the GunPoint dataset. Left (Right): A time series of the “Gun” (“Point”) scenario. Critical periods, such as “Aiming”, are annotated.	55
310	4.9	The red solid time series shows an instant in the target set. The blue dashed time series shows an instant in the query set.	55
311	4.10	Runtime and number of distance calls comparison of GunPoint dataset.	
312	(a)-(d)	$P = 1$, (e)-(h) $P = 2$, (i)-(l) $P = 3$	59
313	5.1	Flattening a 2D window of size $(1 + M) \times w$ to a 1D vector of length $w + M$. The resulting vector serves as the <i>predictor</i> for the regressor. Its expected <i>response</i> is the vector of length h . The regressor learns from this predictor-response pair.	64
314	5.2	The left (right) matrix profile and the matrix profile of a time series. The matrix profile shows the distances between each m -subsequence and its nearest neighbor, where m is a user-given value. The left (right) matrix profile shows the same information but is limited to its left (right) nearest neighbor. For a particular m -subsequence shown by the right gray box, its nearest neighbor is the left gray box, as indicated by the dashed line in the left matrix profile and the matrix profile . Similarly, the nearest neighbor of the left gray box is the right gray box, as indicated by the dashed line in the right matrix profile and the matrix profile . The first (last) point in each box is denoted by a red circle (triangle). h denotes the length of the immediate subsequence of the nearest neighbor. Intuitively, this subsequence should be similar to the immediate subsequence (i.e., future) of the right gray box. To note, the left (right) matrix profile starts (ends) at a later (earlier) index because the corresponding nearest neighbor with length m does not exist.	65

List of Tables

334

3.1	Selected representative records from miRBase. For the last two columns, the first line shows the name, the second line shows its location in the original sequence, and the third line indicates whether its existence has experimental evidence. The selected one is highlighted in bold	335
		336
		337
13		338
3.2	The whole sequence of “hsa-let-7a-1” and its predicted secondary structure by RNAfold. The corresponding positions of the two mature miRNAs and the probability of the unpaired “U” are highlighted in bold	339
		340
14		341
3.3	The first row shows the “four strings” of “hsa-let-7a-1”. Their complementary strands are shown in the second row. As a whole, they are referred to as the “eight strings”.	342
		343
15		344
3.4	Time series encoding. P is the corresponding base-pair probability sequence of S . $p_i = 1$ if we encode S without incorporating base-pair probability sequence.	345
		346
18		347
3.5	Comparison of rocket-based classifiers [1]. $\mathcal{N}(0, 1)$: a standard normal distribution, $U(0, 1)$: a uniform distribution between 0 and 1, 1 st order difference: $\Delta T = t_2 - t_1, t_3 - t_2, \dots, t_n - t_{n-1}$	348
		349
23		350
3.6	Channel ablation study. The best results are highlighted in bold	351
3.7	Performance on the 45 combinations between encoding methods and the ROCKET-based classifiers. The best results are highlighted in bold	352
27		353
3.8	Comparative analysis between MTSCCleav with the best combination of the encoding method and classifier, with the SOTA, DiCleave, on the three datasets. The best results of using MiniROCKET have also been shown to compare the computational efficiency. The best results are highlighted in bold	354
		355
		356
		357
28		358
4.1	Details of the ten datasets for the experiments	359
4.2	The accuracy comparison for eight distance measures of the GunPoint dataset	360
57		361
4.3	The accuracy comparison for six PSED-guided distance measures of the GunPoint dataset	362
58		363
4.4	The accuracy comparison for eight distance measures of the ten datasets	364

365	4.5 The accuracy comparison for six PSED-guided distance measures of the	
366	ten datasets	60
367	4.6 The number of distance calls and runtime on PSED_vanilla and PSED_parallel_bsf	
368	of the ten datasets	61
369	5.1 Dataset Statistics. N is the number of time series in the dataset, while	
370	$ T = n$ is the length of each time series. “rate” refers to the measuring	
371	rate. w is the size of the look-back window. h is the size of the forecasting	
372	window, also known as the forecasting horizon. T_{train} is the training subse-	
373	quence of T . T_{test} is the test subsequence of T . To note, $ T_{\text{train}} + T_{\text{test}} = n$.	
374	71

Chapter 1

375

Introduction

376

1.1 Background

377

Human generates a ton of data nowadays. We are producing more new data in one single day today than in the first twenty-one centuries of AD combined. We are drowning in information but thirsty for knowledge. It is natural for us to develop computational methods to accelerate the process of “harvesting” knowledge from information.

378

379

380

381

Computational tasks focus on the relationship between input and output. We would like to find the hidden function behind. To note, there are two ways to solve a problem. One is the algorithmic approach, and the other is the machine-learning approach.

382

383

384

There are two large categories of machine learning. They are supervised learning and unsupervised learning. Classification may be the most intuitive form of supervised learning. The input is data points with labels. We learn a model from the relationship between data points and the labels. The model predicts the labels for the new data points. They have many applications. For example, in medical applications, it involves classifying patients as healthy or diseased, or tumors as benign or malignant. The term “supervised” means the model has access to labeled data. In other words, it requires labeled training examples that provide ground truth. So, the model can learn the boundary between the categories. Our first study focuses on a classification problem in biology.

385

386

387

388

389

390

391

392

393

A representative of unsupervised learning is undoubtedly clustering. We aim to group data into distinct clusters. The key difference is that the data lack predefined labels. By grouping them, we aim to identify natural patterns hidden in the data. One example is clustering cells based on their gene-expression profiles. These clusters might reveal distinct cell types. Note that we do not have the ground truth for the cluster set. In bioinformatics, we typically use enrichment analysis to determine whether specific gene functions are enriched in these clusters. Cell types often show enrichment for genes responsible for specific functions. This set of genes defines their biological role. In clustering, we first need to define a measure of similarity between two objects. And

394

395

396

397

398

399

400

401

402

403 what should be ignored. This is called invariance. For example, in image classification,
404 it should be invariant with respect to the zooming effect and the rotation effect. In
405 Chapter 4, we define a new distance measure framework that achieves invariance when
406 two time series are in different scaling factors.

407 1.2 Contributions

408 In this study, our contributions mainly include three parts. In Chapter 3, it demonstrates
409 a machine learning approach to analyze a biology problem. In Chapter 4, we solve an
410 algorithmic problem on distance measure. In Chapter 5, we improve a forecaster with
411 the usage of a data mining primitive, namely Matrix Profile. First, we propose the
412 usage of the base pair probability sequence from the predicted secondary structure of
413 RNA sequence as a new information for the classification task. We apply Rocket-based
414 classifiers to identify the human dicer cleavage sites. Because of the simplicity of the
415 transformation method and the classifiers, our proposed method achieves 3.7X to 28.8X
416 speedup while achieving better or comparable results than the current state-of-the-art
417 method. Second, we propose a new distance measure framework, namely PSD, that
418 can incorporate any existing distance measures to achieve invariance for two time series
419 with multiple rates. Experiments show that our methods outperform ED, DTW and
420 the other five DTW-based methods. Besides, we propose to use the segmentation result
421 returned by PSD to improve the accuracy of other distance measures. Third, we propose
422 leveraging left nearest neighbors for each forecasting window as new covariates to improve
423 the accuracy of the underlying forecaster. We use a simple gradient boosting regression
424 tree as the underlying forecaster. Experiment shows that this simple method can improve
425 the accuracy.

426 1.3 Organization

427 In Chapter 2, we review some of the basic knowledge in biology and time series data
428 mining, in particular, we focus on distance measures and Rocket-based classifiers. In
429 Chapter 3, we introduce our study of the problem of predicting human dicer cleavage
430 sites. We proposed a novel approach to frame this task as a multivariate time series
431 classification problem by introducing nine encoding methods and making use of Rocket-
432 based classifiers. In Chapter 4, we introduce a new distance measure framework, namely
433 PSD. It releases the assumption that there is only one scaling factor existing throughout
434 the whole time series. In Chapter 5, we introduce how to create new covariates in time
435 series forecasting using matrix profile. This method can improve the accuracy of the
436 existing forecaster by providing useful covariates. In Chapter 6, we give a conclusion to
437 these two studies and provide future work on them.

Chapter 2

438

Preliminaries

439

In this chapter, we provide background on time series, with a focus on distance measures 440
and classification, particularly the ridge classifier, which is used in the ROCKET-based 441
classifiers for time series classification. The remaining preliminary knowledge will be 442
provided in the corresponding chapters. Section 2.1 gives an overview of the existing 443
distance measures used in the evaluation in Chapter 4. Section 2.2 reviews the additional 444
knowledge about the classifiers used in Chapter 3. We start with the definition of a time 445
series. 446

2.1 Distance Measures

447

A general form of a time series T is an ordered pair of n real-valued variables, $T = 448$
 $(b_1, c_1), (b_2, c_2), \dots, (b_n, c_n)$, where b_i is the behavioral attribute and c_i is the contextual 449
attribute, where $1 \leq i \leq n$. c_i refers to the time stamp at which the measurement b_i 450
is taken. Since the measurements are always taken in a uniform manner, t_i is simply 451
incrementing from 1 to n uniformly. Hence, we can represent a time series more concisely 452
as $T = t_1, t_2, \dots, t_n$, where $t_i = b_i$. 453

We may be interested not only in the entire time series but also in a segment of it, 454
called a subsequence. A subsequence $T(i : j)$ of a time series T is a shorter time series, 455
which is a contiguous subset of time points in T , that starts from position i and ends at 456
position j . Formally, $T(i : j) = t_i, t_{i+1}, \dots, t_j$, where $1 \leq i \leq j \leq n$. We call $T(1 : m)$ as 457
the prefix of length m of T , m -prefix in short. 458

To quantify the similarity between two time series, we need to define a distance 459
measure, also known as a similarity measure, between them. Many distance measures 460
have been proposed in the literature. Among them, the most established measures are 461
undoubtedly Euclidean Distance (ED) and Dynamic Time Warping (DTW). They are 462
representatives of the two board classes of distance measures, namely “lock-step” and 463
“elastic”. 464

465 **2.1.1 Euclidean Distance (ED)**

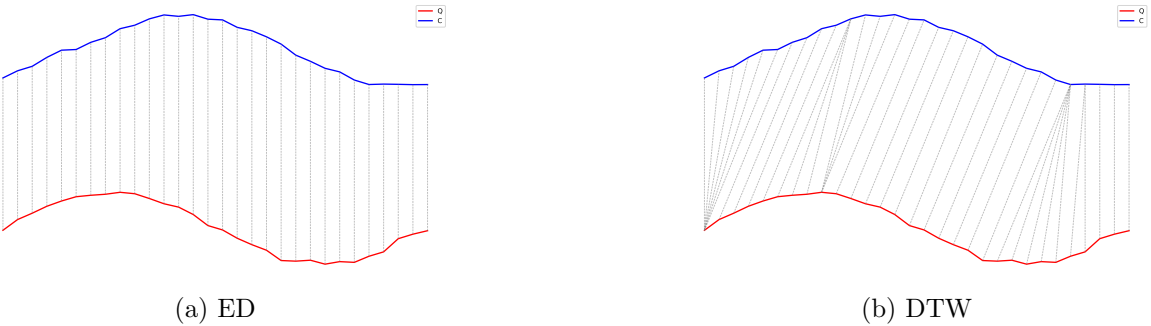


Figure 2.1: Alignments.

466 ED is a lock-step distance measure. Given two time series Q and C with the same
 467 length n , it compares the time point q_i of Q with the time point c_i of C at the same time
 468 (index). Note that, traditionally, lockstep distance measures require the two time series
 469 to have the same length because of the one-to-one alignment, as shown in Figure 2.1.
 470 However, in the setting of query by content, where it is always the case that $|Q| < |C|$,
 471 we can still apply a lock-step distance measure by either comparing Q with $C(1 : |Q|)$
 472 or padding Q using its last element to lengthen it to the same length of C . Minkowski
 473 distance is a generalization of Euclidean distance. Minkowski distance is the L_p -norm of
 474 the difference between the two time series X and Y , defined as:

$$D(X, Y) = \left(\sum_{i=1}^n |x_i - y_i|^p \right)^{\frac{1}{p}} \quad (2.1)$$

475 When $p = 2$, it corresponds to the Euclidean distance. When $p = 1$, it corresponds to
 476 the Manhattan distance. When $p = \infty$, it corresponds to the Chebyshev distance. In our
 477 studies, we focus on the Euclidean distance. Other lock-step distance measures include
 478 Pearson correlation distance. It accounts for the linear association between the two time
 479 series using the Pearson correlation coefficient. To note, there is another measure called
 480 Edit Distance for strings. And Edit Distance is also sometimes abbreviated as ED in
 481 string processing or bioinformatics. In this study, we focus on time series analysis and
 482 use ED to denote Euclidean distance rather than edit distance.

483 **2.1.2 Dynamic Time Warping (DTW)**

484 Dynamic Time Warping is an elastic measure [2]. In contrast to lock-step distance mea-
 485 sures, elastic distance measures allow one-to-many point matching, as shown in Figure 2.1.
 486 The one-to-many point matching allows the elastic distance measures to warp in the time
 487 axis (i.e., temporally) such that it can handle the local temporal distortions. While it

will be detailed in Chapter 4, it is briefly explained here. In short, it minimizes the cumulative distance between two time series, subject to constraints, by finding an optimal warping path W^* in a cost matrix, where W is the set of all possible paths and W^* is the optimal one. The constraints typically are (1) Boundary conditions, (2) Continuity, and (3) Monotonicity. Note that we can reduce pathological warping and accelerate computation by introducing a warping window. DTW with a warping window constraint is called constrained DTW (cDTW). Two famous windows are the Sakoe-Chiba band [2] and the Itakura parallelogram [3]. In the study, we focus on the Sakoe-Chiba band.

2.1.3 Derivative Dynamic Time Warping (DDTW)

The Derivative Dynamic Time Warping (DDTW) is a variant of DTW [4]. Instead of comparing original raw values, it compares two time series using their first-order derivatives, but with an approximation. In DTW, a point on a rising trend may be mapped to a point on a falling trend. It goes against our intuition. It can be solved by comparing their first-order derivatives, which encodes the slope information. The derivative T' of a time series T is computed approximately as follows.

$$t'_i = \frac{(t_i - t_{i-1}) + \frac{t_{i+1} - t_{i-1}}{2}}{2} \quad (2.2)$$

This estimate is simply the average of “the slope of the line through t_i and t_{i-1} (i.e., its left neighbor)” and “the slope of the line through t_{i-1} (i.e., its left neighbor) and t_{i+1} (i.e., its right neighbor)”. The $1/2$ term in the second item of the numerator comes from the fact that the separation in time of the t_{i-1} and t_{i+1} is 2. Note that the estimate is not defined for the first and last elements of the time series in the above equation. In these boundary cases, we use the estimates of the second and penultimate (i.e., the second-to-last thing) as the estimates for the first and last elements, respectively.

2.1.4 Weighted Dynamic Time Warping (WDTW)

The Weighted Dynamic Time Warping (WDTW) is a variant of DTW [5]. It is a penalty-based DTW designed to prevent pathological paths. Recall that a warping window (e.g., Sakoe-Chiba band) is enforced on the cost matrix of DTW, such that some paths are excluded. Only the paths that reside entirely in the warping window are feasible. This constraint may be too strict. WDTW uses a softer way for the same purpose. Instead of using a window to forbid the alignment of x_i and y_j that are far away in time. WDTW weights the cost of such alignment by multiplying it by a modified logistic weight function (MLWF) $\omega(k)$, defined as follows.

$$\omega(k) = \frac{\omega_{\max}}{1 + \exp(-g \cdot (k - m_c))} \quad (2.3)$$

519 Where:

- 520 • $k = |i - j|$. It is the phase difference (i.e., distance on the time axis from the
521 diagonal. The diagonal refers to the line where $i = j$.)
- 522 • ω_{\max} is the desired upper bound for the weight parameter, which is suggested to be
523 set to 1.
- 524 • m_c is the midpoint of a sequence. $m_c = m/2$.
- 525 • g is a constant that controls the level of penalization. It controls the curvature
526 (slope) of the function.

527 Intuitively, if x_i and y_j are far apart temporally, it will have a larger weight to discourage
528 their alignment and vice versa.

529 2.1.5 Weighted Derivative Dynamic Time Warping (WDDTW)

530 [5] also proposed the weighted version of DDTW. In brief, a weight is applied to the local
531 cost function when computing DTW on the first derivative.

532 2.1.6 Shape Dynamic Time Warping (shapeDTW)

533 The Shape Dynamic Time Warping (shapeDTW) is a variant of DTW [6]. The main mod-
534 ification to the original DTW is the way the local distance between points is computed.
535 Recall that DTW compares single scalar points. shapeDTW compares local descriptors.
536 The local descriptors are constructed using a sliding window on the original series, such
537 that for each point x , a L -subsequence with x as the center is extracted to compute the
538 higher-level feature of x . L is the user-given length of the subsequence to consider. By
539 default, it is set to 15. There are several ways to construct such a descriptor. For exam-
540 ple, a raw subsequence (i.e., a set of neighbor points surrounding the point of interest),
541 Piecewise aggregate approximation (PAA) [7, 8], slope, derivative, HOG-1D [9].

542 Then, the distance between descriptors is calculated rather than between raw values.
543 When a raw subsequence is chosen to construct the local descriptors, a common metric
544 used for comparing two local descriptors is the Euclidean distance. In the evaluation, a
545 raw subsequence is chosen to construct the local descriptors.

546 2.1.7 Amercing Dynamic Time Warping (ADTW)

547 The Amercing Dynamic Time Warping (WDTW) is a variant of DTW [10]. It is also
548 designed to constrain the amount of warping, as in cDTW and WDTW. While cDTW
549 imposes a hard window and WDTW uses multiplicative weights (i.e., MLWF), ADTW

introduces an additive penalty for non-diagonal alignment. The word “Amercing” means 550
 “fining”. The non-diagonal alignments are required to pay the fines. Unlike WDTW, 551
 which uses a multiplicative weight based on the position of the alignment, ADTW applies 552
 an additive penalty ω based on the action of warping. The non-diagonal alignments are 553
 penalized. Formally, the recursive relation for ADTW is defined as: 554

$$D(i, j) = d(q_i, c_j) + \min \begin{cases} D(i - 1, j - 1), \\ D(i - 1, j) + \omega, \\ D(i, j - 1) + \omega \end{cases} \quad (2.4)$$

ADTW penalizes the last two alignment actions. ω is a user-given hyperparameter. 555
 It should be a non-negative scalar constant. In practice, it is defined through cross- 556
 validation, which determines the optimal ω by training on a subset of data or heuristic 557
 search, which searches values in a user-given range. 558

To note, ADTW generalizes ED and DTW. If $\omega = 0$, no need to pay the fine for the 559
 non-diagonal alignment, which reduces to DTW. If $\omega \rightarrow \infty$, the non-diagonal alignment 560
 becomes prohibitive, and it reduces to ED. 561

2.2 Classification

In Chapter 3, we use ROCKET (RandOm Convolutional KErnel Transform) and its 563
 variants, including MiniRocket, MultiRocket, and Hydra, as the time series classifiers on 564
 the time series resulting from our encoding methods. Technically, they are not classifiers 565
 in their own right but rather feature extractors. These features are also called summary 566
 statistics. They are high-dimensional feature vectors that capture the characteristics of 567
 the original time series. The summary statistics are then fed to the classifiers to output 568
 the final classification results. 569

2.2.1 Ridge Classifier

The classifier that is usually chosen to work with ROCKET and its variants is a ridge 571
 classifier. The main advantage of it is speed. ROCKET and its variants generate a large 572
 number of features. 573

A ridge classifier is a wrapper that uses a ridge regression model as a routine to perform 574
 classification. It first maps the categorical labels of targets into continuous numbers, does 575
 the regression, and finally thresholds the numerical results from the regressor to obtain 576
 the classification result. 577

578 Given a training dataset $D = \{(x_i, y_i)\}_{i=1}^n$ with n instances, where $x_i \in \mathbb{R}^P$ is the
 579 feature vector with P dimensions and $y_i \in \{+1, -1\}$ is its label, it minimize the following
 580 optimization function.

$$\min_w \left(\sum_{i=1}^n (x_i^T w - y_i)^2 + \lambda \|w\|_2^2 \right) \quad (2.5)$$

581 Where $\|w\|_2^2 = \sum_{j=1}^p w_j^2$ is the L_2 norm of the weight vector and $\lambda > 0$ control the
 582 penalty. We explain the equation in brief. There are two terms inside the bracket. The
 583 first term is simply the sum of the residual, same as the one in the least squares method.
 584 The second term is called the L_2 penalty and is used to introduce bias in the fit to avoid
 585 overfitting. Hence, λ serves as a regularization hyperparameter between the trade-off
 586 between bias and variance.

587 Since the above optimization function in a ridge classifier has a closed-form solution,
 588 it can be solved using linear algebra rather than iterative optimization, as in logistic
 589 regression. Besides, the generated features by the random kernels in ROCKET and its
 590 variants are highly correlated. Ridge regularization, also known as the L_2 norm, can
 591 handle this case. Ridge regression shrinks regression coefficients toward zero by adding
 592 an L2 penalty. It reduces model complexity and helps with multicollinearity.

Chapter 3

593

MTSCCleav: a Multivariate Time Series Classification (MTSC)-based Method for Predicting Human Dicer Cleavage Sites

594

595

596

597

MicroRNAs (miRNAs) are small non-coding RNAs (ncRNAs) that regulate gene expression at the post-transcriptional level, thereby playing essential roles in diverse biological processes. The biogenesis of miRNAs requires dicer to cleave at specific sites on the precursor miRNAs (pre-miRNAs). Several machine learning approaches have been proposed to predict whether an input sequence contains a cleavage site. However, they rely heavily on complex feature engineering or opaque deep neural networks. It results in a lack of generalizability and a long running time. There is a need for an alternative modeling paradigm that is accurate, fast, and simple.

We proposed a novel approach to frame the task as a multivariate time series classification problem. Nine encoding methods have been proposed to convert the sequence and the predicted secondary structure into a time series. We also leveraged the probabilities of the base pairs in the predicted secondary structure. Computational experiments demonstrate that our proposed method can achieve better or comparable results in terms of using a simpler, more intuitive model and less computational time. It achieves 3.7X to 28.8X speedup. Through perturbation experiments, we found that regions close to the center of pre-miRNAs are essential for predicting human dicer cleavage sites.

By transforming the RNA sequence and its secondary structure information into a time series and utilizing simple, state-of-the-art time series classifiers, we achieved comparable or even superior performance in a simpler and faster manner.

Code is available at: <https://github.com/colemanyu/time-series-classification-cleavage>.

619 3.1 Background

620 One of the most important theories in molecular biology is the central dogma. It depicts
621 the flow of genetic information [11, 12]. Proteins are the functional units. The information
622 stored in DNA is used to create them. Genes (segments) in DNA are used as templates for
623 messenger RNAs (mRNAs) synthesis. An mRNA acts as a set of instructions to assemble
624 a chain of amino acids, which form a linear polypeptide. To become biologically active,
625 this chain is folded into a specific 3D structure, a proper configuration that enables it to
626 perform its desired functions. This folded polypeptide is called a functional protein, or
627 simply a protein. This entire process closely resembles how a computer program runs on
628 a machine. The source code does not function by itself. First, it is translated into an
629 assembly code (a lower-level, less human-readable form) and then into an executable file
630 that can actually perform the intended tasks [13].

631 These mRNAs are called “coding RNAs” because they code for proteins. There are
632 other genes in which the final product is the RNA molecule itself. They are called
633 non-coding RNAs (ncRNAs). Two types of small ncRNAs are particularly important.
634 They are microRNAs (miRNAs) and small interfering RNAs (siRNAs). Their discovery
635 was recognized with the 2006 Nobel Prize in Physiology or Medicine¹, awarded for work
636 completed only eight years prior [11].

637 In this study, we focus on miRNAs. An miRNA can regulate the expression of several
638 proteins. Hence, understanding the biogenesis of miRNAs is of great value. It involves
639 the processing of primary miRNAs (pri-miRNAs). RNAs are 3D molecules. However, it
640 is hard to measure the 3D structure (tertiary structure) from the experiment and predict
641 it from 1D sequence. We can understand their properties by analyzing their 1D sequence
642 or 2D structure, known as secondary structure. RNA sequence is easily obtained through
643 sequencing. The sequence and its predicted secondary structure of a pri-miRNA “hsa-
644 let-7a-1” is shown in Figure 3.1.

645 Recall that a pri-miRNA contains a hairpin loop, also called a stem loop. A mi-
646 croprocessor complex comprising Drosa and DCGR8 cleaves the pri-miRNA to form a
647 precursor miRNA (pre-miRNA) inside the nucleus. The stem-loop is still preserved, but
648 the two arms become shorter. After that, the pri-miRNA is transported by Exportin 5
649 from the nucleus to the cytoplasm. It is further cleaved by an enzyme called dicer [14].
650 Dicer cleaves the stem-loop from the two arms at the two cleavage sites, shown as the two
651 scissors in Figure 3.1. The stem-loop is removed. It results in a short double-stranded
652 miRNA molecule, known as an miRNA duplex, which consists of the 5p strand and the

¹The Nobel Prize in Physiology or Medicine 2006 - NobelPrize.org:
<https://www.nobelprize.org/prizes/medicine/2006/summary/> (Accessed on: 2025-06-13).

²Its miRBase entry: <https://mirbase.org/hairpin/MI0000060>. (Accessed on: 2025-06-12).

³RNAfold web server: <http://rna.tbi.univie.ac.at/cgi-bin/RNAWebSuite/RNAfold.cgi>. (Accessed on: 2025-06-12). The figure is viewed in “forna”. This view option can be chosen on the website.

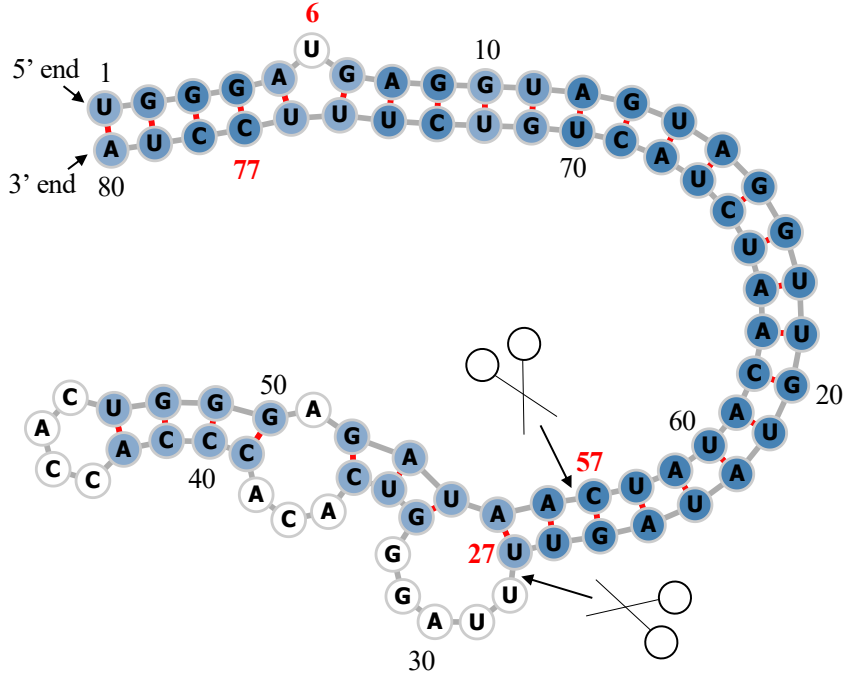


Figure 3.1: Predicted secondary structure of the sequence S of pri-miRNA “hsa-let-7a-1”². Experimental evidence suggests that the two deviated mature miRNAs are $UGA \cdots GUU$ and $CUA \cdots UUC$. They are $S(6 : 27)$ and $S(57 : 77)$ (Both ends are inclusive.). The ends are highlighted in **bold**. Since $S(6 : 27)$ ($S(57 : 77)$) is near the 5' (3') end, we call it “5p (3p) mature miRNA”. The two scissors indicate the two cleavage sites. The color intensity of the nodes reflects their base-pair probability in this predicted secondary structure. The deeper the color, the higher the probability. The unpaired nodes are uncolored. The raw figure is generated by RNAfold web server³.

3p strand⁴. These molecules may be subjected to additional trimming. The miRNA duplex is loaded into an RNA-induced silencing complex (RISC). RISC unwinds the duplex and tends to retain the strand with the less stable 5' end as the guide strand. The other strand is called the passenger strand. The retained strand guides the RISC to silence the target mRNA. Note that both strands can become the guide strand.

Dicer plays an important role in the biogenesis of miRNAs. It is reasonable to argue that the structure of the pre-miRNAs informs dicer about the cleavage process. It would be of great benefit to understand how dicer selects cleavage sites from the neighborhood information near the cleavage sites. Studies [15, 16, 17] revealed that the secondary structures are essential for cleavage site determination. Hence, to predict or classify whether a subsequence, extracted from the sequence of a pri-miRNA, contains a cleavage site, we can make use of both the sequence and secondary structure information. PHDcleav employed support vector machines (SVM), leveraging sequence and structure-based features for the classification [18]. LBSizeCleav improved upon it by considering the loop

⁴The 5p strand comes from the 5' arm while the 3p strand comes from the 3' arm. For the directionality, the 5p (3p) strand retains the original 5' (3') end of the pre-miRNA.

and bulge lengths [19]. [20] proposed an ensemble learning approach, using a gradient boosting machine for better accuracy. [21] developed a deep learning model, namely DiCleave. This model used an autoencoder to learn the secondary structure embeddings of pre-miRNAs from all the species in the miRBase database and leveraged this information. All these methods begin with curated pre-miRNA sequences from the miRBase database. Their secondary structures are predicted. Patterns are extracted from the sequence and the secondary structure. They create the positive cleavage patterns by setting the cleavage sites at the middle of the patterns. The follow-up work of [21], which created the cleavage pattern by allowing cleavage sites to appear at any position within the pattern, instead of the middle only [22]. It created a much larger dataset. This increased dataset facilitates the learning of the deep learning method at the cost of increased running time. We utilized the original dataset setting [18, 19, 20, 21]. DiCleave is the current state-of-the-art (SOTA) for this problem with the original dataset setting.

These models suffer several limitations. They rely heavily on complicated feature engineering or opaque deep learning models [20, 21, 22]. It results in a lack of generalizability and a long running time. There is a need to design a simpler model so that it can be easily extended to other prediction tasks on RNA data. One way to analyze sequence data is to transform it into time series data. In response to this, we proposed a multivariate time series classification-based method. Our contributions are shown as follows.

1. To the best of our knowledge, we are the first to frame the prediction of the cleavage sites as a multivariate time series classification problem.
2. We introduced several encoding methods to convert RNA data to time series.
3. We proposed utilizing the base-pair probabilities in the predicted secondary structure for the prediction. To our surprise, this information has been ignored in the existing studies.
4. For computational efficiency, our method achieves a 3.7X to 28.8X speedup compared to the state-of-the-art (SOTA).
5. We conducted perturbation-based experiments. It shows that regions close to the cleavage sites are important for this problem. It is consistent with the existing study [20].

3.2 Methods

The overall pipeline of this study is summarized in Figure 3.2.

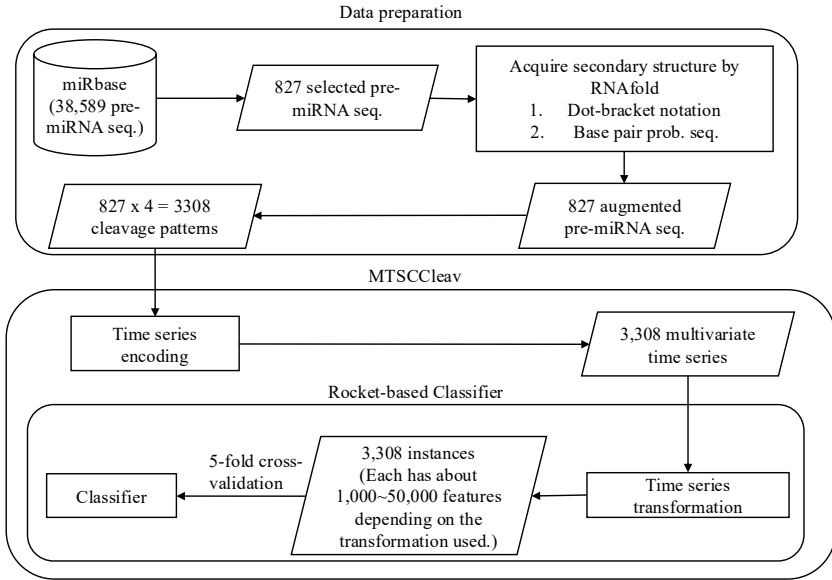


Figure 3.2: The overall pipeline of this study. Symbol notations: Cylinder - Dataset, Rectangle - Process, Parallelogram - Input / Output, Rounded Rectangle - Component.

3.2.1 Data Preparation

700

Accession	Name	Organism	Sequence	Mature miRNA 1	Mature miRNA 2
MI0000001	cel-let-7	<i>Caenorhabditis elegans</i>	<i>UACAC</i> ... <i>UUCGA</i>	cel-let-7-5p 17:38 experimental	cel-let-7-3p 60:81 experimental
MI0000060	hsa-let-7a-1	<i>Homo sapiens</i>	<i>UGGGA</i> ... <i>UCCUA</i>	hsa-let-7a-5p 6:27 experimental	hsa-let-7a-3p 57:77 experimental
MI0000114	hsa-mir-107	<i>Homo sapiens</i>	<i>CUCUC</i> ... <i>ACAGA</i>	hsa-miR-107 50:72 experimental	NA
MI0000238	hsa-mir-196a-1	<i>Homo sapiens</i>	<i>GUGAA</i> ... <i>UUCAC</i>	hsa-miR-196a-5p 7:28 experimental	hsa-miR-196a-1-3p 45:65 not experimental

Table 3.1: Selected representative records from miRBase. For the last two columns, the first line shows the name, the second line shows its location in the original sequence, and the third line indicates whether its existence has experimental evidence. The selected one is highlighted in **bold**.

We used miRBase database [23]⁵. The database comprises miRNA data from various organisms [24]. The database contains 38,589 miRNA records. Each record refers to an miRNA sequence, along with other properties such as name, accession, organism, and information on its derivative miRNA products. We are interested in pri-miRNA in humans. The derivative miRNA products are the mature miRNAs. The database also annotates the location of the mature miRNA within the original sequence and indicates whether its existence has experimental evidence.

701
702
703
704
705
706
707

⁵The website is www.mirbase.org, and the newest version of the database is Release 22.1 (Accessed on 2025-06-22).

708 Table 3.1 shows its four representative records. We first selected the records from
 709 humans (*Homo sapiens*). It resulted in 1,917 records. To identify the actual locations of
 710 the two cleavage sites in the pri-miRNA sequence supported by experimental evidence, we
 711 selected records that have two mature miRNAs resulting from cleavage at the 5p arm and
 712 the 3p arm, both of which have experimental support. Hence, only “MI0000060” (“hsa-
 713 let-7a-1”) would be selected in the table. It would serve as our running example. Its whole
 714 sequence is listed in Table 3.2. After the selection process, we selected 827 experimental
 715 validated pre-miRNA sequences, each with its two mature miRNA products. This formed
 716 our dataset.

Sequence	Secondary Structure (In Dot-bracket notation)
1 UGGGA UGAGGUAGUAGGUUGUAUAGUU 27 28 UUAGGGUCACACCCACCACUGGGAGAU 54 55 AA CUAUACAAUCUACUGUCUUUC CUA 80	1 (((((.(((((((((((((27 28 UUAGGGUCACACCCACCACUGGGAGAU 54 55))))))))))))))))))))) 80
Base-pair probabilities sequence (the first 10 bases)	
1 (0.549, 0.946, 0.987, 0.987, 0.904) 5 6 (0.000 , 0.841, 0.974, 0.981, 0.890) 10	

Table 3.2: The whole sequence of “hsa-let-7a-1” and its predicted secondary structure by RNAfold. The corresponding positions of the two mature miRNAs and the probability of the unpaired “U” are highlighted in **bold**.

717 Augment the Dataset with Secondary Structure Information

718 We leveraged the predicted secondary structure of these sequences to enhance the ac-
 719 curacy of the classification. Recall that a specific three-dimensional (3D) structure is
 720 required for DNA, RNA, and protein to perform functions [25]. However, finding these
 721 3D structures using experimental methods such as X-ray crystallography or nuclear mag-
 722 netic resonance (NMR) is costly and time-consuming. Hence, prediction methods for such
 723 3D structures are necessary and helpful for downstream analysis. However, predicting the
 724 3D structures is challenging. One of the reasons is that there are some “nonconventional”
 725 base-pair interactions (e.g., noncanonical and rare A-G) that allow an RNA sequence to
 726 fold into a 3D structure, in addition to the (G, U) wobble pair, which is common and
 727 functionally important in RNA secondary structures. It makes the search space for pre-
 728 diction much larger than, in the 2D case, the secondary structure. The local structures
 729 of the 3D structures, the secondary structures, only focus on the conventional base-pair
 730 interactions [12]. Hence, predicting secondary structures is easier and faster. We em-
 731 ployed RNAfold from the ViennaRNA Package⁶ to predict the secondary structure for
 732 a given pri-miRNA S [26]. RNAfold returns the secondary structure in the dot-bracket
 733 notation and a matrix of base-pair probabilities. The matrix is a square matrix with the
 734 side length $|S|$, where each entry m_{ij} is the probability of base s_i paired up with base s_j .

⁶The latest stable release is Version 2.7.0 (Accessed on 2025-06-22).

Dot-bracket notation is a way of representing the secondary structure of S . Open parentheses “(” (Close parentheses “)”) indicates that the base is paired with a complementary base further (earlier) along in S . Dot “.” indicates that the base is unpaired. Equipped with the matrix, we can construct the base-pair probability sequence of S . The predicted secondary structure and the base-pair probability sequence of our running example are shown in Table 3.2. 735
736
737
738
739
740

Extract Cleavage Patterns 741

The locations of the two mature miRNAs on the whole sequence indicate the probable locations of the two cleavage sites. The 5p cleavage site must be beyond and near the ending location of the 5p mature miRNA. We deemed the immediate bond next to the 5p mature miRNA’s ending position the 5p cleavage site, with the knowledge that the actual cleavage site may not be this immediate bond but rather the nearby bonds after it. The same applies to the 3p cleavage site. It is located at the immediate bond before the starting position of the 3p mature miRNA. 742
743
744
745
746
747
748

For each arm of each whole sequence, we extracted a 14-string⁷ with the cleavage site located at the center of the string. The first 7 nt (nucleotide) before the center are highlighted in **bold**. In our running example, it would be “**UUAUAGUU**UUAGGU” for the 5p cleavage site and “**GAGAUAA**CUAUACA” for the 3p cleavage site. We refer to these 14-strings as cleavage patterns. We also generate non-cleavage patterns by selecting a 14-string with the center 6 nt away from the corresponding cleavage sites towards the corresponding mature miRNA [19, 20] for each arm of each whole sequence. So, in our running example, the 5p non-cleavage pattern would be “**AGGUUGU**AUAGUUU”. The 3p non-cleavage pattern would be “**ACUAUAC**AAUCUAC”. 749
750
751
752
753
754
755
756
757

In conclusion, for a given pri-miRNA sequence, we can generate two cleavage patterns and two non-cleavage patterns. We call these four patterns simply the “four strings” of a given pri-miRNA. We also call each string a strand. The “four strings” of our running example are listed in Table 3.3. 758
759
760
761

	5p cleav	5p non-cleav	3p cleav	3p non-cleav
Input strand	UUAUAGUU UUAGGU	AGGUUGU AUAGUUU	GAGAUAA CUAUACA	ACUAUAC AAUCUAC
Complementary strand	AUAUCAA_____UA	UCUAACAUAAUCAA_	C_CUGUUGAU AUGU	UGAUAUGUUGGAUG

Table 3.3: The first row shows the “four strings” of “hsa-let-7a-1”. Their complementary strands are shown in the second row. As a whole, they are referred to as the “eight strings”.

We can construct the complementary strand of each of the strands in the “four strings” by finding the corresponding paired base for each of the bases in the input strand by considering the secondary structure information. We use “_” to denote the unpaired base 762
763
764

⁷String with length = 14.

in the complementary strand. For example, in Figure 3.1, “UUAGG” in the 5p cleavage pattern is unpaired, while other bases pair with some bases, the resulting complementary strand is “AUAUCAA____UA”. There is a loop/budge there. We refer to the “four strings” and the four complementary strands together as the “eight strings” of the input pre-miRNA. It is also shown in Table 3.3.

3.2.2 Time Series Encoding

A *time series* $T = t_1, t_2, \dots, t_n$ is a sequence of real-valued numbers⁸. A short contiguous region of T is called a subsequence. A *subsequence* $T(i : j) = t_i, t_{i+1}, \dots, t_j$ of a time series T is a shorter time series that starts from position i and ends at position j , where $i < j$.

Strings and time series are temporal sequences. The difference between strings and time series lies in their behavioral attributes [27]. For strings, an entry is a letter from a predefined set called the *alphabet*. For example, the alphabet is $\{A, C, G, T\}$ in the DNA string, while $\{A, C, G, U\}$ in the RNA string. For time series, an entry is a real number. Unlike real numbers, there is no ordering in the alphabet unless some external domain knowledge is introduced.

The study of applying signal processing techniques to genomic data is called “Genomic Signal Processing” (GSP) [28, 29]. In the field of GSP, the time series representations of DNA strings are referred to as DNA numeric representations (DNR). Many DNRs have been proposed. We noted that DNA strings and RNA strings are equivalent from a computational standpoint. Many transformation methods designed for DNA can be applied to RNA by simply substituting T with U . We present nine encoding methods. The relationship among them is shown in Figure 3.3.

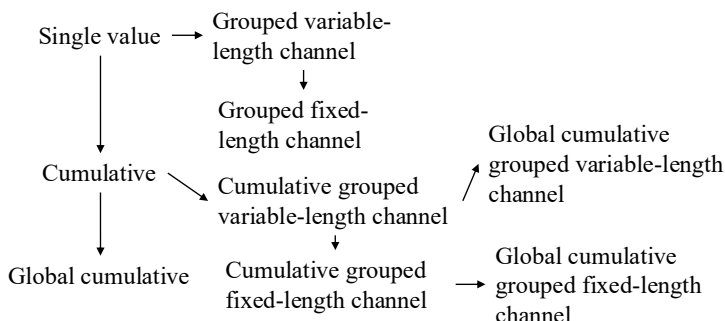


Figure 3.3: Relationship of the proposed encoding methods.

Single Value versus Cumulative

One of the simple, if not the simplest, encoding is to map the letters into numbers. Domain knowledge can be utilized. This approach is called the “Single value map-

⁸Unless otherwise specified, we denote entries of a time series (e.g., T) using the corresponding lowercase letter (e.g., t).

ping” [30, 31, 32, 33, 28]. One single value is assigned to each of the letters. [34] employed the atomic number of each nucleotide as the transformed values, where $\{G = 78, A = 70, C = 58, T = 66\}$. [35] used electron-ion interaction potential representation (EIIP) as such value, where $\{G = 0.0806, A = 0.1260, C = 0.1340, T = 0.1335\}$. Our goal is to transform the input strand and its complementary strand into time series, aiming to capture the information contained in these sequences and the secondary structure implied by them. We employed the following reasoning to assign the value:

1. We employ the complementary property [36, 32] during encoding. Recall that in the base-pairing rules, G pairs with C to form three hydrogen bonds while A pairs with U^9 to form two hydrogen bonds. $G-C$ pairs are more stable than $A-U$ pairs. G (U) can be regarded as the “inverse” of C (A). We can preserve these base-pairing rules in the encoding by assigning G (A) and C (U) opposite values.
2. G and A have a two-ring structure. They are purines. C and U have a single-ring structure. They are pyrimidines. Hence, we put G and A (C and U) on the same side of the number line with zero in the middle.
3. The lower stability of $A-U$ pairs promotes strand separation, thereby facilitating the unwinding of the miRNA duplex during RISC loading. Regions rich in A and U are thus more likely to undergo strand selection and cleavage events. We assigned A (U) with a larger absolute value than G (C) to reflect this functional relevance. It aims to highlight sequence regions with higher cleavage potential.

It results in our baseline transformation method, namely “Single value mapping” as shown in row 1 of Table 3.4. S is the input strand. When we encode S without incorporating the corresponding base-pair probability sequence P , we set $p_i = 1$ for all the entries of P . We use the first ten nucleotides of the complementary strand of the 3p cleav of “hsa-let-7a-1”, as shown in Table 3.3 as S in the examples in Table 3.4.

With the assigned value to each nucleotide defined in single-value mapping, we can compute a cumulative sum of those values over time. It captures the aggregated signal by accumulating past events, allowing us to focus on the trend [37, 38]. We named this method as “Cumulative mapping”, shown in row 4 of Table 3.4.

Grouped Variable-Length Channel versus Grouped Local-Length Channel

We can transform the input strand into a multivariate time series with two channels using grouped binary encoding, where nucleotides are grouped into (A, U) and (G, C) . It releases our third assumption that A (U) has a larger absolute value than G (C). We proposed two variations. The first one allows the output to be variable-length sequences

⁹In DNA, A pairs with T .

	Encoding	Algorithm	Example
1	Single value mapping [30, 31, 32, 33, 28]	$\text{for } i = 1 \text{ to } S :$ $t_i = \begin{cases} 2 \cdot p_i & \text{if } s_i = A \\ 1 \cdot p_i & \text{if } s_i = G \\ -1 \cdot p_i & \text{if } s_i = C \\ -2 \cdot p_i & \text{if } s_i = U \\ 0 & \text{otherwise} \end{cases}$ return T	$S = C, -, C, U, G, U, U, G, A, U$ $P = 0.843, 0.000, 0.807, 0.807, 0.793,$ $0.914, 0.982, 1.000, 0.999, 0.999$ Without base-pair probability sequence: $T = -1, 0, -1, -2, 1, -2, -2, 1, 2, -2$ With base-pair probability sequence: $T = -0.843, 0.000, -0.807, -1.614,$ $0.793, -1.829, -1.963,$ $1.000, 1.999, -1.998$
2	Grouped variable-length channel mapping	$j = 1, k = 1$ $\text{for } i = 1 \text{ to } S :$ $t_j^1 = \begin{cases} 1 \cdot p_i & \text{if } s_i = A \\ -1 \cdot p_i & \text{if } s_i = U \\ 0 & \text{otherwise} \end{cases}$ $t_k^2 = \begin{cases} 1 \cdot p_i & \text{if } s_i = G \\ -1 \cdot p_i & \text{if } s_i = C \\ \text{if } (s_i = G) \text{ or } (s_i = C): \\ \quad \text{increment } k \text{ by 1} \\ \text{else:} \\ \quad \text{increment } j \text{ by 1} \end{cases}$ return T^1, T^2	Without base-pair probability sequence: $T^1 = 0, -1, -1, -1, 1, -1$ $T^2 = -1, -1, 1, 1$ With base-pair probability sequence: $T^1 = 0.000, -0.807, -0.914, -0.982, 0.999, -0.999$ $T^2 = -0.843, -0.807, 0.793, 1.000$
3	Grouped fixed-length channel mapping	$\text{for } i = 1 \text{ to } S :$ $t_i^1 = \begin{cases} 1 \cdot p_i & \text{if } s_i = A \\ -1 \cdot p_i & \text{if } s_i = U \\ 0 & \text{otherwise} \end{cases}$ $t_i^2 = \begin{cases} 1 \cdot p_i & \text{if } s_i = G \\ -1 \cdot p_i & \text{if } s_i = C \\ 0 & \text{otherwise} \end{cases}$ return T^1, T^2	Without base-pair probability sequence: $T^1 = 0, 0, -1, 0, -1, -1, 0, 1, -1$ $T^2 = -1, 0, -1, 0, 1, 0, 0, 1, 0, 0$ With base-pair probability sequence: $T^1 = 0.000, 0.000, 0.000, -0.807,$ $0.000, -0.914, -0.982,$ $0.000, 0.999, -0.9999$ $T^2 = -0.843, 0.000, -0.807, 0.000,$ $0.793, 0.000, 0.000,$ $1.000, 0.000, 0.000$
4	Cumulative mapping [37, 38]	$t_1 = 0$ $\text{for } i = 1 \text{ to } S :$ $t_{i+1} = \begin{cases} t_i + 2 \cdot p_i & \text{if } s_i = A \\ t_i + 1 \cdot p_i & \text{if } s_i = G \\ t_i - 1 \cdot p_i & \text{if } s_i = C \\ t_i - 2 \cdot p_i & \text{if } s_i = U \\ t_i & \text{otherwise} \end{cases}$ return $T // T = S + 1$	Without base-pair probability sequence: $T = 0, -1, -1, -2, -4, -3, -5, -7, -6, -4, -6$ With base-pair probability sequence: $T = 0.000, -0.843, -0.843, -1.650,$ $-3.265, -2.471, -4.300, -6.263,$ $-5.264, -3.265, -5.263$
5	Cumulative grouped variable-length channel mapping	$t_1^1 = 0, t_1^2 = 0$ $j = 1, k = 1$ $\text{for } i = 1 \text{ to } S :$ $t_{j+1}^1 = \begin{cases} t_j^1 + 1 \cdot p_i & \text{if } s_i = A \\ t_j^1 - 1 \cdot p_i & \text{if } s_i = U \\ t_j^1 & \text{if } s_i = - \end{cases}$ $t_{k+1}^2 = \begin{cases} t_k^2 + 1 \cdot p_i & \text{if } s_i = G \\ t_k^2 - 1 \cdot p_i & \text{if } s_i = C \\ t_k^2 & \text{otherwise} \end{cases}$ $\text{if } (s_i = G) \text{ or } (s_i = C):$ $\quad \text{increment } k \text{ by 1}$ else: $\quad \text{increment } j \text{ by 1}$ return T^1, T^2	Without base-pair probability sequence: $T^1 = 0, -1, -2, -3, -2, -3$ $T^2 = 0, -1, -2, -1, 0$ With base-pair probability sequence: $T^1 = 0.000, -0.807, -1.722,$ $-2.703, -1.704, -2.703$ $T^2 = 0.000, -0.843, -1.650,$ $-0.857, 0.143$
6	Cumulative grouped fixed-length channel mapping	$t_1^1 = 0, t_1^2 = 0$ $\text{for } i = 1 \text{ to } S :$ $t_{i+1}^1 = \begin{cases} t_i^1 + 1 \cdot p_i & \text{if } s_i = A \\ t_i^1 - 1 \cdot p_i & \text{if } s_i = U \\ t_i^1 & \text{otherwise} \end{cases}$ $t_{i+1}^2 = \begin{cases} t_i^2 + 1 \cdot p_i & \text{if } s_i = G \\ t_i^2 - 1 \cdot p_i & \text{if } s_i = C \\ t_i^2 & \text{otherwise} \end{cases}$ return $T^1, T^2 // T^1 = T^2 = S + 1$	Without base-pair probability sequence: $T^1 = 0, 0, 0, -1, -1, -2, -3, -2, -3$ $T^2 = 0, -1, -1, -2, -2, -1, -1, 0, 0, 0$ With base-pair probability sequence: $T^1 = 0.000, 0.000, 0.000, 0.000,$ $-0.807, -0.807, -1.722, -2.703,$ $-2.703, -1.704, -2.703$ $T^2 = 0.000, -0.843, -0.843, -1.650,$ $-1.650, -0.857, -0.857, -0.857,$ $0.143, 0.143, 0.143$

Table 3.4: Time series encoding. P is the corresponding base-pair probability sequence of S . $p_i = 1$ if we encode S without incorporating base-pair probability sequence.

per channel, depending on group-specific occurrences. The second one always returns two resulting sequences of a fixed length. Two variations extended from single value mapping are shown in rows 2 and 3, while those extended from cumulative mapping are shown in rows 5 and 6 in Table 3.4. 824
825
826
827

Global Cumulative versus Local Cumulative 828

In cumulative mapping and its variations, we can choose where to start the accumulation. 829
For a given subsequence S' of the whole sequence S , accumulation can start from the 830
beginning of S even if only S' is used downstream. It can also begin just at the start 831
of the S' . The first one preserves the global context. It can be useful when previous 832
nucleotides (those before S') influence later interpretation. The second one focuses solely 833
on local history in S' , ignoring global history. It is helpful if the previous nucleotides do 834
not affect the chemical property of S' . 835

Consider $T = 0, -1, \dots, -6$ of the input string S in “Cumulative mapping” in Table 3.4, 836
which accumulates from 0. S is the suffix with length = 10 of the constructed complemen- 837
tary strand of $S(1 : 63)$ in Figure 3.1. If we start the accumulation from the first entry 838
of the constructed complementary strand instead, it will yield a different result. Suppose 839
that the last entry of the time series encoded in the cumulative mapping of the con- 840
structed complementary strand is -8, the time series encoded in the “Global cumulative 841
mapping” for S would accumulate from -8 instead of 0. The result is $T = -8, -9, \dots, -14$. 842
Note that it has the same trend as the original T . This “Global cumulative” concept can 843
be applied to every cumulative-based method, as shown in Figure 3.3. 844

Incorporating Base-Pair Probabilities 845

We can incorporate the base-pair probabilities P in the encoding by thinking of it as the 846
weight or confidence p_i in the value assignment of each nucleotide s_i . It is implemented 847
by multiplying the base-pair probability p_i of the nucleotide s_i with the assigned value of 848
the kind of nucleotide of s_i during encoding, as shown in Table 3.4. 849

Transforming the Secondary Structure into a Time Series 850

We can transform the secondary structure in the dot-bracket notation into a time series 851
by “Single value mapping”, where “(” maps to 1, “.” maps to 0, and “)” maps to -1. 852

3.2.3 Time Series Classification 853

In univariate time series classification, an instance in the dataset consists of a time series 854
 $x = x_1, x_2, \dots, x_m$ with m observations and a discrete class label y , which takes c possible 855

values [39, 40]. If $c = 2$, we refer to binary classification. If $c > 2$, we refer to multi-class classification. In multivariate time series classification, the time series is not a single sequence but a list of sequences. Each sequence is called a channel. There are many classifiers defined for time series data, including distance-based, feature-based, interval-based, shapelet-based, dictionary-based, convolution-based, and deep learning-based classifiers. Additionally, two or more of the above approaches can be combined, resulting in hybrid approaches [1, 40, 39]. We employed convolution-based classifiers due to their simplicity and accuracy.

Convolution-Based Classifiers

Convolution-based classifiers first use randomly parameterized kernels to perform convolutions on the original time series T . A kernel is referred to as parameterized because its behavior is governed by a set of parameters, which will be discussed in detail later. Convolution is an operation to transform T to another time series M , where M is called the activation map. Its entry M_i is calculated by applying a kernel ω with length l to T at position i , defined as follows:

$$M_i = T(i : i + l - 1) * \omega = \sum_{j=0}^{l-1} t_{i+j} \cdot \omega_{1+j}$$

To note, $|T(i : i + l - 1)| = |\omega| = l$. Entries M_i 's are calculated by sliding ω across T and computing a dot product. Additionally, although the original paper [41] used the term “convolution” to refer to the above operation, “cross-correlation” may be a more suitable term for this operation. Recall T with length m has $(m - l + 1)$ sliding windows of length l , given that the increment is 1^{10} , which defines the length of M .

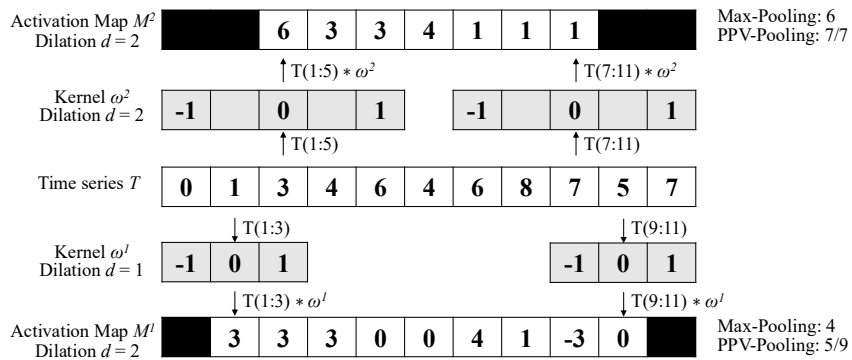


Figure 3.4: Features generation in the transformation

Figure 3.4 shows two kernels ω^1 and ω^2 with lengths 3 and 5, respectively. Each of which performs a convolution with T and returns two activation maps, M^1 and M^2 ,

¹⁰One step to the right per time.

respectively. For example, $M_1^1 = T(1 : 3) * \omega^1 = 3$. By sliding ω^1 one time stamp at a time, an activation map M^1 with length = $(m - l + 1) = 11 - 3 + 1 = 9$ is obtained. Then, pooling operations, such as the maximum (MAX) and proportion of positive values (PPV), are applied on M^1 to derive the summary features. In Figure 3.4, MAX and PPV are applied on M^1 and M^2 . The summary features of M^1 are 4 and $5/9$, which correspond to MAX and PPV, respectively. Dilation refers to a method that enables a kernel to cover a larger portion by creating empty spaces between entries in the kernel. The dilation d of ω^2 is 2. It introduces a gap of 1 in every two values of ω^2 .

The most popular convolution-based approach is the Random Convolutional Kernel Transform (ROCKET) [41]. It generates a large number of randomly parameterized kernels, ranging from thousands to tens of thousands. The kernel's parameters include length, weights (the entries inside the kernel), bias (the value added to the result of the convolution operation), and dilation. Additionally, padding can be applied to T at the start and end, ensuring M has the same length as the input. To note, T , M_1 , and M_2 in Figure 3.4 have different lengths. The summary statistics of the activation map are obtained through two pooling operations: MAX and PPV. Hence, for k kernels, the transformed data has $2k$ features. The default value of k is 10,000.

There are two extensions of ROCKET. They are MiniROCKET [42] and MultiROCKET [43]. MiniROCKET removes unnecessary operations and many of the random components in the definition of kernels used by ROCKET. It speeds up Rocket by over an order of magnitude with no significant difference in accuracy, making the classifier almost deterministic. For example, the kernel length is fixed, and only two weight values are used. Only PPV is used for the summary statistics. MultiROCKET is extended from MiniROCKET. The main improvement of it is to extract features from first-order differences as defined in Table 3.5 and add three new pooling operations [43]. The three added operations are mean of positive values (MPV), mean of indices of positive values (MIPV) and longest stretch of positive values (LSPV).

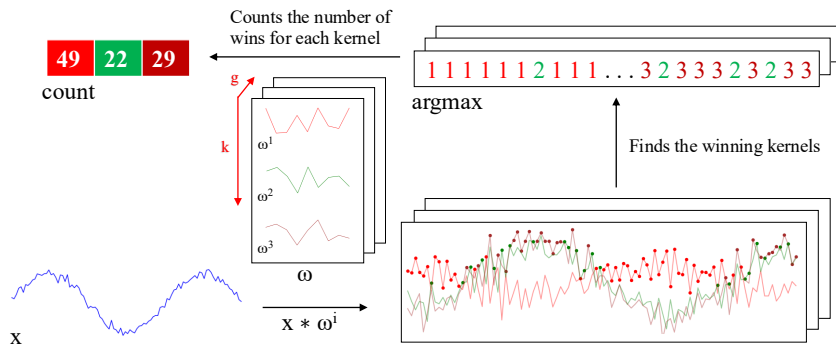


Figure 3.5: Convolutions of HYDRA for each input time series with a set of random kernels w , organized into g groups with k kernels each.

905 The HYbrid Dictionary-ROCKET Architecture (Hydra) combines dictionary-based
906 and convolution-based models [44]. Similar to ROCKET-based classifiers, it uses random
907 kernels to extract features from the input time series. But it groups the kernels into g
908 groups of k kernels each, as shown in Figure 3.5. Each time series is passed through
909 all the groups. For each group of kernels, we slide them across T and compute the dot
910 product at each timestamp. Recall that the dot product of two input vectors (x and
911 w_i) has the maximum value when the two vectors align in the same direction and the
912 minimum value when they are oriented in opposite directions. We record the kernel
913 that best matches the subsequence of T at each timestamp in each group (i.e., argmax).
914 We refer to these kernels as the winning kernels. This results in a k -dimensional count
915 vector for each of the g groups, where $k = 3$ in Figure 3.5. This results in a total of
916 $g \times k$ features, with default values of $g = 64$ and $k = 8$. It uses a total of $k \times g = 512$
917 kernels per dilation. In addition to recording the kernel with the maximum response,
918 we can also record the kernel with the minimum response, knowing that this kernel will
919 be the best match with the “inverted” subsequence of T . Hydra is applied to both the
920 original time series and its first-order differences. Hydra generated approximately 1000
921 features for each instance in our dataset. [44] found that it can improve the accuracy
922 by concatenating features generated from Hydra with those from MultiRocket. This
923 classifier is called MultiROCKET-Hydra.

924 These five classifiers share the same simple design pattern. It involves the overpro-
925 duction of features followed by a selection strategy. A large number of features (1,000 ~
926 50,000) are generated for each instance. The features are then fed into a simple linear
927 classifier. It determines which features are most useful and returns the final classification
928 result. A ridge classifier is used in this study. It is a linear classifier that extends ridge
929 regression to classification tasks by applying a threshold to the predicted values. It uses
930 L2 regularization to prevent overfitting. The regularization strength is selected by in-
931 ternal cross-validation. A Ridge classifier is suggested for small datasets, as in our case,
932 while a logistic regression classifier is suggested for large datasets [1].

933 While these five classifiers are often referred to as classifiers [1], they are technically
934 time series transformation methods for generating features that are then fed to a down-
935 stream classifier. The comparison of them is shown in Table 3.5. For MiniROCKET
936 and MultiROCKET, the bias is determined from the convolution output, and the di-
937 lation depends on the length of the input time series [42, 43]. The main differences
938 among ROCKET-based classifiers lie in how the summary features are generated. The
939 generation of the summary features depends on:

- 940 1. Kernels, which are defined based on the parameters, which consist of kernel length,
941 kernel weights, bias, and dilation.

- | | |
|---|------------|
| 2. The way that padding applies to T , which leads to activation maps with different lengths. | 942
943 |
| 3. The pooling operations, which are used in extracting features on the activation map. | 944
945 |

	ROCKET	MiniROCKET	MultiROCKET	Hydra
kernel length	$\{7, 9, 11\}$	9	9	9
kernel weights	$\mathcal{N}(0, 1)$	$\{-1, 2\}$	$\{-1, 2\}$	$\mathcal{N}(0, 1)$
bias	$\mathcal{U}(0, 1)$	from output	from output	none
dilation	random	fixed (input-relative)	fixed (input-relative)	random
padding	random	fixed	fixed	always
pooling operations	MAX, PPV	PPV	PPV, MPV, MIPV, LSPV	Response per Kernel/Group
1 st order difference	no	no	yes	yes
feature vector size	20k	10k	50k	relative to input

Table 3.5: Comparison of rocket-based classifiers [1]. $\mathcal{N}(0, 1)$: a standard normal distribution, $\mathcal{U}(0, 1)$: a uniform distribution between 0 and 1, 1st order difference: $\Delta T = t_2 - t_1, t_3 - t_2, \dots, t_n - t_{n-1}$.

3.2.4 Evaluation Metrics

To evaluate the performance of our time series-based classification (MTSC) model, we adopted five standard classification metrics. They are Accuracy (Acc), Specificity (Sp), Sensitivity (Sn), F1 score (F1), and Matthews Correlation Coefficient (MCC) [45].

$$\begin{aligned} Acc &= \frac{TP + TN}{TP + TN + FP + FN} \\ Sp &= \frac{TN}{TN + FP} \\ Sn &= \frac{TP}{TP + FN} \\ F1 &= \frac{2 \times TP}{2 \times TP + FP + FN} \\ MCC &= \frac{TP \times TN - FP \times FN}{\sqrt{(TP + FP)(TP + FN)(TN + FP)(TN + FN)}} \end{aligned}$$

where TP, TN, FP, and FN are the number of true positives, true negatives, false positives, and false negatives, respectively.

To extend a binary metric to multi-class problems, we can treat the data as a collection of binary problems, one for each class. One class is treated as positive while the other classes are treated as negative. Then, the multi-class metrics can be obtained by averaging binary metric calculations across the set of classes. There are different ways of doing the averaging. Here, we adopted a macro-averaging approach. It treats each class equally and calculates the mean of the binary metrics. To use MCC in the multiclass case, it

958 can be defined in terms of a confusion matrix C for K classes, where $C_{i,j}$ is the number
959 of observations that are actually in class i and predicted to be in class j [46].

$$MCC_{multi} = \frac{c \times s - \sum_k^K p_k \times t_k}{\sqrt{(s^2 - \sum_k^K p_k^2) \times (s^2 - \sum_k^K t_k^2)}}$$

960 where $t_k = \sum_i^K C_{i,k}$ (denoting the number of times class k actually occurred), $p_k =$
961 $\sum_i^K C_{k,i}$ (denoting the number of times class k was predicted), $c = \sum_k^K C_{k,k}$ (denoting
962 the total number of samples correctly predicted) and $s = \sum_i^K \sum_j^K C_{i,j}$ (denoting the total
963 number of samples).

964 3.3 Results

965 The code implementing our method is available at <https://github.com/colemanyu/time-series-classification-cleavage>. The dataset of this study is available at
966 <https://www.mirbase.org>.

968 In all experiments, the models were trained and tested using 5-fold cross-validation.
969 We retrieved 827 empirically validated sequences of pre-miRNAs. There are 5p arm
970 and 3p arm in each sequence. For each arm, we defined a cleavage pattern and a non-
971 cleavage pattern. Three datasets, namely “5p arm”, “3p arm”, and “multi-class” were
972 constructed by these patterns. We refer to the cleavage patterns as positive instances
973 and the non-cleavage patterns as negative instances. The 5p arm dataset comprises 827
974 positive instances and an equal number of negative instances. The 5p arm and 3p arm
975 datasets are binary-class datasets. The multi-class dataset comprises all patterns from
976 both the 5p arm and the 3p arm. There are 827 “5p” instances¹¹, 827 “3p” instances,
977 and 1,654 negative instances.

978 For every fold in 5-fold cross-validation, the dataset was divided into a training set
979 and a test set with sizes of 80% and 20% of the whole dataset, respectively. We kept the
980 class distribution approximately the same in each fold, since it is in the original dataset.
981 In each fold derived from the 5p arm and 3p arm datasets, the training set has a size of
982 1,323, and the test set has a size of 331. In each fold derived from the multi-class dataset,
983 the training set has a size of 2,262, and the test set has a size of 662. We reported the
984 average of the five classification metrics.

985 The ROCKET-based classifiers require all channels in the multivariate time series to
986 have equal length. We applied padding to the shorter channels using the constant value
987 100, which does not appear in the original time series. It ensures the padding does not
988 introduce ambiguity or interfere with the semantic meaning of the encoded nucleotide
989 signals.

¹¹Cleavage patterns from the 5p arm.

3.3.1 Channel Ablation Study

We utilized three types of data as the input features for each instance. They are (1) the RNA sequence, which consists of the primary strand and its complementary strand, (2) the secondary structure information, and (3) the base-pair probability sequence. To input the data into our time series-based classifiers, we converted them into multivariate time series. The primary strand and its complementary strand are each encoded into one or two channels, using the encoding methods in Table 3.4. For example, single value mapping encodes a strand in one channel, while grouped variable-length channel mapping encodes in two channels. The secondary structure information is converted into a univariate time series. The base-pair probability sequence is already in numerical form and does not require further transformation. It can be used either as a standalone channel or incorporated into the encoding of the complementary strand. We performed a channel ablation study to determine the most informative combination of the above channels.

We referred to the multivariate time series that consists of the channels from the RNA sequence only as the baseline setting. We added the other channels to this baseline. It leads to the following configurations (cfgs):

1. (cfg 1) Baseline: Time series derived only from the RNA sequence.
2. (cfg 2) Baseline + Secondary structure: Baseline + time series representation of the secondary structure.
3. (cfg 3) Baseline + Base-pair probability (Standalone): Baseline + the base-pair probability sequence as a standalone channel.
4. (cfg 4) Baseline + Base-Pair probability (Incorporated): Baseline with the base-pair probability sequence incorporated into the encoding of the complementary strand.

Classifier	5p arm					3p arm					multi-class					
	Acc	Sp	Sn	F1	MCC	Acc	Sp	Sn	F1	MCC	Acc	Sp	Sn	F1	MCC	
Baseline (cfg 1)	ROCKET	0.781	0.743	0.819	0.789	0.563	0.790	0.773	0.807	0.793	0.580	0.717	0.838	0.685	0.700	0.538
	MiniROCKET	0.755	0.728	0.782	0.762	0.512	0.788	0.781	0.794	0.789	0.576	0.685	0.823	0.653	0.662	0.486
	MultiROCKET	0.784	0.767	0.801	0.787	0.569	0.803	0.792	0.814	0.805	0.606	0.691	0.830	0.667	0.672	0.501
	Hydra	0.830	0.800	0.860	0.835	0.663	0.808	0.797	0.820	0.810	0.617	0.731	0.844	0.696	0.712	0.560
	MultiROCKET-Hydra	0.796	0.778	0.815	0.800	0.594	0.807	0.767	0.816	0.808	0.614	0.701	0.836	0.681	0.686	0.520
Baseline + Secondary Structure (cfg 2)	ROCKET	0.847	0.832	0.862	0.849	0.695	0.855	0.842	0.868	0.857	0.711	0.836	0.907	0.828	0.833	0.736
	MiniROCKET	0.825	0.807	0.843	0.827	0.652	0.822	0.802	0.843	0.826	0.646	0.823	0.900	0.812	0.818	0.715
	MultiROCKET	0.812	0.803	0.822	0.814	0.626	0.824	0.809	0.839	0.826	0.649	0.796	0.888	0.791	0.792	0.673
	Hydra	0.845	0.816	0.873	0.849	0.691	0.846	0.817	0.874	0.850	0.693	0.830	0.901	0.814	0.826	0.724
	MultiROCKET-Hydra	0.817	0.809	0.826	0.819	0.635	0.825	0.816	0.834	0.826	0.652	0.803	0.891	0.798	0.800	0.684
Baseline + Base-pair probability (Standalone) (cfg 3)	ROCKET	0.842	0.828	0.855	0.844	0.684	0.855	0.856	0.854	0.855	0.710	0.795	0.885	0.783	0.789	0.670
	MiniROCKET	0.817	0.820	0.814	0.816	0.634	0.836	0.834	0.838	0.836	0.673	0.772	0.872	0.757	0.764	0.632
	MultiROCKET	0.822	0.813	0.832	0.824	0.645	0.825	0.831	0.820	0.824	0.651	0.758	0.866	0.747	0.750	0.612
	Hydra	0.846	0.827	0.865	0.849	0.693	0.851	0.840	0.861	0.852	0.702	0.789	0.879	0.769	0.780	0.658
	MultiROCKET-Hydra	0.822	0.809	0.834	0.824	0.644	0.835	0.840	0.830	0.834	0.670	0.759	0.866	0.746	0.750	0.611
Baseline + Base-pair probability (Incorporated) (cfg 4)	ROCKET	0.799	0.771	0.827	0.805	0.600	0.809	0.786	0.832	0.813	0.619	0.737	0.850	0.712	0.724	0.573
	MiniROCKET	0.776	0.756	0.797	0.781	0.554	0.801	0.808	0.794	0.799	0.603	0.705	0.835	0.675	0.684	0.521
	MultiROCKET	0.814	0.801	0.828	0.817	0.630	0.816	0.812	0.820	0.816	0.634	0.726	0.848	0.706	0.712	0.556
	Hydra	0.822	0.787	0.857	0.828	0.647	0.834	0.828	0.840	0.835	0.669	0.759	0.862	0.734	0.746	0.608
	MultiROCKET-Hydra	0.814	0.802	0.820	0.817	0.629	0.820	0.825	0.816	0.819	0.642	0.736	0.853	0.717	0.723	0.874

Table 3.6: Channel ablation study. The best results are highlighted in **bold**.

1013 We used single value mapping as the encoding method. Table 3.6 shows the result.
 1014 From the table, we can see that the addition of secondary structure, base-pair probability
 1015 as a standalone channel, and base-pair probability incorporated in the encoding of the
 1016 complementary strand can improve the performance. We plotted the critical difference
 1017 (CD) diagram as shown in Figure 3.6 to visualize Table 3.6 to make the performances
 1018 of different combinations more obvious. In CD diagrams, lower-ranked methods (toward
 1019 the right) are better. A horizontal bar connecting combinations indicates no statistically
 1020 significant difference.

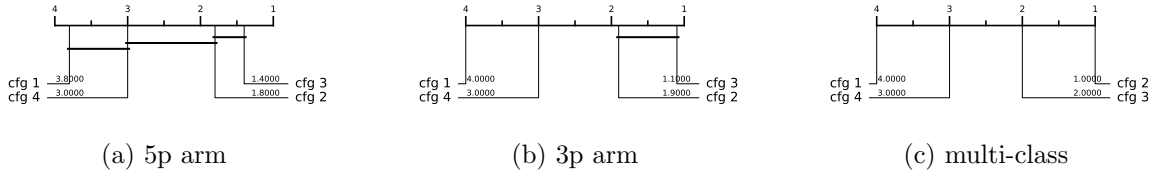


Figure 3.6: CD diagrams of channel ablation study.

1021 From Figure 3.6, we can see that including time series derived from secondary struc-
 1022 ture information and base-pair probability as a separate channel can significantly improve
 1023 the performance of the classifiers. Incorporating the base-pair probability sequence in the
 1024 time series encoding of the complementary strand can also improve the classifier, but to
 1025 a minor degree compared to serving as a standalone channel. In our downstream analy-
 1026 sis, we adopted the combination of RNA sequence time series, secondary structure time
 1027 series, and base-pair probability time series as our multivariate time series input, with 4
 1028 to 6 channels, depending on the encoding used.

1029 3.3.2 Predictive Performance

1030 The experiment was conducted on three datasets: the 5p arm, the 3p arm, and the
 1031 multi-class datasets. Recall that we have nine encoding methods and five ROCKET-
 1032 based classifiers. It results in 45 combinations of encoding methods and classifiers.

1033 The result is shown in Table 3.7. The best combination of encoding method and
 1034 classifier is shown in Table 3.8. For the 5p arm dataset, the best combination is “Global
 1035 Cumulative grouped fixed-length channel mapping + ROCKET”. For all five classifica-
 1036 tion metrics, it outperforms the state-of-the-art (SOTA) method, DiCleave. For the 3p
 1037 arm dataset, the best combination is “Global Cumulative grouped fixed-length channel
 1038 mapping + ROCKET”. Out of the five classification metrics, it outperforms DiCleave,
 1039 except in specificity. For the multi-class dataset, the best combination is “Global Cu-
 1040 mulative grouped fixed-length channel mapping + ROCKET”. For all five classification
 1041 metrics, it outperforms DiCleave. Note that for the 3p arm and the multi-class datasets,

	Classifier	5p arm					3p arm					multi-class				
		Acc	Sp	Sn	F1	MCC	Acc	Sp	Sn	F1	MCC	Acc	Sp	Sn	F1	MCC
Single value mapping (enc 1)	ROCKET	0.849	0.842	0.857	0.851	0.699	0.863	0.854	0.873	0.865	0.727	0.853	0.917	0.847	0.851	0.764
	MiniROCKET	0.823	0.809	0.837	0.825	0.647	0.823	0.828	0.817	0.822	0.647	0.835	0.906	0.828	0.833	0.735
	MultiROCKET	0.821	0.802	0.840	0.824	0.643	0.839	0.826	0.852	0.841	0.679	0.811	0.894	0.806	0.809	0.697
	Hydra	0.843	0.820	0.867	0.847	0.688	0.838	0.819	0.857	0.841	0.677	0.831	0.901	0.815	0.827	0.727
	MultiROCKET-Hydra	0.820	0.803	0.837	0.823	0.640	0.840	0.830	0.850	0.841	0.680	0.816	0.896	0.810	0.814	0.704
Grouped variable-length channel mapping (enc 2)	ROCKET	0.835	0.826	0.844	0.836	0.670	0.855	0.849	0.861	0.856	0.710	0.846	0.913	0.839	0.844	0.752
	MiniROCKET	0.843	0.833	0.853	0.844	0.686	0.831	0.821	0.842	0.833	0.663	0.837	0.907	0.828	0.834	0.737
	MultiROCKET	0.819	0.809	0.828	0.820	0.638	0.817	0.814	0.820	0.818	0.634	0.890	0.894	0.806	0.808	0.695
	Hydra	0.825	0.780	0.869	0.832	0.653	0.811	0.769	0.854	0.819	0.626	0.818	0.892	0.765	0.812	0.705
	MultiROCKET-Hydra	0.818	0.814	0.822	0.819	0.636	0.831	0.825	0.837	0.832	0.662	0.820	0.900	0.815	0.818	0.710
Grouped fixed-length channel mapping (enc 3)	ROCKET	0.851	0.843	0.859	0.852	0.702	0.863	0.850	0.875	0.864	0.726	0.849	0.915	0.843	0.847	0.757
	MiniROCKET	0.844	0.836	0.853	0.845	0.689	0.840	0.826	0.855	0.843	0.682	0.851	0.915	0.844	0.849	0.760
	MultiROCKET	0.831	0.815	0.848	0.834	0.663	0.824	0.813	0.836	0.826	0.649	0.811	0.896	0.808	0.808	0.698
	Hydra	0.848	0.816	0.880	0.853	0.699	0.862	0.839	0.884	0.864	0.724	0.843	0.908	0.837	0.839	0.746
	MultiROCKET-Hydra	0.836	0.813	0.859	0.839	0.672	0.833	0.820	0.845	0.835	0.665	0.828	0.905	0.824	0.826	0.725
Cumulative mapping (enc 4)	ROCKET	0.850	0.834	0.866	0.852	0.701	0.863	0.855	0.871	0.864	0.726	0.852	0.915	0.842	0.850	0.762
	MiniROCKET	0.840	0.821	0.860	0.843	0.682	0.840	0.837	0.844	0.841	0.682	0.843	0.911	0.835	0.840	0.747
	MultiROCKET	0.822	0.809	0.834	0.824	0.644	0.832	0.830	0.834	0.832	0.665	0.820	0.898	0.810	0.816	0.709
	Hydra	0.848	0.819	0.878	0.853	0.698	0.853	0.856	0.869	0.855	0.705	0.845	0.910	0.830	0.841	0.749
	MultiROCKET-Hydra	0.824	0.811	0.856	0.825	0.647	0.838	0.833	0.843	0.839	0.677	0.821	0.898	0.810	0.817	0.711
Cumulative grouped variable-length channel mapping (enc 5)	ROCKET	0.843	0.821	0.866	0.847	0.688	0.856	0.840	0.871	0.857	0.712	0.855	0.916	0.843	0.851	0.766
	MiniROCKET	0.845	0.826	0.865	0.848	0.691	0.836	0.833	0.838	0.836	0.672	0.840	0.909	0.833	0.838	0.742
	MultiROCKET	0.826	0.814	0.838	0.828	0.653	0.815	0.820	0.810	0.814	0.631	0.826	0.902	0.820	0.824	0.721
	Hydra	0.850	0.819	0.880	0.854	0.701	0.834	0.807	0.861	0.838	0.669	0.833	0.903	0.818	0.829	0.731
	MultiROCKET-Hydra	0.824	0.810	0.838	0.826	0.649	0.833	0.833	0.833	0.833	0.666	0.830	0.903	0.821	0.827	0.726
Cumulative grouped fixed-length channel mapping (enc 6)	ROCKET	0.856	0.836	0.876	0.858	0.712	0.870	0.861	0.879	0.871	0.741	0.863	0.921	0.852	0.860	0.780
	MiniROCKET	0.856	0.837	0.874	0.858	0.712	0.842	0.839	0.845	0.843	0.685	0.845	0.912	0.837	0.843	0.751
	MultiROCKET	0.820	0.802	0.839	0.824	0.642	0.798	0.798	0.798	0.798	0.597	0.809	0.894	0.806	0.807	0.694
	Hydra	0.850	0.814	0.885	0.855	0.701	0.855	0.840	0.869	0.857	0.711	0.847	0.910	0.831	0.843	0.752
	MultiROCKET-Hydra	0.820	0.801	0.839	0.823	0.641	0.807	0.813	0.802	0.806	0.615	0.821	0.900	0.817	0.819	0.713
Global Cumulative mapping (enc 7)	ROCKET	0.850	0.834	0.866	0.852	0.701	0.863	0.855	0.871	0.864	0.726	0.852	0.915	0.842	0.850	0.762
	MiniROCKET	0.847	0.832	0.862	0.849	0.695	0.848	0.839	0.857	0.850	0.697	0.845	0.911	0.836	0.843	0.750
	MultiROCKET	0.827	0.819	0.834	0.828	0.653	0.847	0.842	0.853	0.848	0.695	0.825	0.901	0.817	0.822	0.718
	Hydra	0.851	0.821	0.880	0.855	0.703	0.861	0.848	0.874	0.863	0.722	0.847	0.911	0.834	0.844	0.753
	MultiROCKET-Hydra	0.829	0.823	0.834	0.830	0.658	0.843	0.838	0.849	0.844	0.688	0.832	0.905	0.823	0.829	0.730
Global Cumulative grouped variable-length channel mapping (enc 8)	ROCKET	0.840	0.814	0.867	0.844	0.682	0.853	0.838	0.867	0.854	0.706	0.856	0.917	0.845	0.853	0.768
	MiniROCKET	0.848	0.834	0.862	0.850	0.697	0.841	0.824	0.859	0.844	0.683	0.844	0.911	0.856	0.842	0.748
	MultiROCKET	0.834	0.828	0.839	0.834	0.668	0.831	0.821	0.842	0.833	0.663	0.828	0.904	0.823	0.826	0.724
	Hydra	0.857	0.821	0.894	0.862	0.717	0.822	0.786	0.857	0.828	0.645	0.826	0.898	0.806	0.820	0.717
	MultiROCKET-Hydra	0.837	0.834	0.839	0.837	0.674	0.834	0.827	0.840	0.835	0.668	0.835	0.907	0.828	0.832	0.734
Global Cumulative grouped fixed-length channel mapping (enc 9)	ROCKET	0.856	0.836	0.876	0.858	0.712	0.870	0.861	0.879	0.871	0.741	0.863	0.921	0.852	0.860	0.780
	MiniROCKET	0.857	0.845	0.870	0.859	0.715	0.840	0.821	0.859	0.843	0.681	0.844	0.911	0.837	0.842	0.749
	MultiROCKET	0.829	0.825	0.833	0.830	0.658	0.820	0.816	0.823	0.820	0.640	0.819	0.900	0.816	0.817	0.710
	Hydra	0.856	0.817	0.894	0.861	0.713	0.859	0.838	0.880	0.862	0.719	0.846	0.911	0.832	0.843	0.752
	MultiROCKET-Hydra	0.829	0.824	0.834	0.830	0.658	0.822	0.825	0.819	0.821	0.644	0.827	0.904	0.823	0.824	0.722

Table 3.7: Performance on the 45 combinations between encoding methods and the ROCKET-based classifiers. The best results are highlighted in **bold**.

the combination of “Cumulative grouped fixed-length channel mapping + ROKCET” 1042 also attains the best result.

1043

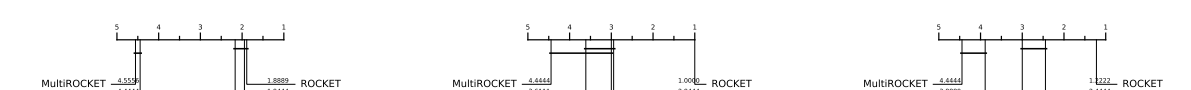


Figure 3.7: CD diagrams to compare different classifiers.

To summarize Table 3.7, we plot the CD diagrams for finding the best classifier, as shown in Figure 3.7, and the best encoding method, as shown in Figure 3.8.

1044

1045

Dataset	Methods	Acc	Sp	Sn	F1	MCC	Time (s)
5p arm	enc 9 + MiniROCKET	0.857	0.845	0.870	0.859	0.715	0.787
	DiCleave	0.818	0.790	0.846	0.822	0.653	21.249
3p arm	enc 9 + ROCKET	0.870	0.861	0.879	0.871	0.741	4.311
	enc 7 + MiniROCKET	0.848	0.839	0.857	0.850	0.697	0.989
	DiCleave	0.854	0.891	0.817	0.847	0.715	15.919
multi-class	enc 9 + ROCKET	0.863	0.921	0.852	0.860	0.780	12.208
	enc 3 + MiniROCKET	0.851	0.915	0.844	0.849	0.760	4.550
	DiCleave	0.820	0.895	0.804	0.815	0.710	131.151

Table 3.8: Comparative analysis between MTSCCleav with the best combination of the encoding method and classifier, with the SOTA, DiCleave, on the three datasets. The best results of using MiniROCKET have also been shown to compare the computational efficiency. The best results are highlighted in **bold**.

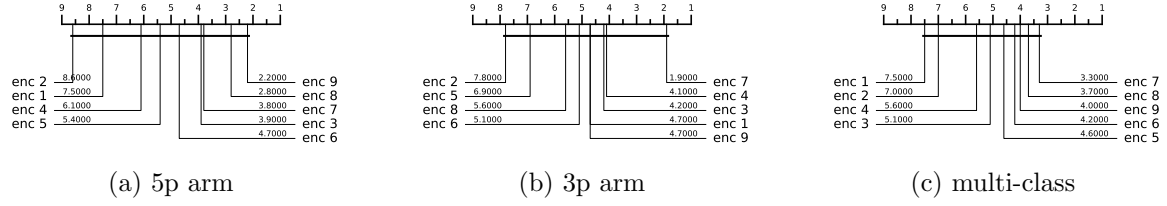


Figure 3.8: CD diagrams to compare different encoding methods.

3.3.3 Running Time Analysis

To compare the computational efficiency of MTSCCleav and DiCleave, we conducted a comparative analysis of their running times. For DiCleave, we employed the code from its supporting website¹², without any modifications. All experiments were conducted on the same machine (a personal laptop equipped with an Apple M1 Pro chip and 16 GB of memory) and using the same splits of the training and test datasets under 5-fold cross-validation to ensure fairness. The reported running times are the averages of the five runs. The timing results were measured from the training phase to the return of the five classification metrics. The result is shown in Table 3.8. MiniROCKET is the most computationally efficient of the five rocket-based classifiers. We also included its best result, along with the corresponding encoding method, even though this combination may not be the best overall.

MTSCCleav demonstrated a significant advantage in computational efficiency, achieving an average 27.0X, 3.7X, and 10.7X speedup over DiCleave, for the 5p arm, 3p arm, and multi-class datasets, respectively. If we consider using the MiniROCKET in the case of 3p arm and multi-class datasets, it achieves 16.1X and 28.8X speedup. To note, in the

¹²

<https://github.com/MGuard0303/DiCleave> (Accessed on: 2025-07-13).

case of the 3p arm dataset, the performance of MiniROCKET is only slightly worse than 1062
DiCleave. In the case of the multi-class dataset, even the performance of MiniROCKET 1063
is better than DiCleave. DiCleave is a deep learning-based method that requires sub- 1064
stantial time for model inference, while MTSCleav leverages efficient ROCKET-based 1065
classifiers. This significant reduction in runtime makes MTSCcleav more suitable for 1066
large-scale data and real-time applications. 1067

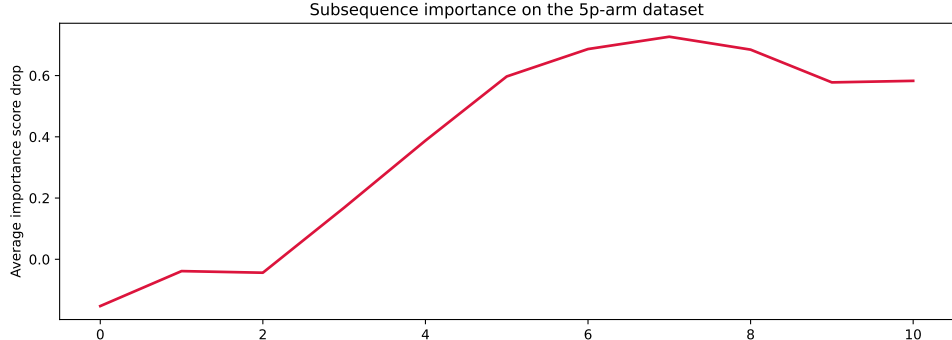
3.3.4 Subsequence Importance

To evaluate the sensitivity of MTSCcleav to subsequences of the input, we conducted a 1069
perturbation experiment to evaluate the importance of subsequences based on masking 1070
windows. The goal of this experiment is to identify which subsequences of the entire 1071
time series are critical for classification. We examine how various modifications to the 1072
original input impact model performance. It suggests which features are essential for 1073
classification. 1074

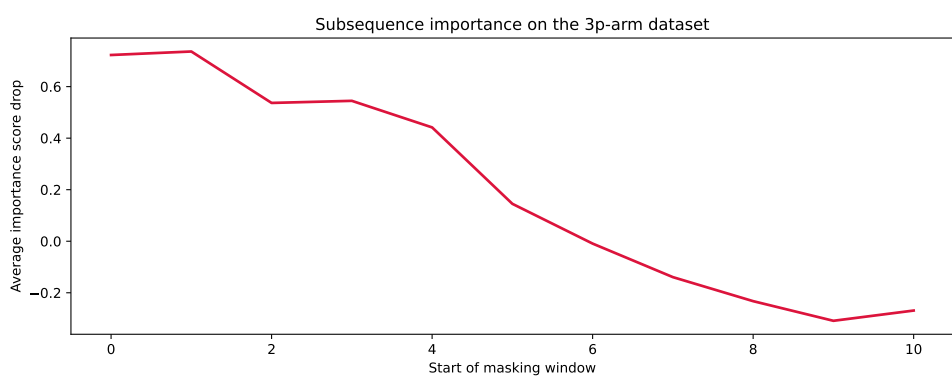
The model was trained on the original training dataset. For each instance in the test 1075
dataset, we measure its original score and the masked score. We slid a masking window 1076
 w with a fixed length over the input time series T . $|w|$ was set to 4. For each window 1077
position $i \in \{1, 2, \dots, |T| - |w| + 1\}$, we masked all entries across all the channels of T 1078
within the window. Hence, we removed or hid that portion of information from the model 1079
during inference. The changes in classification performance in terms of accuracy relative 1080
to the unmasked original score of each i are recorded. Intuitively, if the information of a 1081
subsequence is critical for the classification, the masking of this subsequence would lead 1082
to a great drop in classification performance. We aggregated the importance score across 1083
the test dataset. 1084

The result is shown in Figure 3.9. For the encoding methods, we cannot use the 1085
methods derived from the cumulative mapping because the accumulation would leak in- 1086
formation from the masked region. We adopted “Grouped fixed-length channel mapping” 1087
as the encoding method and ROCKET as the classifier. “Grouped fixed-length channel 1088
mapping” is the best encoding, other than the methods derived from the cumulative map- 1089
ping, in all datasets, as shown in Figure 3.8. ROCKET is the best classifier, as shown in 1090
Figure 3.7. 1091

In the 5p arm dataset, we found that masking subsequences at the tailing part caused 1092
a significant drop in the importance score, as shown in Figure 3.9 (a). In the 3p arm 1093
dataset, we found that masking subsequences at the leading part caused a significant 1094
drop in the importance score, as shown in Figure 3.9 (b). 1095



(a) 5p arm



(b) 3p arm

Figure 3.9: Results of the perturbation experiment.

3.3.5 Summary

Our method achieves better or comparable predictive results and a 3.7X to 28.8X speedup compared to the state-of-the-art (SOTA).

3.4 Discussion

The channel ablation study reveals that the involvement of the time series derived from the secondary structure can improve accuracy. It suggests the importance of RNA folding in dicer processing. Furthermore, we found that the base-pair probability sequence of the secondary structure can also enhance accuracy. To the best of our knowledge, it is a novel application of the base-pair probability sequence. Experiments show that using the probability sequence as an additional channel can enhance accuracy more than incorporating it in the encoding. It is likely because keeping it as an additional channel can preserve more information, of both the probability sequence itself and the complementary strand.

Out of the three datasets, the best classifier is ROCKET. The ranking of the five classifiers by performance, starting from the best, is as follows: ROCKET, Hydra, MiniROCKET, MultiROCKET-Hydra, and MultiROCKET. It indicates that the fea-

tures created from the pooling operations that are only in MultiROCKET but not in MiniROCKET, confuse the final classifier. They are mean of positive values (MPV), mean of indices of positive values (MIPV) and longest stretch of positive values (LSPV) [43]. In contrast, the pooling operator that is only present in ROCKET but not in MiniROCKET, enhances the classification performance. It is maximum (MAX). 1111
1112
1113
1114
1115

For the encoding methods, we have the following observations. Fixed-length grouped channel mappings outperform variable-length counterparts with one exception in the multi-class dataset, likely because fixed-length schemes better preserve the original positional information of nucleotides within the sequence. Global cumulative methods consistently yield better performance than local cumulative methods. It suggests that the upstream information of the cleavage pattern plays a critical role in identifying cleavage sites. Cumulative-based encodings perform better than single-value mappings, with one exception in the 3p dataset, suggesting that the accumulated nucleotide signal is more informative for cleavage site prediction than the local or isolated presence of nucleotides. In the 5p arm dataset, encoding RNA sequence in two channels appears to worsen the result. This suggests that the 5p arm dataset and the 3p arm dataset need different nucleotide grouping methods for the encoding. 1116
1117
1118
1119
1120
1121
1122
1123
1124
1125
1126
1127

One limitation of DiCleave is overfitting during training because of the relatively small size of the dataset [21]. DiCleave is a deep learning-based method. Deep learning models typically require a large amount of training data to generalize effectively. They are data-hungry. In contrast, MTSCCleav leverages ROCKET-based methods for the classification. They rely on random convolutional feature extraction followed by a simple linear classifier. The Ridge classifier used in this study is less data-hungry compared to deep learning methods due to its use of L2 regularization and the simplicity of its linear model nature. It allows ROCKET-based classifiers, and hence MTSCCleav, to maintain strong predictive performance even in settings with a relatively small dataset size. 1128
1129
1130
1131
1132
1133
1134
1135
1136

The subsequence importance reveals some connections between RNA secondary structure and human dicer cleavage site prediction. The perturbation experiment shows that the leading part of 5p arm and the tailing part of 3p arm are important for the classification. These parts are close to the center of the RNA secondary structure of pre-miRNA. It indicates that the center region is more crucial for human dicer cleavage site prediction. It is consistent with the previous study [20]. 1137
1138
1139
1140
1141
1142

3.5 Concluding Remarks 1143

We proposed an accurate, fast, and simple multivariate time series classification (MTSC)-based method, termed MTSCCleav, for predicting human dicer cleavage sites. Base-pair probability sequences of the secondary structures have also been leveraged in the classification. MTSCCleav consists of three parts: time series encoding, time series 1144
1145
1146
1147

transformation, and classification. ROCKET-based methods were used for time series transformation. Ridge Classifier was used for classification. For the computational experiments, we evaluated nine time series encoding methods in conjunction with five time series transformation methods. MTSCCleav outperformed the SOTA method in all five evaluation metrics for the 5p-arm and multi-class datasets, and four of the metrics for the 3p-arm dataset. In terms of computational efficiency, MTSCCleav with the optimal setting achieved an average 3.7X to 27.0X speedup over the SOTA method on the three datasets. With the use of a less accurate but faster time series classification method, MTSCCleav achieved an average speedup of 16.1X to 28.8X, respectively. We analyzed the subsequence importance of the input multivariate time series. The results show that subsequences near the center of the pre-miRNA sequences are more important. This aligns with the findings from previous work. This study demonstrates that time series analysis provides a powerful alternative to conventional modeling in the context of RNA processing. This framework may be extended to other RNA-processing tasks. Notably, the encoding of RNA sequence into time series enables us to utilize any well-established tools from the time series community.

Chapter 4

1164

Scaling with Multiple Scaling

1165

Factors in Time Series Searching

1166

Time series data are ubiquitous across many different fields. Many data mining tasks, such as classification, clustering, and motif finding, have been defined for time series data. They utilize similarity search as a core subroutine, making it crucial to design similarity measures that align with our intuitions. To facilitate efficient computation, speedup techniques are essential. Dynamic Time Warping (DTW) is arguably the most prevailing distance measure for time series data. However, studies have shown that for certain data, another distance measure, namely Uniform Scaling (US), is equally crucial as DTW. DTW handles the local distortion, while US handles the global scaling. In addition, studies have demonstrated that combining DTW and US is necessary to obtain meaningful results in some cases. Surprisingly, all existing studies employ only a single scaling factor for the entire time series. A time series could consist of phases. Since each phase of a time series expresses at its own rate, using a single scaling factor is insufficient when comparing two time series that share similar phases but differ in their expression rates. We introduce the first framework that accounts for multiple scaling factors, Piecewise Scaling Distance (PSD). PSD employs other existing distance measures as subroutines. Because the naive implementation of PSD is slow, we propose a constrained version of PSD that enforces constraints based on the allowed segment lengths derived from the given scaling factor bound. It also prevents pathological results. In addition, two other speedup techniques have been proposed, which achieve 10.10X to 191.46X speedup. We also demonstrate the usage of a lower bound when DTW is used as the subroutine of PSD. Moreover, we show that the segmentation results returned by PSD can improve the accuracy of other distance measures.

1188

1189 **4.1 Background**

1190 To study the mechanism of a process, we take measurements. Measurements are usually
1191 taken continuously by the sensors. Measurements of processes always yield continuous
1192 values at discrete timestamps. They are time series data. For example, smartphones
1193 collect users' GPS data. ECG monitors measure patients' heart rate. The continuous
1194 measurements compose a time series. It is not hard to see why time series data are
1195 ubiquitous across many different fields. In GPS data, each time series data point consists
1196 of the user's latitude and longitude information. They are multivariate time series. In
1197 ECG data, each data point represents the amplitude of the patient's cardiac electrical
1198 activity. They are univariate time series. In this study, we focus on univariate time series.

1199 Many data mining tasks can be defined on time series data. For example, given a
1200 time series database, we can perform clustering based on the pairwise similarity of the
1201 time series instances. A classifier can be trained when categorical labels are available.
1202 Alternatively, given a long time series, for motif finding, we identify recurring patterns.
1203 In contrast, for anomaly detection, we identify abnormal subsequences. Almost all time
1204 series data mining tasks can be reduced to arguing the similarity between two time series.
1205 A good distance measure, also known as a similarity measure, can determine the success
1206 or failure of the algorithms built on it. The choice of an appropriate distance measure is
1207 particularly evident in classification. Studies show that simple nearest-neighbor classifi-
1208 cation (1-NN) is difficult to beat and can compete with more complex methods [39].

1209 A time series is treated as a whole rather than as a collection of individual values.
1210 The relationships between values are important. They constitute trends and shapes.
1211 Hence, similarity search in time series data is approximate-based rather than exact match-
1212 based [47]. Besides, different invariances should be allowed during the comparison.

1213 Dynamic Time Warping (DTW) is one of, if not the most common, similarity mea-
1214 sures. DTW provides invariance to time distortion by aligning and measuring the sim-
1215 ilarity between two series that may be misaligned in time. However, it assumes that
1216 the time series are expressed on a similar global expression rate. This assumption limits
1217 its performance when comparing two time series expressed at different global expression
1218 rates. We often see this behavior in domains such as speech recognition, motion analysis,
1219 patient biomedical signals, and sensor data in the manufacturing industry.

1220 Uniform Scaling (US) can achieve global scaling invariance by scaling the two time
1221 series to the same length via interpolation, such as nearest-neighbor interpolation, before
1222 comparison, as shown in Figures 4.1. It is reported that in some domains, such as
1223 gestures [48, 49] and music performance [50], the scaling is about 10-15% (i.e., scaling
1224 factors: 1.1 to 1.15). The scaling factors are relatively small, since the nature of the
1225 music and the gait will change with significant scaling factors. However, in some other
1226 domains, we may encounter larger scaling factors. In bioinformatics, gene expression time

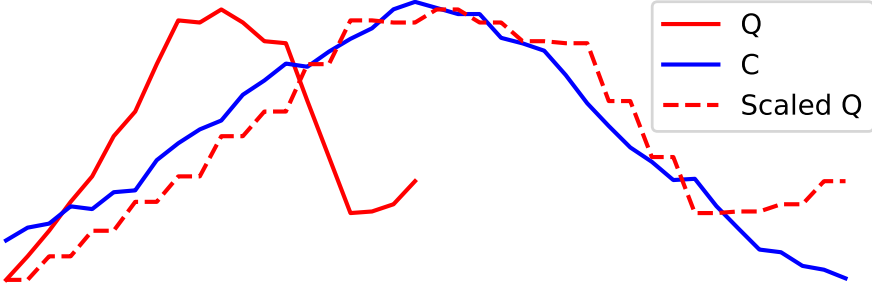


Figure 4.1: Applying nearest neighbor interpolation on Q , which result in Scaled Q , that can better reflect its similarity with C .

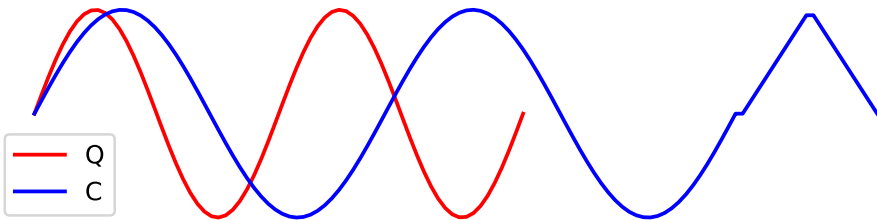


Figure 4.2: Q and C are in different rates. A stretching version of Q is similar to a prefix of C , but not the whole C .

series data could differ by a factor of 1.41 [51, 52]. In Figure 4.2, Q and a prefix of C 1227
are similar, but at different rates. In searching, we typically have a query Q and a longer 1228
candidate C . We seek a prefix of C that is close to Q . For better comparison, we need 1229
to eliminate the scaling effect. These observations demonstrate the necessity of uniform 1230
scaling. 1231

DTW and US are used to achieve different kinds of invariance. DTW handles local 1232
distortion, while US handles global scaling. Furthermore, some studies show that the 1233
combination of US and DTW, namely USDTW, better reflects similarity [53, 54, 55]. US 1234
is first applied to transform the two time series into the same length to eliminate the effect 1235
resulting from the different rates. Then, DTW, rather than ED, is applied to address 1236
local misalignment. USDTW is computationally more expensive than DTW because it 1237
involves the calculation of the DTW between Q and different lengths of each prefix of C . 1238
The different lengths of the prefixes correspond to different scaling factors. 1239

It is not uncommon for the data sampling strategy to change over time [56]. There are 1240
different phases, each with its own rate. To achieve invariance for this kind of scaling effect 1241
resulting from multiple rates, rather than using a single scaling factor, it is beneficial to 1242
identify these different phases and use the appropriate scaling factors for these segments, 1243
also known as pieces. We refer to this as piecewise scaling (PS). Figure 4.3 shows the 1244
intuition of PS. The prefix of C (i.e., $C(1 : k)$) and Q share the same set of segments, 1245
but each has a different scaling. Multiple scaling factors must be used. It motivates us 1246

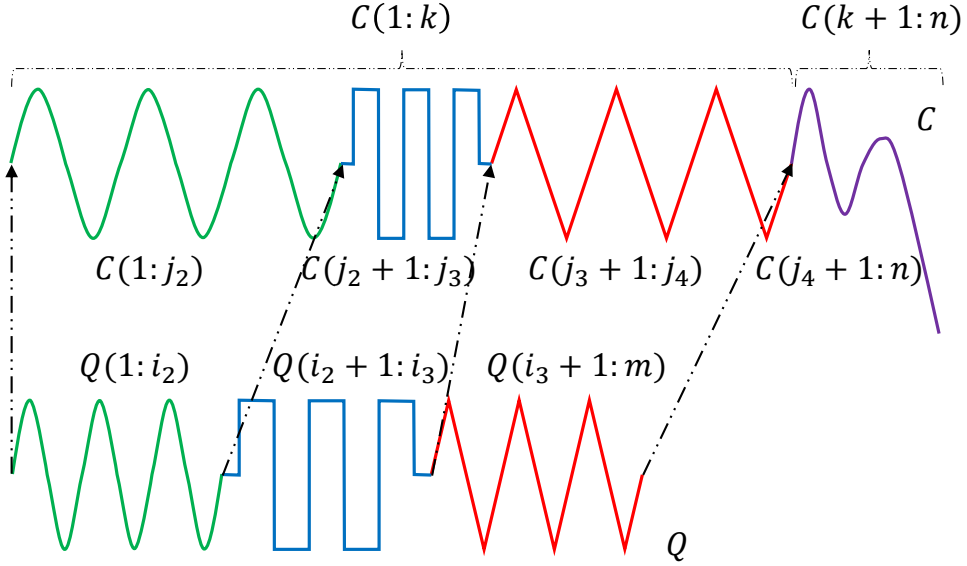


Figure 4.3: Intuition of piecewise scaling (PS).

1247 to design a new distance measure or framework that considers applying a scaling factor
 1248 on each of the phases as defined by dashed lines in Figure 4.3, during the comparison of
 1249 two time series.

1250 Our contributions are as follows:

- 1251 • We propose the first framework to achieve piecewise scaling (PS) invariance. In
 1252 particular, we focus on two instantiations of PSD, namely PSED (i.e., ED with PS
 1253 invariance) and PSDTW (i.e., DTW with PS invariance).
- 1254 • We design a dynamic programming method to compute PSD.
- 1255 • We propose a constrained version of PSD (cPSD) based on the allowed segment
 1256 lengths. Besides, two other speedup techniques have been proposed. For a partic-
 1257 ular instantiation of PSD, PDTW, we demonstrate the usage of a lower bound to
 1258 further speed it up.
- 1259 • We demonstrate that the segmentation results returned by PSD can improve the
 1260 accuracy of other distance measures.

1261 The rest of this paper is structured as follows. We present related work in Section 5.2
 1262 and preliminaries in Section 4.3. Section 5.3 introduces our new distance measure frame-
 1263 work, its constrained version, and speedup techniques. It is experimentally demonstrated
 1264 in Section 4.5 for the problem of querying. In Section 5.5, we conclude this study with
 1265 some future work.

4.2 Related Work

1266

This study focuses on distance measures of time series. For the overall review of time 1267
series, we direct the readers to [47, 57] for a more comprehensive understanding of this 1268
field. 1269

For many tasks, having appropriate distance measures that align with our intuition 1270
for the domains we work with is essential. One well-known distance measure is Dynamic 1271
Time Warping (DTW). It is initially designed for speech analysis [2]. However, DTW 1272
is computationally expensive. Lower bounds are used to speed up time series similarity 1273
search by admissibly pruning the unpromising candidates. One of the popular exact 1274
lower bounds of DTW is LB_{Keogh} . [58] improves the scalability of DTW by introducing a 1275
subsequence search suite of their four novel ideas, namely the UCR suite. For an overall 1276
review of lower bounds, we refer readers to [59, 60]. There is an approximate algorithm 1277
that approximates DTW with high accuracy while drastically cutting down the time and 1278
space requirements [61]. 1279

While ED is sensitive to distortions in the time axis, uniform scaling (US) has been 1280
shown to be a critical invariance in domains such as motion capture. [62] demonstrated 1281
that DTW is insufficient for handling global scaling effects, and that identifying DTW is 1282
not the solution to achieve this kind of invariance. There is a need for US. [63] extends 1283
the importance of uniform scaling to motif discovery. The authors show that meaningful 1284
motifs often suffer from a global scaling effect, causing standard motif finding algorithms 1285
to miss them completely. 1286

To the best of our knowledge, three studies analyze the combination of US and DTW, 1287
namely USDTW. It was first proposed by [53]. It extended LB_{Keogh} to bound the US- 1288
DTW. However, the extended LB_{Keogh} is still too loose with invariance to large amounts 1289
of uniform scaling. [54] and its follow-up study [55] proposed a new lower bound ¹, namely 1290
 LB_{Shen} , which has been shown to be tighter than LB_{Keogh} on USDTW. 1291

To our surprise, despite a fruitful discussion of DTW, US, and USDTW, no study has 1292
proposed a distance measure capable of handling scaling effects across multiple scaling 1293
factors. This is precisely what we will address in this study. 1294

4.3 Preliminaries

1295

We refer to time as the contextual attribute because it provides the context for the mea- 1296
surements to be made. We refer to the measurements as the behavioral attributes. Time 1297
series are multivariate when more than one behavioral attribute is present. Otherwise, it 1298
is called univariate. We focus on the univariate case. 1299

¹It is denoted as LB_{New} in the original study. We rename it to prevent any confusion.

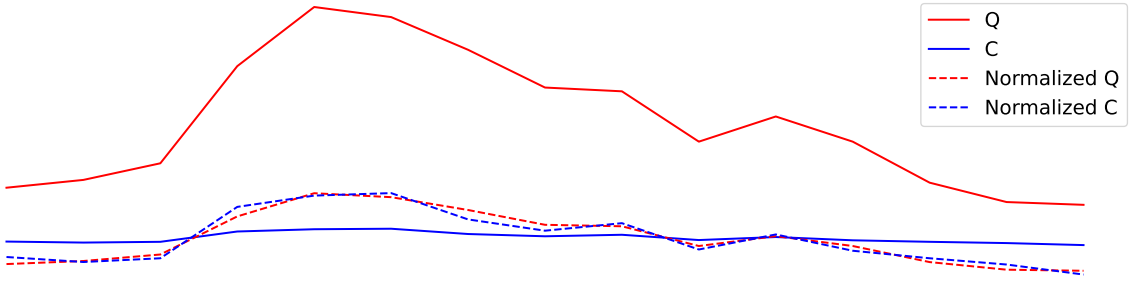


Figure 4.4: Z-normalization. Resulting time series have mean = 0 and std = 1.

1300 **Definition 1** (Time Series). A time series $T = t_1, t_2, \dots, t_n$ is a sequence of real-valued
1301 numbers with length = n .

1302 When two time series are involved in the discussion, we denote them as Q (Query)
1303 and C (Candidate), with lengths m and n , respectively. Since Q is the query sequence,
1304 it is not longer than C (i.e., $m \leq n$). The requirement of “ $m \leq n$ ” is a natural setting.
1305 In “Query by Content”, a user is going to search for a candidate in the database from a
1306 user-input query in which the query may only contain partial information of the target
1307 candidate. For example, a user often wants to find a song or tune that is lingering in
1308 their head by humming a part but not whole of the tune [64]. We are also interested in
1309 a segment or subsequence of a time series.

1310 **Definition 2** (Subsequence). A subsequence $T(i : j)$ of a time series T is a shorter time
1311 series that starts from position i and ends at position j with length = $j - i + 1$. Both
1312 ends are inclusive. Formally, $T(i : j) = t_i, t_{i+1}, \dots, t_j$, $1 \leq i \leq j \leq n$.

1313 We call $T(1 : j)$ the prefix of T of length j .

1314 Before comparison, we need to standardize or normalize them. A common way is
1315 Z-Normalization, which is $T = (T - \text{mean}(T)) / \text{std}(T)$, as shown in Figure 4.4. The most
1316 fundamental distance measure is the Euclidean Distance (ED).

1317 4.3.1 Euclidean Distance (ED)

1318 Given two points on a plane, it is intuitive to define the distance between them as the
1319 length of the line segment between them. This idea extends to the case of n -dimensions
1320 in time series with length n .

1321 **Definition 3** (Euclidean Distance (ED)). Given two series Q and C both with length n ,
1322 the Euclidean Distance between them is defined as:

$$\text{ED}(Q, C) = \sqrt{\sum_{i=1}^n (q_i - c_i)^2} \quad (4.1)$$

A square root is usually involved in the computation of distance measures. It is a ₁₃₂₃ monotonic function. Since it does not change the relative ranking of the results, we can ₁₃₂₄ omit the square root operation for simplicity and optimization. ED aligns the entries ₁₃₂₅ between two series in a one-to-one manner. Two similar series will have a large distance ₁₃₂₆ under ED if they are not aligned well in the time dimension. ED cannot handle local ₁₃₂₇ distortion along the time axis because warping in the alignment is not allowed. A stan- ₁₃₂₈ dard distance measure that provides warping invariance is called Dynamic Time Warping ₁₃₂₉ (DTW). ₁₃₃₀

4.3.2 Dynamic Time Warping (DTW)

Dynamic Time Warping (DTW) is an algorithm that measures similarity between two ₁₃₃₂ time series while accounting for local distortions. DTW aligns the two series by nonlin- ₁₃₃₃ early warping the time axis to minimize the final cumulative distance. ₁₃₃₄

Given two time series, Q and C , we first construct an m by n distance matrix M . ₁₃₃₅ The origin $(1, 1)$ is set at the bottom-left element of M . The (i, j) element of M ₁₃₃₆ contains the distance $d(q_i, c_j)$ between points q_i and c_j . This local distance $d(\cdot, \cdot)$ is ₁₃₃₇ usually calculated by $(q_i - c_j)^2$. Each (i, j) element refers to an alignment or mapping ₁₃₃₈ of the two points. A contiguous set of such elements forms a warping path W . W ₁₃₃₉ represents the non-linear alignment of Q and C . $W = w_1, w_2, \dots, w_K$ in which $w_k = (i, j)_k$ ₁₃₄₀ represents the mapping between q_i in Q and c_j in C , where $\max(m, n) \leq K \leq m + n - 1$. ₁₃₄₁ “ $\max(m, n) \leq K$ ” because the alignment of two series must include every point in both Q ₁₃₄₂ and C . “ $K \leq m + n - 1$ ” because the longest warping path is either the “concatenation of ₁₃₄₃ the bottom row and the rightmost column” (with the bottom-right cell being overlapped) ₁₃₄₄ or the “concatenation of the leftmost column and the top row” (with the top-left cell being ₁₃₄₅ overlapped). ₁₃₄₆

The warping path W is typically subject to the following three constraints. ₁₃₄₇

- Boundary conditions: $w_1 = (1, 1)$ and $w_K = (m, n)$. The first (last) point of Q ₁₃₄₈ must map to that of C . ₁₃₄₉
- Continuity: Given $w_k = (i, j)$ and $w_{k-1} = (i', j')$, $i - i' \leq 1$ and $j - j' \leq 1$. An ₁₃₅₀ entry in the warping path W is adjacent to its one-step previous entry. ₁₃₅₁
- Monotonicity: Given $w_k = (i, j)$ and $w_{k-1} = (i', j')$, $i - i' \geq 0$ and $j - j' \geq 0$. The ₁₃₅₂ warping path W does not go back. ₁₃₅₃

We denote W^* as a set of all allowed possible paths. ₁₃₅₄

Definition 4 (Dynamic Time Warping (DTW) [2]). DTW returns the minimum warping ₁₃₅₅ cost: ₁₃₅₆

$$\text{DTW}(Q, C) = \min_{W \in W^*} \sum_{k=1}^{|W|} w_k \quad (4.2)$$

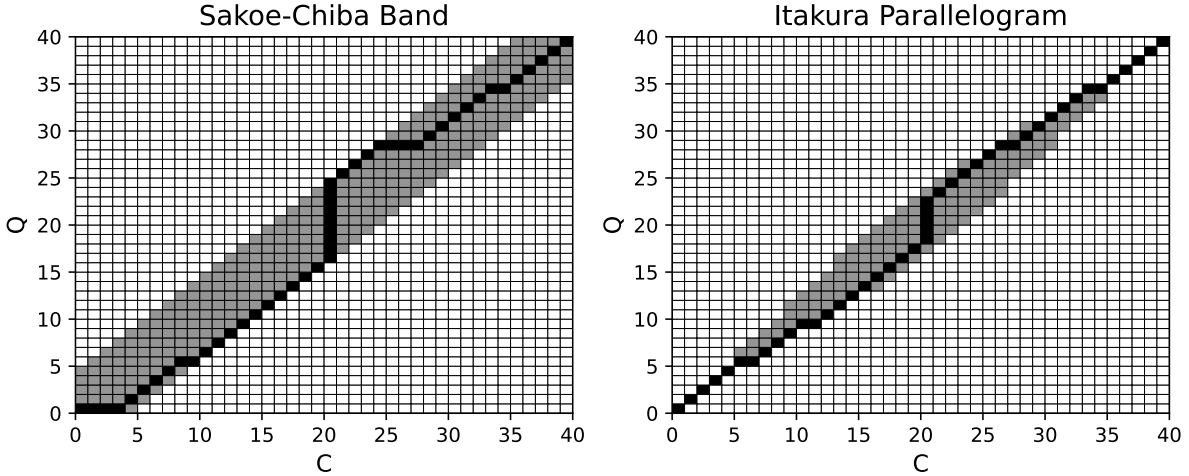


Figure 4.5: Visualization of D with local constraints. The black cells form the warping path.

To find the minimum warping cost and its corresponding warping path, we can use dynamic programming (DP) to evaluate the following recurrence.

$$D(i, j) = d(q_i, c_j) + \min \begin{cases} D(i - 1, j - 1), \\ D(i - 1, j), \\ D(i, j - 1) \end{cases} \quad (4.3)$$

It can be solved by building the accumulated cost matrix D , where the y-axis refers to Q , and the x-axis refers to C . The base cases, which are the first row and the first column, are defined as $D(1, j) = \sum_{k=1}^j d(q_1, c_k), j \in [1, n]$ and $D(i, 1) = \sum_{k=1}^i d(q_k, c_1), i \in [1, m]$. After we have initialized the base cases, we can fill up D starting from the bottom up. There are $m \times n$ entries in D . It takes $\mathcal{O}(mn)$ to fill it up. Once D is built, we can find the path corresponding to this minimum cost by simple backtracking from the end cell $D(m, n)$ to the origin cell $D(1, 1)$.

Some constraints have been proposed to prevent pathological warping paths with the aim of accuracy and efficiency. Two of the most popular are Sakoe-Chiba Band [2] and Itakura Parallelogram [3]. They only allow the warping paths to pass through the allowed region, as shown in Figure 4.5, by setting the cells outside this region in D to have ∞ accumulated distance cost. [65] suggested that these constraints can be viewed as constraints on the warping path entry $w_k = (i, j)_k$. It represents these constraints as inequalities applying to the indices i and j locally, without depending on the main diagonal in D . In the Sakoe-Chiba Band, the constraints can be represented as $j - r \leq$

$i \leq j + r$, where r is an integer. It is sometimes specified as a fraction (or percentage) 1374 of the longer time series length to ensure length invariance. For clarity, we assume r is 1375 an integer unless specified otherwise. This means that q_i can only align with c_j if their 1376 indices differ by at most r . Since r defines the maximum allowed difference between the 1377 mapping indices, $|n - m| \leq r$, to ensure that the end points of Q and C can map. In 1378 the Itakura Parallelogram, r is a function of i rather than a constant value. ED can 1379 be seen as a special case of DTW where the warping path is fixed to be diagonal. q_i 1380 aligns to c_i for every i (i.e., $r = 0$). DTW minimizes over all possible warping paths, 1381 and the warping path of ED is one of them. Because of the band, we only need to fill 1382 up the cells within the band. The complexity is $\mathcal{O}(\#\text{of_cells_inside})$. In the case of the 1383 Sakoe-Chiba Band, the band has a constant width $w = 2r + 1$. The complexity becomes 1384 $\mathcal{O}(w \times \text{length_of_diagonal}) = \mathcal{O}(rn)$. The constrained DTW is denoted as DTW_r . 1385

4.3.3 Uniform Scaling (US)

1386

In US, we compare the whole sequence of Q to a prefix of C , as shown in Figure 4.2. 1387 The two compared sequences are scaled to the same length via interpolation before ED 1388 is applied. A common interpolation method is nearest neighbor interpolation. 1389

Definition 5 (Nearest Neighbor Interpolation). Given a time series T of length n and 1390 an integer L , Nearest Neighbor Interpolation scales T into T^L as follows: 1391

$$T_j^L = T_{\lceil n(j/L) \rceil} \quad \text{where } 1 \leq j \leq L \tag{4.4}$$

We can scale up or down a given series using Equation 4.4, as shown in Example 1. 1392

Example 1. Given a series $T = 1, 2, \dots, 6$ with length $n = 6$. Let $T(1 : 4)$ be the prefix 1393 of T of length $k = 4$ (i.e., $T(1 : 4) = 1, 2, 3, 4$). Given an integer $L = 8$, we compute 1394 $T(1 : 4)^8$ as follows. 1395

$$\begin{aligned} T(1 : 4)^8 &= T_{\lceil 4(1/8) \rceil}, T_{\lceil 4(2/8) \rceil}, T_{\lceil 4(3/8) \rceil}, \dots, T_{\lceil 4(8/8) \rceil} \\ &= T_1, T_1, T_2, \dots, T_4 \\ &= 1, 1, 2, \dots, 4. \end{aligned}$$

When $L > k$, T is said to be stretched. When $L < k$, T is said to be shrunk. 1396

Definition 6 (Uniform Scaling (US) [62]). Given two series Q and C , of length m and 1397 n respectively, and a scaling factor bound l , where $l \geq 1$. Let $C(1 : k)$ be the prefix of 1398 C , where $\lceil m/l \rceil \leq k \leq \min(\lfloor lm \rfloor, n)$, and $C(1 : k)^L$ be a rescaled version of $C(1 : k)$ with 1399 length L , where $L = \min(\lfloor lm \rfloor, n)$. L is called the alignment factor. $\min(\lfloor lm \rfloor, n)$ is the 1400

1401 largest alignment factor.

$$\text{US}(Q, C, l, L) = \min_{k=\lceil m/l \rceil}^{\min(\lfloor lm \rfloor, n)} \text{ED}(Q^L, C(1:k)^L) \quad (4.5)$$

1402 L is set as the largest alignment factor [55] to ensure all the points in Q and $C(1:k)$ are
1403 preserved during interpolation because of up-sampling, and the scaled version of all the
1404 prefixes is going to have the same length (i.e., L), for fair comparison, since comparison
1405 between two longer time series generally results in a larger distance measure. Through
1406 Equation 4.5, we find the minimum value and the corresponding argument (i.e., k) by
1407 checking the minimum value of the ED function from $\lceil m/l \rceil$ to $\min(\lfloor lm \rfloor, n)$. The scaling
1408 factor is defined by the argument minimum value of k . The smaller k is, the more we
1409 need to “stretch” C for Q to compare with $C(1:k)$, which is m/k times.

1410 Consider a time series database D comprising a set of candidate instances, and a
1411 single query series Q . The search task aims to retrieve the most similar instance (or
1412 top- k instances) from D to Q . We maintain Q as a fixed reference and extract only the
1413 prefixes from each instance in D for comparison. Furthermore, to simplify notation, we
1414 apply scaling exclusively to the instances in D , leaving Q unscaled.

1415 4.3.4 Uniform Scaling & Dynamic Time Warping (USDTW)

1416 Uniform Scaling & Dynamic Time Warping (USDTW) measures the similarity by apply-
1417 ing scaling with an appropriate scaling factor on C and then applying DTW. The tail
1418 part of C can be ignored, as shown in Figure 4.2.

1419 **Definition 7** (Uniform Scaling & Dynamic Time Warping (USDTW) [55]). With the
1420 same notations defined in Definition 6,

$$\text{USDTW}_r(Q, C, l, L) = \min_{k=\lceil m/l \rceil}^{\min(\lfloor lm \rfloor, n)} \text{DTW}_r(Q^L, C(1:k)^L) \quad (4.6)$$

1421 where r is the DTW constraint parameter.

1422 We replace the ED function in Equation 4.5 by DTW function to form Equation 4.6.
1423 As mentioned in Section 5.1, there may exist more than one scaling factor. Hence,
1424 both the existing distance measures, US and USDTW, which are designed to handle
1425 only one scaling factor, are insufficient. This motivates us to design a new framework of
1426 distance measures.

4.3.5 Lower Bounds for DTW and USDTW

1427

We first introduce the concept of lower bounds and explain how they can benefit search. 1428 DTW is computationally more expensive than ED. They compute an accumulated cost 1429 matrix of size $m \times n$, where m and n denote the lengths of the two time series. It 1430 results in quadratic complexity. This complexity poses a challenge for similarity search. 1431 The most common approach is to compute a lower bound of the real value, which is 1432 computationally cheap and tight. We can use this lower bound to filter out unpromising 1433 candidates and perform the expensive distance computation only on the small set of 1434 promising candidates. In searching, we would keep track of the best_so_far distance bsf 1435 between the query Q and the testing candidates. When testing a new candidate C , we 1436 first compute the $\text{LB}(Q, C)$. We only compute the actual DTW when $\text{LB}(Q, C) \leq \text{bsf}$. 1437

We then introduce some common lower bounds. 1438

Kim Lower Bound [66]: LB_{Kim} is a simple and fast lower bound of DTW. The 1439 complexity is $O(1)$. It uses the four features in Q and C . We denote t_{-1} as the last point 1440 and t_{\max} (t_{\min}) as the maximum (minimum) point in time series T . 1441

$$\text{LB}_{\text{Kim}} = \max \begin{cases} d(q_1, c_1) \\ d(q_{-1}, c_{-1}) \\ d(q_{\max}, c_{\max}) \\ d(q_{\min}, c_{\min}) \end{cases} \quad (4.7)$$

$d(\cdot, \cdot)$ refers to the local distance used in the point alignment. The first two lines come 1442 from the boundary condition in DTW. The alignment between the first pair of points and 1443 the last pair of points must contribute to the accumulated sum of DTW. Each point in 1444 Q must align with some point in C , and vice versa. Each alignment contributes a local 1445 distance to the final sum. The minimum possible local distance for the alignment of q_{\max} 1446 would be the one aligned with c_{\max} . The same applies to the last line in the equation. 1447

There is a simplification of LB_{Kim} . Only the first and last pair are used in the lower 1448 bound computation. In the normalized time series, the third and fourth rows in Equa- 1449 tion 4.7 should have small values [58]. Ignoring them can improve the complexity from 1450 $\mathcal{O}(n)$ to $\mathcal{O}(1)$. The simplified lower bound is $\text{LB}_{\text{KimFL}} = d(q_1, c_1) + d(q_{-1}, c_{-1})$. 1451

Keogh Lower Bound [65]: LB_{Keogh} builds the upper U and lower envelopes L of 1452 one of the time series out of the two compared sequences. Usually, the envelopes are 1453 constructed for Q instead of C as we will compare one Q against many C 's. Otherwise, 1454 we need to build the envelopes for each candidate instead [58]. 1455

To the best of our knowledge, they are the first to interpret the constraint as a 1456 restriction on the indices of the warping path $w_k = (i, j)_k$ such that $j - r \leq i \leq j + r$, 1457 where r defines the allowable deviation of alignment between q_i and c_j . For ease of 1458

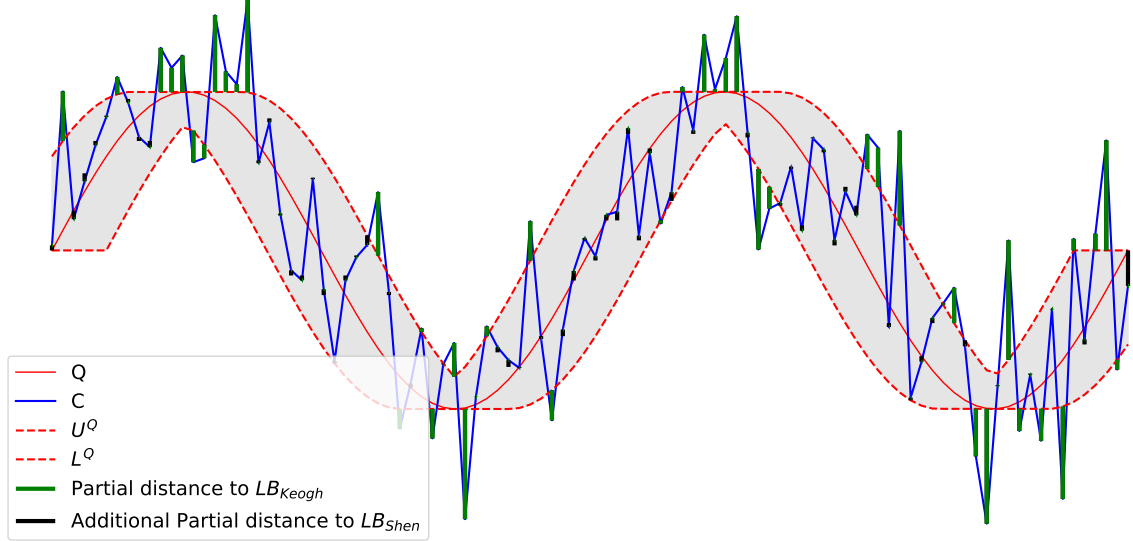


Figure 4.6: Visualization of LB_{Keogh} and LB_{Shen}

exposition, we focus on the most used constraint in the literature, which is the Sakoe-Chiba Band [67]. Two sequences are constructed for Q , namely the upper U^Q and lower envelopes L^Q of Q as shown in Figure 4.6. For each q_i , we would assign a window of q_i based on its index i as follows.

$$\begin{aligned} U_i^Q &= \max(q_{\max(1,i-r)} : q_{\min(i+r,m)}) \\ L_i^Q &= \min(q_{\max(1,i-r)} : q_{\min(i+r,m)}) \end{aligned} \quad (4.8)$$

$\max(1, \cdot)$ and $\min(\cdot, m)$ are used for handling the boundary cases. U^Q and L^Q together form a bounding envelope that encloses the original Q , it is the grey region in the figure. For each c_j , either (c_j, U_j^Q) or (c_j, L_j^Q) corresponds to the possible alignment that contributes the minimum distances if c_j falls outside the envelope. Herein, the lower bound is the sum of these distances, as shown in the following equation.

$$\text{LB}_{\text{Keogh}}(Q, C) = \sum_{j=1}^n \begin{cases} d(c_j, U_j^Q) & \text{if } c_j > U_j^Q \\ d(c_j, L_j^Q) & \text{if } c_j < L_j^Q \\ 0 & \text{otherwise} \end{cases} \quad (4.9)$$

Visually, these distances are the distances between c_j outside the envelope and the vertically corresponding points on the envelope. The distances are the green bars in the figure. Equation 4.9 returns the sum of the green bars.

Shen Lower Bound [54, 55]: It leverages the boundary and continuity conditions to create a lower bound of DTW. It can be used to lower-bound the USDTW with slight modification. The intuition is to find the minimum possible alignment of each c_j with

points in Q , subject to the local constraint r from DTW and the global constraint l from US. 1474
1475

We will first introduce LB_{Shen} for DTW. Given the candidate sequence C with length n , for each c_j , we create its possible reach \mathbf{q}_j in Q under DTW as in Equation 4.10. The elements \mathbf{q}_j form an indexed collection $\mathbb{Q} = (\mathbf{q}_1, \mathbf{q}_2, \dots, \mathbf{q}_{\min(\lfloor lm \rfloor, n)})$. 1476
1477
1478

$$\mathbf{q}_j = (q_{\max(1, j-r)}, \dots, q_{\min(j+r, m)}) \quad (4.10)$$

We define $\delta(x, Y) = \min_{y \in Y} d(x, y)$. The possible minimum cost contributed by the alignment of c_j and some point in Q to the accumulated sum would be $\delta(c_j, \mathbf{q}_j)$. The lower bound LB_{Shen} is defined as: 1479
1480
1481

$$\text{LB}_{\text{Shen}}(Q, C) = d(c_1, q_1) + \sum_{j=2}^{n-1} \delta(c_j, \mathbf{q}_j) + d(c_n, q_m) \quad (4.11)$$

We direct the reader to [54] for the formal proof, while an intuition of the proof is presented here. There are three items on the right-hand side of Equation 4.11. The continuity requirement ensures that each c_i is involved in at least one alignment. The first and the last items are from the boundary condition. The middle item returns the possible minimum distances contributed by each c_j 's, where $2 \leq j \leq n - 1$. It is obvious that LB_{Shen} in Equation 4.11 is tighter when we use the first pair of points and the last pair of points instead of doing the middle summation all from $j = 1$ to n . It is because the distance contributed by the first pair (last pair) must be greater than $\delta(c_1, \mathbf{q}_1)$ ($\delta(c_n, \mathbf{q}_n)$). 1482
1483
1484
1485
1486
1487
1488
1489

It is proven that it is tighter than LB_{Keogh} [54]. It is shown in Figure 4.6 visually. The black bars refer to the additional lower bound distance sum on top of LB_{Keogh} . We will give an intuitive proof here. Both LB_{Keogh} and LB_{Shen} compute the lower bounds by summing the local distance resulting from the alignment of each c_j with some points in Q , which is guaranteed to be not greater than the partial distance contributed by the real alignment, which we only know until we compute the exact distance measure. In LB_{Keogh} , if this c_j falls outside the envelope, this local distance is the vertical distance between c_j and the envelope. If c_j falls inside, this local distance would be 0. For those points outside the envelope, the local distances for c_j of LB_{Keogh} and LB_{Shen} are the same. But LB_{Shen} aims to return the minimum possible partial distance for each c_j , even within the envelope. Hence, $\text{LB}_{\text{Keogh}} \leq \text{LB}_{\text{Shen}}$. 1490
1491
1492
1493
1494
1495
1496
1497
1498
1499
1500

In order to compute Equation 4.11 efficiently, we first sort sequences \mathbf{q}_j and the resulting sorted sequences are denoted as $\tilde{\mathbf{q}}_j$. The sorted sequences allow us to do a binary search when we are calculating $\delta(c_j, \tilde{\mathbf{q}}_j)$ in contrast to $\delta(c_j, \mathbf{q}_j)$. The sorting only needs to be done once because we are testing the same Q with different candidates. 1501
1502
1503
1504

It can be extended to the USDTW case [54, 55]. The possible reach now is not only defined by r , but also by the scaling factor bound l . 1505
1506

$$\mathbf{q}_j = (q_{\max(1, \lceil j/l \rceil - r)}, \dots, q_{\min(\lfloor j/l \rfloor + r, m)}) \quad (4.12)$$

[54] proves the following theorem to allow us to consider the lower bound between each prefix of C and Q without the scaling up of each prefix of C (i.e., $C(1 : k)^L$) and the scaling up of Q (i.e., Q^L).

Theorem 8. *For any $\lceil m/l \rceil \leq k \leq \min(\lfloor lm \rfloor, n)$, $\text{DTW}_r(Q^{\min(\lfloor lm \rfloor, n)}, C(1 : k)^{\min(\lfloor lm \rfloor, n)})$ is always lower bounded by $\sum_{j=1}^k \delta(c_j, \mathbf{q}_j)$.*

Recall that USDTW calculates DTW distances between each rescaled prefix of C to the rescaled Q , and outputs the minimum DTW distance, as in Equation 4.6. The incremental nature of the lower bound frees us to calculate the lower bound of each DTW distance from scratch. This theorem allows us to first calculate the lower bound of the shortest prefix $C(1 : \lceil m/l \rceil)$ of C and Q , and then incrementally calculate the lower bound of the longer prefix with length from $\lceil m/l \rceil + 1$ to $\min(\lfloor lm \rfloor, n)$ by adding on each $\delta(c_j, \mathbf{q}_j)$. To note, it also means that if $\text{LB}_{\text{Shen}}(Q, C(1 : k))$ is larger than a value, namely bsf, $\text{LB}_{\text{Shen}}(Q, C(1 : k'))$, where $k' > k$, would also be larger than bsf. To note, we can tighten LB_{Shen} by using $d(c_1, q_1)$ instead of $\delta(c_1, \mathbf{q}_1)$.

The above analysis can also apply to the case of US distance. We only need to define the corresponding reaches as follows:

$$\mathbf{q}_j = (q_{\max(1, \lceil j/l \rceil)}, \dots, q_{\min(\lfloor j/l \rfloor, m)}) \quad (4.13)$$

4.4 Piecewise Scaling Distance

The motivation stems from the limitations of US and USDTW. They assume that the relationship between Q and C is governed by only a single, global scaling factor. This assumption fails when applied to multi-rate data, where different phases of the time series express at different rates.

Note that existing studies [62, 58] can find all scaling factors, defined by the chosen prefix of C , ranging from $\lceil m/l \rceil$ to $\min(\lfloor lm \rfloor, n)$. However, they can use only one of them in the scaling. Consider the following illustrative example in ASCII text [58], where character repetition represents the duration of spoken phonemes, and space indicates a pause:

- “time series 20 25” and “time series 20 25”. Here, the Hamming distance (the discrete analogue of ED) fails due to misalignment in the underlined locations, but the string edit distance (the discrete analogue of DTW) can resolve it.
- “time sseerriiss 222000222555”. This sequence exhibits three distinct phases with scaling factors of 1, 2, and 3, respectively. The corresponding invariance cannot be

achieved by DTW or US (which is restricted to a single global scalar). US would 1538
enforce a single compromised global scale instead. 1539

In Query-by-Content scenarios, such as query-by-humming or gesture retrieval, the 1540
query is generated by a human. Humans do not maintain a consistent rate for each 1541
phase. For example, humans rush through a familiar sequence but slow down for a 1542
new or complex sequence. It is commonly observed in a piece of music performed by a 1543
beginner. The piece's tempo is not uniform. 1544

We introduce a novel distance measure framework, termed Piecewise Scaling Distance 1545
(PSD). It addresses the local scaling effect within each phase by employing a scaling factor 1546
to each phase, instead of using a single scaling factor for the whole time series. It releases 1547
the basic constraint or assumption made in US and USDTW. PSD employs an existing 1548
distance metric, such as ED or DTW, to quantify the similarity of aligned segment pairs. 1549
While the PSD framework is agnostic to the underlying metric, this study focuses on its 1550
two fundamental instantiations: 1551

- PSED, which employs ED to compute the similarity of aligned segment pairs. 1552
- PSDTW, which employs DTW to compute the similarity of aligned segment pairs. 1553

In the formulation that follows, we utilize PSDTW as the running example. PSDTW 1554
generalizes PSED. The PSED formulation can be trivially derived from it. 1555

4.4.1 Piecewise Scaling & Dynamic Time Warping (PSDTW) 1556

Problem formulation: To simplify the discussion, we focus on the comparison between 1557
 Q and the entire sequence C , rather than a prefix of C . Note that this formulation can 1558
be generalized to prefix matching as in Definition 6 and Definition 7. 1559

Given two sequences Q and C , where Q is not longer than C , $|Q| = m \leq |C| = n$, and 1560
the number of segments or pieces P allowed, our goal is to segmentalize both Q and C 1561
into P contiguous segments automatically in a way that minimize the total sum of DTW 1562
distance of aligned segment pairs with interpolation. 1563

Definition 9 (Piecewise Scaling & Dynamic Time Warping (PSDTW)). With the same 1564
notations defined in Definition 7, 1565

$$\begin{aligned} \text{PSDTW}_r(Q, C, l, L, P) = \\ \min_{\substack{i_1 < i_2 < \dots < i_{P+1} \\ j_1 < j_2 < \dots < j_{P+1}}} \sum_{p=1}^P \text{DTW}_r(Q(i_p + 1 : i_{p+1})^L, \\ C(j_p + 1 : j_{p+1})^L) \end{aligned} \quad (4.14)$$

, where $i_1 = 0$, $i_{P+1} = m$, $j_1 = 0$, $j_{P+1} = n$ and the setting of L will be discussed later. 1566

Algorithm 1 Naive PSDTW

Input: Query series Q , Candidate series C , DTW constraint parameter r (in fraction),

Number of pieces P , Scaling parameter L

Output: Distance Matrix D of size $(m + 1) \times (n + 1) \times (P + 1)$

```
1: Initialize  $D$  with  $\infty$ 
2:  $D[0, 0, 0] \leftarrow 0$ 
3: for  $p \leftarrow 1$  to  $P$  do
4:   for  $i \leftarrow 1$  to  $m$  do
5:     for  $j \leftarrow 1$  to  $n$  do
6:        $D[i, j, p] \leftarrow \min_{i' < i, j' < j} \{D[i', j', p - 1]$ 
          $+ \text{DTW}_r(Q(i' + 1 : i)^L, C(j' + 1 : j)^L)\}$ 
7: return  $D[m, n, P]$ 
```

Algorithm 2 Line 6 in Algorithm 1

```
1: for  $i' \leftarrow 0$  to  $i - 1$  do
2:   for  $j' \leftarrow 0$  to  $j - 1$  do
3:      $dist_{\text{prev}} \leftarrow D[i', j', p - 1]$ 
4:      $dist_{\text{seg}} \leftarrow \text{DTW}_r(Q(i' + 1 : i)^L, C(j' + 1 : j)^L)$ 
5:      $D[i, j, p] \leftarrow \min(D[i, j, p], dist_{\text{prev}} + dist_{\text{seg}})$ 
```

1567 Essentially, L needs to be at least the length of all segments to preserve all the points
1568 by up-sampling.

1569 We refer to Figure 4.3 to clarify Equation 4.14. Given two sequences Q and C , with the
1570 aid of different colors and the dashed lines, we observe that Q consists of three segments
1571 while C consists of four segments, with the first three segments of C similar to those
1572 of Q . They form three segment pairs. The scaling factor used in each segment pair is
1573 determined from the length of the two subsequences involved, i.e., $(i_{p+1} - i_p)/(j_{p+1} - j_p)$.
1574 These three parts have different scaling factors. For example, the first part in C is the
1575 stretched version of that in Q . The second part in C is the compressed version of that in
1576 Q .

1577 Equation 4.14 can be formulated in a recurrence relation as follows. Let $D[i, j, p]$ be
1578 the minimum cost to align the first i points in Q (i.e., $Q(1 : i)$) with the first j points in
1579 C (i.e., $C(1 : j)$) using exactly p segments:

$$D[i, j, p] = \min_{\substack{i' < i \\ j' < j}} \left\{ D[i', j', p - 1] + \text{DTW}_r(Q(i' + 1 : i)^L, C(j' + 1 : j)^L) \right\} \quad (4.15)$$

1580 **Naive PSDTW:**

Algorithm 3 Initialization of PSDTW

- 1: $L_{\text{gmin}}^Q \leftarrow \lceil (m/P)/\sqrt{l} \rceil, \quad L_{\text{gmax}}^Q \leftarrow \lfloor (m/P)\sqrt{l} \rfloor$ ▷ “g” refers to “global”.
 - 2: $L_{\text{gmin}}^C \leftarrow \lceil (n/P)/\sqrt{l} \rceil, \quad L_{\text{gmax}}^C \leftarrow \lfloor (n/P)\sqrt{l} \rfloor$
 - 3: $L = \max(L_{\text{gmax}}^Q, L_{\text{gmin}}^C)$
 - 4: Initialize D of size $(m+1) \times (n+1) \times (P+1)$ with ∞
 - 5: $D[0, 0, 0] \leftarrow 0$
-

Our goal is $D[m, n, P]$. Equation 4.15 can be solved exactly by dynamic programming 1581 (DP). The base case is $D[0, 0, 0] = 0$. It refers to the zero cost to align the first 0 point 1582 (i.e., the empty prefix) of Q with that of C . Other cells in D are first initialized with ∞ . 1583 They are calculated using a bottom-up approach via Equation 4.15. A straightforward 1584 implementation in DP is shown in Algorithm 1. Line 6 is achieved by looping all the 1585 previous indices of the current i and j as in Algorithm 2. 1586

We explain the lines in Algorithm 2. Line 3 retrieves the accumulated distance cost 1587 from the beginning up to the endpoints (i', j') , and saves it as $dist_{\text{prev}}$. Line 4 considers 1588 the current aligned segment pair, which consists of $Q(i'+1 : i)$ and $C(j'+1, j)$, and they 1589 are interpolated to the length L . The DTW distance of this pair is calculated and saved 1590 as $dist_{\text{seg}}$. 1591

We now analyze the time complexity of Algorithm 1. There are Pmn entries in D . 1592 The \min operator in line 6 takes $\mathcal{O}(mn)$. Hence, the time complexity of Algorithm 1 1593 is $\mathcal{O}(Pm^2n^2) = \mathcal{O}(Pn^4)$, multiplied by the running time of the DTW. It is slow, which 1594 prevents us from using it in practice. To note, we use r in a fraction instead of a fixed 1595 integer here. This allows the deviation tolerance to scale adaptively with pieces of varying 1596 lengths. 1597

4.4.2 Speedup Techniques

1598

Length constraints of the segment: A way to reduce complexity and to prevent 1599 pathological segment pairs is to limit the possible segment lengths that are considered by 1600 constraining the minimum and maximum lengths of segments. It is similar to constrained 1601 DTW, in which we limit the search space of the warping path as in Figure 4.5. The 1602 version of PSDTW that considers the segment constraint is termed constrained PSDTW 1603 (cPSDTW). It is shown in Algorithm 4. The uncolored part shows the main logic, while 1604 the colored part shows the speedup techniques, which will be explained later. 1605

We initialize in Algorithm 3. For a given number of segments P , the expected length 1606 of each segment in Q and C would be m/P and n/P , respectively. For Q , we set the 1607 minimum possible segment length L_{gmin}^Q to be $\lceil (m/P)/\sqrt{l} \rceil$ and the maximum possible 1608 length L_{gmax}^Q to be $\lfloor (m/P)\sqrt{l} \rfloor$ in line 1 such that the scaling ratio of any two segments 1609 in Q would be bounded by l . It allows some deviation in the length of the segments from 1610 their expected length. Similarly, we compute the segment constraints for C in line 2. We 1611

Algorithm 4 Constrained PSDTW (cPSDTW) with early abandoning and lower bounding

Input: Query series Q , Candidate series C , DTW constraint parameter r (in fraction), Number of pieces P , best_so_far bsf

Output: The final distance $D[m, n, P]$ if $D[m, n, P] \leq \text{bsf}$, otherwise ∞

- 1: Execute Algorithm 3 for initialization
- 2: **for** $p \leftarrow 1$ **to** P **do**
- 3: **for** $i \leftarrow (p \cdot L_{\text{gmin}}^Q)$ **to** $\min(p \cdot L_{\text{gmax}}^Q, m)$ **do** ▷ The iterations can be parallelized.
- 4: **for** $L^Q \leftarrow L_{\text{gmin}}^Q$ **to** L_{gmax}^Q **do**
- 5: $i' \leftarrow i - L^Q$ ▷ i' : End point of previous segment on Q .
- 6: $Q' \leftarrow \text{rev}(Q(i' + 1 : i))$ ▷ $\text{rev}(T)$: Reverse the input series T .
- 7: $L_{\text{min}}^C \leftarrow \max(L_{\text{gmin}}^C, \lceil L^Q/l \rceil)$
- 8: $L_{\text{max}}^C \leftarrow \min(\lfloor L^Q/l \rfloor, L_{\text{gmax}}^C)$
- 9: $r' \leftarrow r \times \max(L^Q, L_{\text{max}}^C)$ ▷ Compute the integer value of r .
- 10: **for** $k \leftarrow 1$ **to** L_{max}^C **do**
- 11: $\mathbf{q}_k \leftarrow (q'_{\max(1, \lceil k/l \rceil - r')}, \dots, q'_{\min(\lfloor k/l \rfloor + r', L^Q)})$ ▷ Construct indexed collection \mathbb{Q} .
- 12: $\tilde{\mathbf{q}}_k \leftarrow \text{sort}(\mathbf{q}_k)$
- 13: **for** $j \leftarrow (p \cdot L_{\text{gmin}}^C)$ **to** $\min(p \cdot L_{\text{gmax}}^C, n)$ **do**
- 14: **for** $L^C \leftarrow L_{\text{min}}^C$ **to** L_{max}^C **do**
- 15: $j' \leftarrow j - L^C$
- 16: $C' \leftarrow \text{rev}(C(j' + 1 : j))$
- 17: $dist_{\text{prev}} \leftarrow D[i', j', p - 1]$
- 18: **if** $dist_{\text{prev}} = \infty$ **then**
- 19: **continue**
- 20: **if** $dist_{\text{prev}} > \text{bsf}$ **then**
- 21: **continue**
- 22: **if** $dist_{\text{prev}} > D[i, j, p]$ **then** ▷ $D[i, j, p]$ stores the best so far.
- 23: **continue**
- 24: **if** $L^C = L_{\text{min}}^C$ **then** ▷ Compute the lower bound from sketch.
- 25: $lb = (c'_1 - q'_1)^2$ ▷ Partial distance contributed by the first alignment.
- 26: **for** $k \leftarrow 2$ **to** L^C **do**
- 27: $lb = lb + \delta(c'_k, \tilde{\mathbf{q}}_k)$
- 28: **else**
- 29: $lb = lb + \delta(c'_{L^C}, \tilde{\mathbf{q}}_{L^C})$ ▷ Compute the lower bound incrementally.
- 30: $lb_{\text{check}} = lb - \delta(c'_{L^C}, \tilde{\mathbf{q}}_{L^C}) + (c'_{-1} - q'_{-1})^2$ ▷ Tighten the lower bound by using the last alignment.
- 31: **if** $dist_{\text{prev}} + lb_{\text{check}} > D[i, j, p]$ **then**
- 32: **continue**
- 33: $dist_{\text{seg}} \leftarrow \text{DTW}_r(Q'^L, C'^L)$
- 34: **if** $dist_{\text{prev}} + dist_{\text{seg}} < D[i, j, p]$ **then**
- 35: $D[i, j, p] \leftarrow dist_{\text{prev}} + dist_{\text{seg}}$ ▷ Also save pointer (i', j') for the cut.
- 36: **return** $D[m, n, P]$

1612 set the maximum segment length be the alignment factor L in line 3. We set the base
1613 case in line 5.

1614 We fill the table D in Algorithm 4. In line 3, given p pieces in Q , the ending index
1615 of the last piece (i.e., the p^{th} piece) will range from $(p \cdot L_{\text{gmin}}^Q)$, given all the p pieces are
1616 in minimum length L_{gmin}^Q , to $\min(p \cdot L_{\text{gmax}}^Q, m)$, given all the p pieces are in maximum
1617 length L_{gmax}^Q .

1618 In line 4, we enumerate for all the allowed lengths L^Q . For the segment with length
1619 L^Q in Q , the length L^C of the corresponding aligned segment in C will have a range from

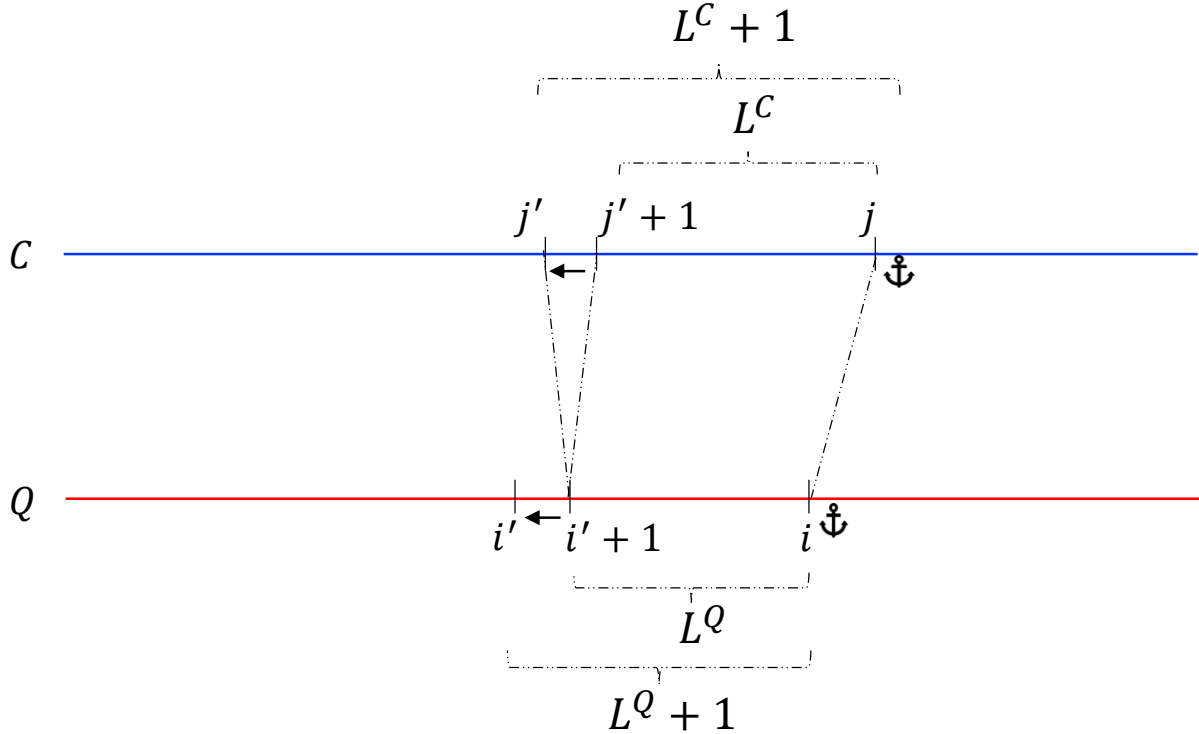


Figure 4.7: Relationship of L_Q and L_C .

L_{\min}^C to L_{\max}^C , as defined in lines 7–8, such that the ratio of L^Q and L^C would be bounded by l . Because L^Q and L^C increase in line 4 and line 14, and the i and j are fixed by the outer loop, in line 3 and line 13, respectively, the i' and j' decrease correspondingly. It is visualized in Figure 4.7. A segment in Q with ending index i and starting index $i' + 1$ would be compared to a set of segments in C , all of which have a fixed end at j and a decreasing starting index, starting at $j' + 1$. For example, the starting index of the first segment with being compared is $j' + 1$, which has length L^C , and that of the second segment is j' , which has length $L^C + 1$, as in Figure 4.7.

In line 18, we terminate the current iteration if there are no previously valid segment pairs (i.e., $dist_{\text{prev}} = \infty$).

In line 22, if the accumulated cost $dist_{\text{prev}}$ exceeds the current best so far, we stop the current iteration as the resulting ($dist_{\text{prev}} + dist_{\text{seg}}$) is guaranteed to be greater than the current best so far, which is stored in $D[i, j, p]$.

To be consistent with the result of using the lower bound speedup technique, which will be introduced later, we compute the DTW in the reverse manner in line 33. Due to the nearest neighbor interpolation, $\text{DTW}_r(Q'^L, C'^L)$ may not equal to $\text{DTW}_r(\text{rev}(Q')^L, \text{rev}(C')^L)$.

In line 35, we also save the pairs (i', j') that serve as cutting points between segments to obtain the segmentation result.

Parallel computing: We observe that the recurrence relation for the state $D[i, j, p]$ at stage p depends exclusively on the states computed at stage $p - 1$, as shown in Equa-

1640 tion 4.15. There are no stage dependencies over indices i and j . It allows us to parallelize
 1641 the loops over indices i and j on lines 3 and 13. In the following experimental section, we
 1642 distribute the i-loop iterations (i.e., line 3 in Algorithm 4, which is colored in blue) across
 1643 available threads only because there are already sufficient iterations from the i-loop to
 1644 fill the available threads. There are $\left(\min(p \cdot L_{\text{gmax}}^Q, m) - (p \cdot L_{\text{gmin}}^Q) + 1\right)$ iterations from
 1645 the i-loop. The parallel execution of the i -loop is implemented by `prange` in Numba in
 1646 Python.

1647 **Early Abandoning in nearest neighbor search:** To accelerate the nearest neighbor
 1648 search (or top- k search) for a query Q on a candidate set, we employ an early abandoning
 1649 strategy. It prunes the search branch within the PSD computation of a specific candidate
 1650 C as soon as the result corresponding to this search branch is determined to be sub-
 1651 optimal. We maintain a variable, bsf (best-so-far), which represents the minimum final
 1652 distance among the candidates processed with Q so far. bsf serves as an upper-bound
 1653 threshold. During the evaluation of a new candidate C , we monitor the accumulated
 1654 partial distance, $\text{dist}_{\text{prev}}$. If $\text{dist}_{\text{prev}}$ exceeds bsf , the corresponding final distance is guar-
 1655 anteed to exceed bsf . In such cases, the current search branch is immediately terminated.
 1656 The implementation of this pruning mechanism is detailed in lines 20–21 in Algorithm 4,
 1657 which are colored in orange. In the case of top- k search, we must maintain the top- k
 1658 final distances and use the k -th distance as the threshold.

1659 Lower bound:

1660 When we use DTW as a routine in PSD, the computation of the DTW of the interpo-
 1661 lated segment can be sped up by computing LB_{Shen} for the lower bound. From Figure 4.7,
 1662 we observe that a segment of Q , with length L^Q , is compared to a set of growing seg-
 1663 ments of C , with a fixed end at j . The length of these segments is from L_{min}^C to L_{max}^C ,
 1664 as indicated in line 14 in Algorithm 4. They share the same suffix with length L_{min}^C . It
 1665 encourages us to view both Q and C reversely. The reversed segments are denoted as Q'
 1666 and C' , as in lines 6 and 16 in Algorithm 4. In this reversed view, they share the same
 1667 prefix with length L_{min}^C . Hence, we construct an indexed collection $\tilde{\mathbb{Q}}$ for Q' with the
 1668 maximum length of the segments being compared in C , which is L_{max}^C , as in lines 10–12.

1669 In lines 24–27, we first compute the lower bound between Q' and the shortest segment
 1670 of C . We add the minimum possible contribution of each c' to the distance contributed
 1671 by the first alignment, which is $lb = (c'_1 - q'_1)$. For the lower bound of the subsequent
 1672 segments, we compute them incrementally in line 29. Because the last point of segment
 1673 C' must map to the last point of Q' , we further tighten the lower bound by using the last
 1674 alignment in line 30 instead.

1675 Furthermore, we can reduce the computational overhead of constructing the sorted
 1676 reaches $\tilde{\mathbb{q}}_k$ (lines 9–12). As illustrated in Figure 4.7, the segment of Q involved in the
 1677 comparison grows incrementally. Since the reversed versions of these segments share a
 1678 common prefix, the sorted reaches $\tilde{\mathbb{q}}_k$ computed for a segment Q' of length L^Q can be

Algorithm 5 Replace lines 3 to 9 in Algorithm 5 to reuse the computed sorted reaches \tilde{q}_k .

```

1:  $r'_{\text{cache}} \leftarrow -1$ 
2: for  $i \leftarrow (p \cdot L_{\text{gmin}}^Q)$  to  $\min(p \cdot L_{\text{gmax}}^Q, m)$  do
3:   for  $L^Q \leftarrow L_{\text{gmin}}^Q$  to  $L_{\text{gmax}}^Q$  do
4:      $i' \leftarrow i - L^Q$ 
5:      $Q' \leftarrow \text{rev}(Q(i' + 1 : i))$ 
6:      $L_{\text{min}}^C \leftarrow \max(L_{\text{gmin}}^C, \lceil L^Q/l \rceil)$ 
7:      $L_{\text{max}}^C \leftarrow \min(\lfloor L^Q/l \rfloor, L_{\text{gmax}}^C)$ 
8:      $r' \leftarrow r \times \max(L^Q, L_{\text{max}}^C)$ 
9:     if  $r'_{\text{cache}} = r'$  then
10:      for  $k \leftarrow 1$  to  $L_{\text{max}}^C$  do
11:        if  $k \leq |Q'|$  then
12:           $e_{\text{prev}} \leftarrow \min(\lfloor kl \rfloor + r', L^Q - 1)$ 
13:           $e_{\text{new}} \leftarrow \min(\lfloor kl \rfloor + r', L^Q)$ 
14:          if  $e_{\text{new}} > e_{\text{prev}}$  then
15:             $\tilde{q}_k \leftarrow \tilde{q}_k \cup q'_{e_{\text{new}}}$ 
16:        else
17:           $q_k \leftarrow (q'_{\max(1, \lceil k/l \rceil - r')}, \dots,$ 
18:           $q'_{\min(\lfloor kl \rfloor + r', L^Q)})$  ▷  $L^Q$  equals to  $|Q'|$ .
19:        else
20:          for  $k \leftarrow 1$  to  $L_{\text{max}}^C$  do
21:             $q_k \leftarrow (q'_{\max(1, \lceil k/l \rceil - r')}, \dots,$ 
22:             $q'_{\min(\lfloor kl \rfloor + r', L^Q)})$ 
23:             $\tilde{q}_k \leftarrow \text{sort}(\tilde{q}_k)$ 
 $r_{\text{cache}} \leftarrow r'$ 

```

reused to compute those for the subsequent segments. This optimization is detailed in 1679
Algorithm 5, with the new components highlighted in blue. It is important to note that 1680
because r' is a function of L^Q , and the construction of \tilde{q}_k depends on r , reuse is limited 1681
to cases where r' remains constant. We construct reaches \tilde{q}_k from the sketch in lines 1682
20–22 and keep track of the r' used for construction in line 23. If r' remains constant, 1683
we can use previously computed reaches \tilde{q}_k to compute the new set of reaches \tilde{q}_k . Since 1684
the ending index of reaches depends on $\min(\lfloor kl \rfloor + r', L^Q)$, we need to check whether we 1685
have a new ending index when L^Q increases. If the ending index has been changed, we 1686
need to add the new data points $q'_{e_{\text{new}}}$ to the sorted sequence \tilde{q}_k , as in line 15. 1687

L_{max}^C depends of L^Q . If L_{max}^C increase because L^Q increase, we construct the new reach 1688
 \tilde{q}_k and sort it in lines 16–18. 1689

1690 **4.4.3 Guided Distance**

1691 For faster computation, one would want to use a distance measure with linear complexity,
1692 such as ED, as the base measure for PSD. While PSED is effective for identifying phase-
1693 scaling changes, certain applications require capturing complex properties within those
1694 segments that ED cannot handle. There are two ways to address it. One approach is
1695 to use an alternative distance measure that captures these complex properties as the
1696 base distance for computing the PSD, such as DTW. But PSDTW is slower than PSED.
1697 The other approach is to use the segmentation result returned by PSED. To address
1698 this, we propose a two-stage framework in which PSED-derived segmentation guides the
1699 application of advanced distance metrics M . Let $\mathcal{P}^* = \{(i_1, j_1), (i_2, j_2), \dots, (i_{P+1}, j_{P+1})\}$
1700 be the set of optimal cut points on Q and C obtained by minimizing the PSED. We
1701 utilize \mathcal{P}^* to partition both series into P aligned pairs of segments. The final distance,
1702 denoted as M^{PSED} , is calculated by summing the distances of these pairs using a target
1703 metric M :

$$M^{\text{PSED}}(Q, C) = \sum_{p=1}^P M(Q_p^L, C_p^L) \quad (4.16)$$

1704 , where $Q_p = Q(i_p + 1 : i_{p+1})$ and $C_p = C(j_p + 1 : j_{p+1})$.

1705 **4.5 Experiments**

1706 We evaluate the performance of our proposed distance measure framework, PSD, via its
1707 two instantiations: PSED and PSDTW. Specifically, we focus on a query retrieval task
1708 in which the query exhibits piecewise-scaled distortion, that is, distinct phases of the
1709 query exhibit different expression rates relative to the target in the candidate dataset.
1710 Our objective is to verify whether PSD achieves invariance to these multiple scaling
1711 distortions, thereby allowing it to correctly retrieve the most similar candidate. We detail
1712 the experimental setup in Section 4.5.1 and present the results in Section 4.5.2. The code
1713 and data are available at <https://github.com/colemanyu/k-scaling-factor-dtw>.

1714 **4.5.1 Experimental Setup**

1715 We utilize the GunPoint dataset, originally released in 2003 [68], as the running example.
1716 Widely regarded as the “iris” dataset of the time series community [69], it has appeared
1717 in over one thousand publications. Beyond its ubiquity, the dataset addresses a critical
1718 distinction: misinterpreting the act of aiming a gun as merely pointing a finger could
1719 have life-threatening consequences.

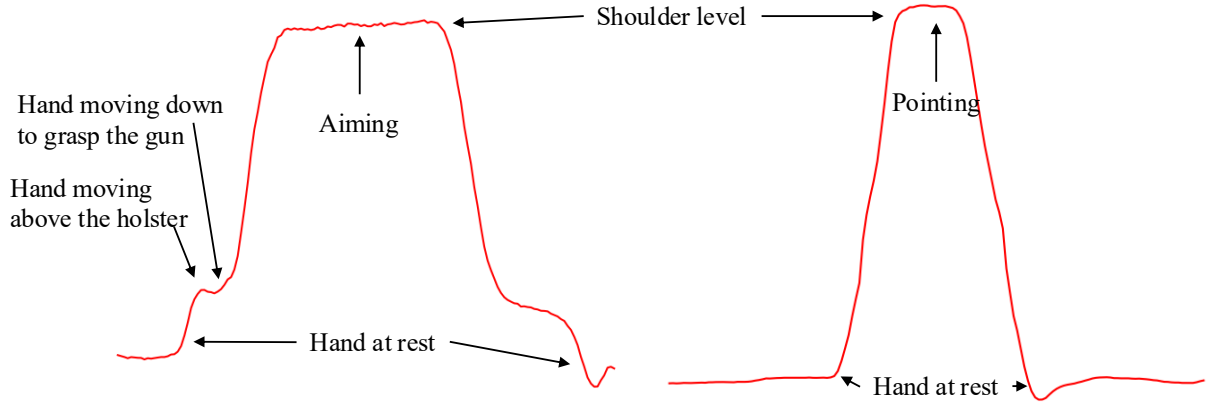


Figure 4.8: Visualization of the GunPoint dataset. Left (Right): A time series of the “Gun” (“Point”) scenario. Critical periods, such as “Aiming”, are annotated.

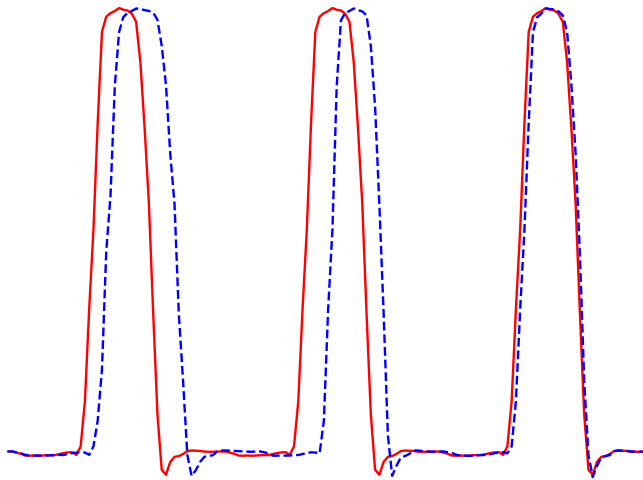


Figure 4.9: The red solid time series shows an instant in the target set. The blue dashed time series shows an instant in the query set.

The dataset contains two classes: “Gun” and Point”. Actors aim at an eye-level target 1720 using either a replica gun or their index finger, as illustrated in Figure 4.8. The resulting 1721 time series represent the X-axis centroid of the actor’s right hand. Each action lasts 1722 for 5 seconds, with the pointing/aiming phase occurring for approximately one second. 1723 Recorded at 30 fps, each sample consists of 150 data points. The dataset comprises 50 1724 training and 150 test series, all of length 150. 1725

A key limitation of the original dataset is the assumption that every action lasts 1726 exactly 5 seconds. In reality, actors perform actions at varying speeds. If an actor is 1727 asked to perform the action three times continuously in a row, we are likely to observe a 1728 time series containing three phases, each with a unique rate. The first phase should take 1729 longer than subsequent phases because it is the first time the action is performed. This 1730 phenomenon is depicted in Figure 4.9, where the red curve represents an ideal case that 1731 consists of three identical phases (i.e., identical rate), while the blue curve represents a 1732

1733 realistic scenario with varying rates. The first action is slower than the second action.
1734 Consequently, retrieving such patterns requires assigning different scaling factors to each
1735 phase to accommodate the phase-specific rates.

1736 We now describe the procedure for generating the target and query sets for the re-
1737 trieval task. To construct the target set, we concatenate P repetitions of each time series
1738 instance from the source dataset. To ensure a fair comparison, we constrain the resulting
1739 time series to match the original length n . This is achieved by rescaling each phase to a
1740 length of n/P prior to concatenation. Note that we must handle remainders to ensure
1741 that the final time series length is exactly n . An example of such a target (where $P = 3$)
1742 is depicted by the red solid line in Figure 4.9.

1743 To construct the query set, we first determine the specific lengths for the P segments.
1744 Starting with an expected mean length of n/P , we define the minimum segment length
1745 as $L_{\min} = (n/P)\sqrt{l}$ and the maximum as $L_{\max} = (n/P)\sqrt{l}$. This formulation ensures
1746 that the ratio of the lengths of any two segments is bounded by l . We then generate P
1747 random integers within $[L_{\min}, L_{\max}]$ subject to the constraint that their sum is exactly n .
1748 Finally, we construct the query by rescaling P copies of the source time series to these
1749 generated random lengths and concatenating them. The resulting time series maintains
1750 the original length n . An example of such a query (where $P = 3$) is depicted by the blue
1751 dashed line in Figure 4.9.

1752 Both the query and target sets are derived from the same source dataset. Conse-
1753 quently, the ground truth target for a given query is defined as the instance in the target
1754 set that is generated from the same underlying source time series.

Table 4.1: Details of the ten datasets for the experiments

Name	Type	Train/Test?	Size	Class	Length
SonyAIBORobotSurface1	Sensor	Test	601	2	70
ECG200	ECG	Train	100	2	96
MedicalImages	Image	Train	381	10	99
CBF	Simulated	Train	30	3	128
SwedishLeaf	HAR	Train	500	15	128
Plane	Sensor	Train	105	7	144
PowerCons	Device	Train	180	2	144
GunPoint	HAR	Train	50	2	150
Adiac	Image	Train	390	37	176
Epilepsy	HAR	Train	137	4	207

1755 Table 4.1 details the additional datasets used in this study. The column labeled
1756 “Train/Test?” specifies which split was employed as the source dataset.

1757 In our experiments, we set the warping window parameter $r = 0.1$, as suggested in
1758 the literature. The algorithms were implemented in Python. We utilized the `aeon` [70]

library to obtain the baseline distance measures. All experiments were conducted on a 1759
workstation equipped with an Intel Xeon Gold 6326 CPU and 256GB of RAM. 1760

4.5.2 Experimental Results

1761

We employ Top- k Accuracy (often referred to as Precision@ k [71]) as the primary evaluation metric. For a single query Q , this metric indicates whether the correct match is successfully retrieved within the top k candidates: 1762
1763
1764

$$P@k(Q) = \begin{cases} 1 & \text{if the ground truth is in the top-}k \text{ results} \\ 0 & \text{otherwise} \end{cases} \quad (4.17)$$

To determine the top- k results, we compute the distance between Q and every time series in the target set, generating a distance profile of length equal to the dataset size. 1765
1766
1767
1768
1769 The top- k results correspond to the k instances with the smallest distances in this profile. Finally, we evaluate the overall performance by computing the mean Top- k Accuracy across the entire query set \mathcal{D} : 1769

$$\overline{P@k} = \frac{\sum_{Q \in \mathcal{D}} P@k(Q)}{|\mathcal{D}|} \quad (4.18)$$

We choose $k \in \{1, 3\}$. $k = 1$ refers to the exact retrieval. $k = 3$ give some tolerance for the retrieval. 1770
1771

Table 4.2: The accuracy comparison for eight distance measures of the GunPoint dataset

P	l	ED		DTW [2]		ADTW [10]		DDTW [4]		shapeDTW [6]		WDDTW [5]		WDTW [5]		PSED		PSDTW	
		$P@1$	$P@3$	$P@1$	$P@3$	$P@1$	$P@3$	$P@1$	$P@3$	$P@1$	$P@3$	$P@1$	$P@3$	$P@1$	$P@3$	$P@1$	$P@3$	$P@1$	$P@3$
2	1.25	0.30	0.56	0.82	1.00	0.54	0.84	0.84	0.92	<u>0.96</u>	1.00	0.88	0.96	0.82	0.98	0.98	1.00	0.86	1.00
	1.50	0.14	0.36	0.88	1.00	0.38	0.64	0.78	0.94	1.00	1.00	0.80	0.92	0.88	0.96	1.00	1.00	<u>0.96</u>	1.00
	1.75	0.16	0.34	0.82	1.00	0.38	0.66	0.64	0.80	0.90	1.00	0.66	0.80	0.82	0.96	1.00	1.00	<u>0.94</u>	1.00
	2.00	0.12	0.24	0.84	0.98	0.34	0.66	0.72	0.88	<u>0.96</u>	1.00	0.68	0.86	0.82	0.98	1.00	1.00	<u>0.96</u>	1.00
	1.25	0.30	0.50	0.84	0.92	0.70	0.88	0.80	0.92	0.96	0.98	0.84	0.94	0.86	0.98	<u>0.94</u>	1.00	0.88	0.96
3	1.50	0.10	0.28	0.84	0.96	0.60	0.78	0.66	0.86	<u>0.90</u>	1.00	0.72	0.86	0.84	0.98	0.96	1.00	0.86	0.96
	1.75	0.10	0.28	<u>0.88</u>	1.00	0.42	0.78	0.72	0.88	0.76	0.94	0.74	0.88	<u>0.88</u>	1.00	1.00	1.00	<u>0.88</u>	0.98
	2.00	0.02	0.12	<u>0.86</u>	0.94	0.38	0.52	0.60	0.78	0.70	0.94	0.60	0.80	0.82	0.92	0.98	1.00	<u>0.86</u>	0.98
	1.25	0.34	0.50	0.70	0.86	0.68	0.88	0.60	0.78	0.70	0.90	0.64	0.80	0.70	0.86	0.86	0.94	<u>0.72</u>	0.88
4	1.50	0.22	0.38	0.64	0.80	0.60	0.92	0.52	0.64	0.68	0.90	0.52	0.66	0.64	0.82	0.86	0.98	<u>0.72</u>	0.82
	1.75	0.16	0.30	0.72	0.92	0.56	0.80	0.60	0.78	0.56	0.80	0.56	0.80	0.70	0.88	0.92	1.00	<u>0.80</u>	0.94
	2.00	0.06	0.12	0.58	0.78	0.50	0.72	0.46	0.64	0.50	0.82	0.50	0.64	0.56	0.82	0.88	0.98	<u>0.64</u>	0.88

Results of GunPoint dataset: We utilize the GunPoint dataset to evaluate how the parameters P and l affect the ability of PSD to achieve invariance under piecewise scaling. The results are presented in Table 4.2, where the best performance of $\overline{P@1}$ is highlighted in bold, and the second-best is underlined. We benchmark our method against several state-of-the-art distance measures, including ADTW [10], DDTW [4], shapeDTW [6], WDDTW [5], and WDTW [5]. PSED achieves the highest accuracy, followed closely by PSDTW. We attribute PSED’s superior performance over PSDTW to the specific nature 1772
1773
1774
1775
1776
1777
1778

1779 of the distortions in the query set, that is, the “pure” piecewise scaling distortions. Since
 1780 the query set exhibits only piecewise scaling distortions, the corresponding segments of the
 1781 query and target time series differ solely in length (scale). Consequently, the additional
 1782 flexibility provided by DTW in PSDTW is unnecessary and may inadvertently increase
 1783 the similarity of incorrect matches, thereby reducing discriminative power relative to the
 1784 stricter PSED measure. However, PSDTW remains theoretically essential for handling
 1785 local distortions within the phase. PSDTW applies DTW within the scaled segment,
 1786 enabling robust alignment across local nonlinearities.

Table 4.3: The accuracy comparison for six PSED-guided distance measures of the Gun-Point dataset

P	l	DTW ^{PSED}		ADTW ^{PSED}		DDTW ^{PSED}		shapeDTW ^{PSED}		WDDTW ^{PSED}		WDTW ^{PSED}	
		$\overline{P@1}$	$\overline{P@3}$	$\overline{P@1}$	$\overline{P@3}$	$\overline{P@1}$	$\overline{P@3}$	$\overline{P@1}$	$\overline{P@3}$	$\overline{P@1}$	$\overline{P@3}$	$\overline{P@1}$	$\overline{P@3}$
2	1.25	0.86	1.00	0.98	1.00	0.72	0.92	0.98	1.00	0.74	0.96	0.86	1.00
	1.50	0.88	1.00	1.00	1.00	0.60	0.90	0.98	1.00	0.64	0.90	0.92	1.00
	1.75	0.94	1.00	1.00	1.00	0.84	0.94	1.00	1.00	0.86	0.96	0.94	1.00
	2.00	0.98	1.00	1.00	1.00	0.60	0.78	0.98	1.00	0.66	0.80	0.98	1.00
3	1.25	0.82	0.96	0.94	1.00	0.74	0.90	0.92	0.98	0.76	0.90	0.82	0.96
	1.50	0.86	1.00	0.96	1.00	0.72	0.90	0.94	1.00	0.80	0.90	0.88	1.00
	1.75	0.88	1.00	1.00	1.00	0.68	0.90	1.00	1.00	0.70	0.94	0.90	1.00
	2.00	0.86	0.96	0.98	1.00	0.54	0.86	0.96	1.00	0.62	0.86	0.88	0.96
4	1.25	0.74	0.88	0.86	0.94	0.78	0.80	0.80	0.92	0.78	0.82	0.74	0.88
	1.50	0.72	0.84	0.86	0.98	0.68	0.84	0.84	0.96	0.66	0.84	0.72	0.86
	1.75	0.74	0.96	0.92	1.00	0.54	0.90	0.90	1.00	0.56	0.88	0.74	0.96
	2.00	0.66	0.90	0.88	0.98	0.58	0.82	0.88	0.98	0.62	0.80	0.66	0.90

1787 We further investigate whether the segmentation results returned by PSED can serve
 1788 as a guide to enhance other distance measures. As shown in Table 4.3, this approach
 1789 generally improves accuracy. The exceptions are highlighted in bold, indicating cases
 1790 where the segmentation led to worse performance. Notably, in most cases, only DDTW
 1791 and WDDTW failed to benefit from PSED-guided segmentation. We argue that the
 1792 performance degradation of DDTW and WDDTW stems from their derivative-based
 1793 nature. They rely on matching slope or shape features. Consequently, they are highly
 1794 sensitive to segmentation boundaries. A non-perfect cut that falls within a shape feature
 1795 segmentizes it, and these features are then destroyed. When the algorithm subsequently
 1796 attempts to map these features, it fails to find correct correspondences, resulting in high
 1797 distances.

1798 Figure 4.10 illustrates the runtime performance across varying parameters P and l .
 1799 We evaluate two variants of PSD, PSED and PSDTW, each implemented with three
 1800 levels of

- 1801 1. `vanilla` (i.e., Basic implementation)
 1802 2. `parallel_bsf` (i.e., With parallelization with Best-So-Far early abandoning)

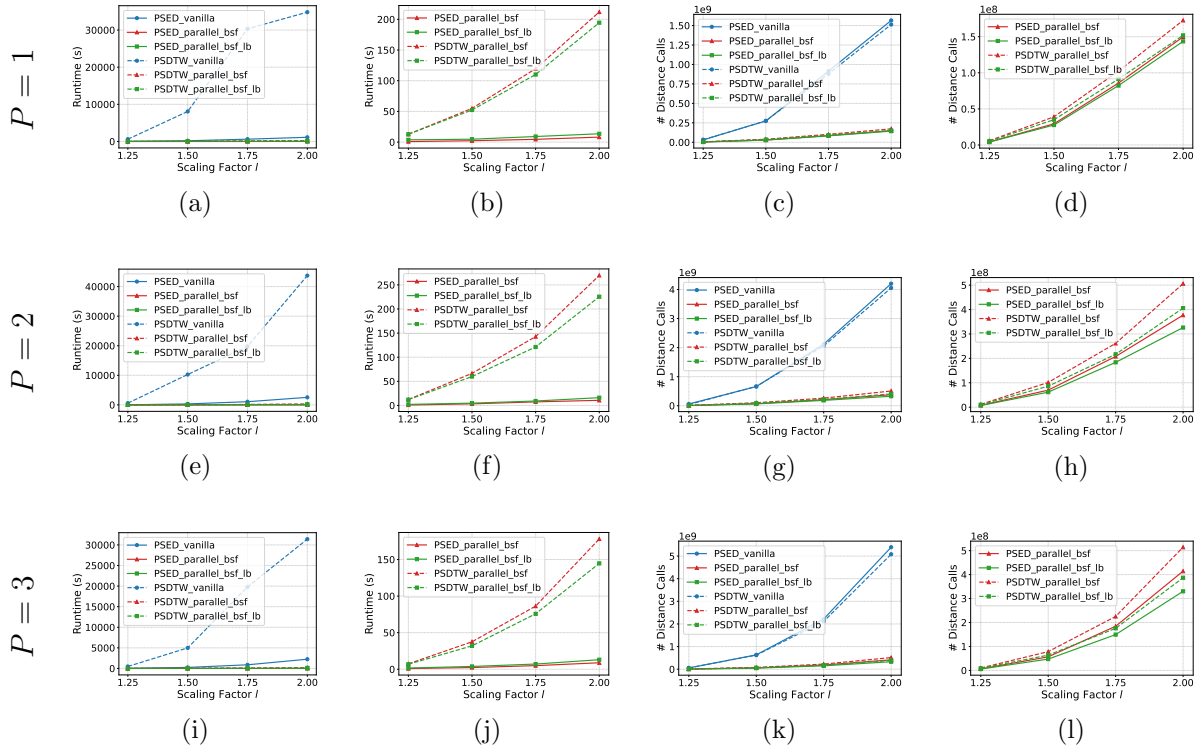


Figure 4.10: Runtime and number of distance calls comparison of GunPoint dataset. (a)-(d) $P = 1$, (e)-(h) $P = 2$, (i)-(l) $P = 3$.

3. parallel_bsf_lb (i.e., Incorporating lower bound pruning)

1803

This yields a total of six methods. The figure is organized into four columns plotted against the scaling factor l . The rows refer to the number of pieces P . The first and third columns display the running time and the number of distance calculations, respectively, for all six methods. To better visualize the performance differences among the efficient implementations, the second and fourth columns omit the `vanilla` baselines and focus exclusively on the four optimized variants. 1804
1805
1806
1807
1808
1809

The results indicate that `vanilla_PSDTW` is orders of magnitude slower than the other approaches, whereas the optimized methods operate within a similar performance range. 1810
1811
As anticipated, the computation time for all methods increases with the scaling factor 1812
 l . The fourth column confirms that the lower bounding strategy effectively reduces the 1813
number of distance calculations (pruning power). However, the second column reveals 1814
a critical trade-off in actual runtime. While the lower bound successfully accelerates 1815
PSDTW, it actually slows down PSED. This suggests that for the computationally lighter 1816
ED, the overhead of calculating the lower bound outweighs the time saved by pruning. 1817
Overall, the results demonstrate that PSED is significantly faster than PSDTW. 1818

Results of the ten datasets:

For the remaining nine datasets, we fix the parameters at $P = 3$ and $l = 1.5$. We have the following findings from the previous experiment: 1820
1821

Table 4.4: The accuracy comparison for eight distance measures of the ten datasets

Dataset	ED		DTW		ADTW		DDTW		shapeDTW		WDDTW		WDTW		PSED	
	P@1	P@3	P@1	P@3	P@1	P@3	P@1	P@3	P@1	P@3	P@1	P@3	P@1	P@3	P@1	P@3
SonyAIBORobotSurface1	0.04	0.08	0.51	0.63	<u>0.60</u>	0.74	0.45	0.57	0.20	0.29	0.45	0.58	0.51	0.64	0.67	0.77
ECG200	0.12	0.20	0.70	0.81	<u>0.78</u>	0.83	0.60	0.74	0.59	0.76	0.59	0.73	0.70	0.80	0.81	0.88
MedicalImages	0.08	0.19	0.63	0.78	0.69	0.85	0.52	0.68	0.57	0.75	0.51	0.68	0.62	0.78	0.76	0.88
CBF	0.53	0.67	0.83	1.00	<u>0.90</u>	1.00	0.73	0.87	0.73	0.90	0.77	0.90	<u>0.90</u>	1.00	1.00	1.00
SwedishLeaf	0.07	0.12	0.82	0.92	<u>0.84</u>	0.93	0.70	0.83	0.78	0.91	0.69	0.83	0.83	0.92	0.97	0.99
Plane	0.09	0.14	0.50	0.74	<u>0.59</u>	0.78	0.38	0.64	0.53	0.79	0.37	0.61	0.49	0.75	0.75	0.93
PowerCons	0.26	0.43	0.77	0.98	0.80	1.00	0.77	0.98	0.77	0.99	0.77	0.99	0.77	0.99	0.80	1.00
GunPoint	0.10	0.28	<u>0.84</u>	0.96	0.60	0.78	0.66	0.86	0.90	1.00	0.72	0.86	<u>0.84</u>	0.98	0.96	1.00
Adiac	0.01	0.02	<u>0.37</u>	0.50	0.12	0.21	0.32	0.42	0.27	0.41	0.31	0.41	0.36	0.50	0.57	0.71
Epilepsy	0.18	0.26	0.74	0.88	<u>0.80</u>	0.91	0.65	0.82	0.38	0.47	0.58	0.79	0.70	0.83	0.83	0.91

Table 4.5: The accuracy comparison for six PSED-guided distance measures of the ten datasets

Dataset	DTW ^{PSED}		ADTW ^{PSED}		DDTW ^{PSED}		shapeDTW ^{PSED}		WDDTW ^{PSED}		WDTW ^{PSED}	
	P@1	P@3	P@1	P@3	P@1	P@3	P@1	P@3	P@1	P@3	P@1	P@3
SonyAIBORobotSurface1	0.53	0.64	0.64	0.76	0.37	0.53	0.65	0.76	0.38	0.53	0.53	0.65
ECG200	0.73	0.84	0.80	0.88	0.54	0.68	0.81	0.88	0.53	0.69	0.73	0.84
MedicalImages	0.66	0.78	0.76	0.88	0.51	0.69	0.74	0.88	0.51	0.70	0.66	0.79
CBF	0.90	1.00	0.93	1.00	0.73	0.93	0.93	0.97	0.70	0.93	0.90	1.00
SwedishLeaf	0.82	0.92	0.97	0.99	0.72	0.87	0.97	0.99	0.73	0.88	0.82	0.92
Plane	0.60	0.80	0.75	0.94	0.50	0.67	0.74	0.90	0.50	0.69	0.59	0.80
GunPoint	0.86	1.00	0.96	1.00	0.72	0.90	0.94	1.00	0.80	0.90	0.88	1.00
PowerCons	0.78	0.99	0.79	1.00	0.79	1.00	0.79	1.00	0.79	1.00	0.78	1.00
Adiac	0.33	0.45	0.57	0.71	0.21	0.34	0.53	0.70	0.20	0.33	0.34	0.45
Epilepsy	0.77	0.88	0.78	0.88	0.66	0.79	0.74	0.89	0.66	0.82	0.80	0.89

1822 1. From Table 4.3, PSED outperformed PSDTW in handling piecewise scaling distortions.

1823 2. From Figure 4.10, the lower bound offered no efficiency gain for PSED.

1825 Hence, we select PSED_parallel_bsfs as the representative method for this evaluation.

1826 The accuracy results are presented in Table 4.4, while the results for the PSED-guided
1827 distance measures are detailed in Table 4.5. Finally, the runtime efficiency for all datasets
1828 is summarized in Table 4.6. It shows a significant speedup, ranging from 10.10X to
1829 191.46X.

1830 4.6 Concluding Remarks

1831 In this paper, we proposed a novel distance measure framework, Piecewise Scaling Dis-
1832 tance (PSD), which relaxes the strict assumption of a single uniform scaling factor across
1833 the entire time series. We presented an exact dynamic programming (DP) algorithm to
1834 solve this problem. To enhance efficiency and prevent pathological segment alignments,
1835 we introduced a constraint version, which limits the search space of segment lengths
1836 based on given scaling factors. To enhance computational efficiency, we integrated two

Table 4.6: The number of distance calls and runtime on PSED_vanilla and PSED_parallel_bsf of the ten datasets

Name	Size	Length	PSED_vanilla	PSED_parallel_bsf	% distance calls pruned	Speed Up
			Time (s)	Time (s)		
SonyAIBORobotSurface1	601	70	697	69	90.40%	10.10X
ECG200	100	96	91	3	91.08%	30.33X
MedicalImages	381	99	2082	40	96.03%	52.05X
CBF	30	128	43	2	75.31%	21.50X
SwedishLeaf	500	128	16601	107	96.24%	155.15X
Plane	105	144	621	6	96.05%	103.50X
PowerCons	180	144	3629	49	82.32%	74.06X
GunPoint	50	150	159	3	89.42%	53.00X
Adiac	390	175	23550	123	96.71%	191.46X
Epilepsy	137	206	13131	336	39.88%	39.08X

optimization techniques for the general PSD framework. In addition, we propose incorporating a lower-bounding strategy to accelerate PSDTW. Our experimental results demonstrate the necessity and effectiveness of PSD when identifying matches between a query Q and a candidate C under piecewise scaling distortions.

We outline several directions for future research. First, we aim to develop a lower bound specifically optimized for PSED that can improve actual runtime. Second, while the current PSDTW algorithm requires the number of segments P to be specified as a hyperparameter, it is preferable for the algorithm to determine this value adaptively. A simple heuristic is to test a range of P values and select the configuration that yields the minimum distance. Finally, we plan to investigate efficiency improvements for PSDTW. Currently, PSDTW computes dynamic time warping on two growing subsequences after scaling. While techniques for Incremental DTW [72] allow for the reuse of the accumulating cost matrix D to avoid redundant calculations, applying this to PSDTW is non-trivial. The interpolation performed before DTW fundamentally alters the sequence structure, preventing the straightforward extension of D (e.g., by appending rows or columns) to reuse the computed D that is possible in standard DTW.

Chapter 5

1853

Leveraging Nearest Neighbors for Time Series Forecasting with Matrix Profile

1854

1855

1856

5.1 Background

1857

Humans have made predictions since ancient times. In ancient societies, accurate predictions were important to the success of subsistence activities such as hunting, planting, and harvesting. There was a need to predict weather dynamics, such as rainfall and temperature. For example, it is crucial to plant during the period with sufficient rainfall and appropriate temperatures. Our ancestors used divination tools such as turtle shells, wooden blocks (moon blocks), or bones to make predictions. Without doubt, the accuracy was not guaranteed. Even in modern societies, prediction is still essential. Predicting traffic-jam patterns only a few hours ahead can save time by enabling the selection of an alternative route [73]. A wealth could be created by forecasting stock market trends. Predicting the future, also known as time series forecasting, is crucial.

1867

With advances in hardware technologies, we collect enormous amounts of data from diverse sources, such as smart sensors and social media platforms, continuously in the form of time series data. A time series is an ordered sequence of measures, represented in real-valued numbers, at discrete equal-interval timestamps [74]. The vast data collections have created the era of “Big Data”, which provides a wealth of datasets for developing and deploying reliable, robust, data-driven forecasting techniques to discover patterns and extract valuable information [75]. Applications can be found in the financial sector, such as predicting business cycles and stock market movements [76, 73, 77, 78] and the medical field, such as the status of critical patients according to their vital signs [79, 80] and the propagation of diseases such as influenza [78, 81] and COVID-19 [79, 82].

1877

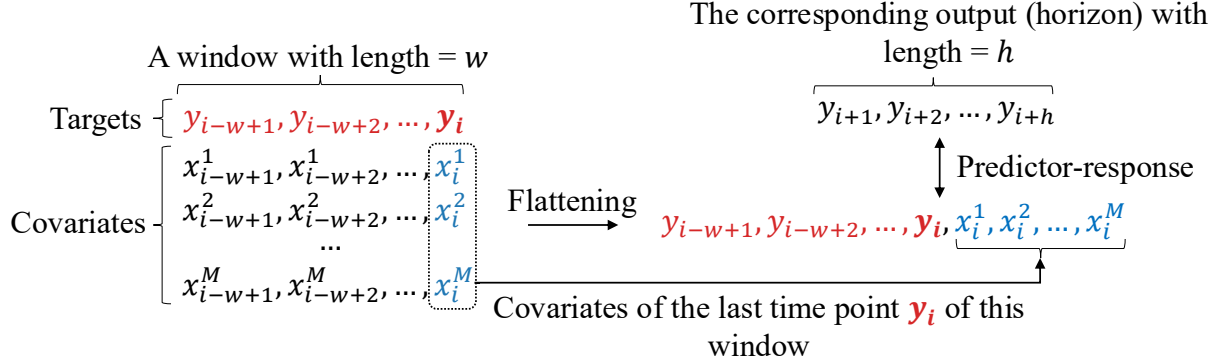


Figure 5.1: Flattening a 2D window of size $(1+M) \times w$ to a 1D vector of length $w+M$. The resulting vector serves as the *predictor* for the regressor. Its expected *response* is the vector of length h . The regressor learns from this predictor-response pair.

1878 A recent study [1] shows that, in time series classification, a non-parametric, instance-
 1879 based method, namely nearest-neighbor classifiers (1-NN) and its generalized form k -NN,
 1880 with appropriate distance measures, such as Dynamic Time Warping (DTW), despite
 1881 their simplicity, perform well and are therefore commonly used as benchmarks. In de-
 1882 tail, when a new instance is to be classified, k -NN finds its k nearest neighbors in the
 1883 training set and returns their majority label among them. k -NN is considered a lazy
 1884 learner because the training steps involve only memorizing all the instances verbatim; no
 1885 higher-level concepts have been learned. In addition, in time series forecasting, a recent
 1886 study demonstrates that a well-known machine learning baseline, Gradient Boosting Re-
 1887 gression Tree (GBRT), such as XGBoost, equipped with an appropriate data engineering
 1888 of the data, can achieve competitive or even superior performance than the deep learning
 1889 method. In detail, they transform the time series forecasting task into a window-based
 1890 regression problem, as shown in Figure 5.1. For each training window of length w with
 1891 the last time point \mathbf{y}_i , and its lagged values $\mathbf{y}_{i-1}, \mathbf{y}_{i-2}, \dots, \mathbf{y}_{i-w+1}$ are concatenated with
 1892 covariates $x_i^1, x_i^2, \dots, x_i^M$ to form a *predictor* for a multi-output GBRT. This transfor-
 1893 mation is called flattening. The corresponding response is the following h points of \mathbf{y}_i . It
 1894 provides a simple, more efficient yet accurate method for time series forecasting.

1895 Moreover, k -NN has also shown to be a promising method for time series forecast-
 1896 ing [83]. The k -NN uses the lagged values of the last time point to form a query Q .
 1897 It identifies the k previous similar subsequences to Q and uses their immediate subse-
 1898 quences to predict the immediate subsequence, which is the forecasting window, of Q .
 1899 The intuition is that history repeats itself. The previous (historical) subsequences that
 1900 are similar to Q can provide a hint about the future of Q . They are similar, and so are
 1901 their immediate subsequences. Figure 5.2 depicts this idea. Observe that the immediate
 1902 subsequence of the right gray box is similar to that of the left gray box. The left gray
 1903 box is the nearest neighbor of the right gray in the “past”.

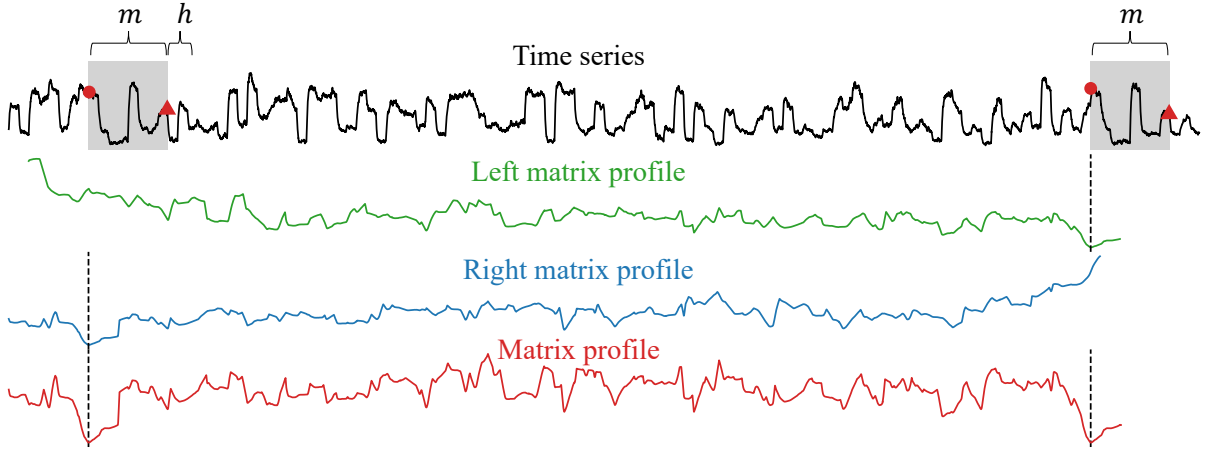


Figure 5.2: The **left** (**right**) matrix profile and the **matrix profile** of a time series. The **matrix profile** shows the distances between each m -subsequence and its nearest neighbor, where m is a user-given value. The **left** (**right**) matrix profile shows the same information but is limited to its left (right) nearest neighbor. For a particular m -subsequence shown by the right gray box, its nearest neighbor is the left gray box, as indicated by the dashed line in the **left matrix profile** and the **matrix profile**. Similarly, the nearest neighbor of the left gray box is the right gray box, as indicated by the dashed line in the **right matrix profile** and the **matrix profile**. The first (last) point in each box is denoted by a red circle (triangle). h denotes the length of the immediate subsequence of the nearest neighbor. Intuitively, this subsequence should be similar to the immediate subsequence (i.e., future) of the right gray box. To note, the **left** (**right**) matrix profile starts (ends) at a later (earlier) index because the corresponding nearest neighbor with length m does not exist.

Algorithm 6 The brute force approach to compute Matrix Profile

```

1: for  $i \leftarrow 1$  to  $n - m + 1$  do
2:   for  $j \leftarrow 1$  to  $n - m + 1$  do
3:     Compute the z-normalized Euclidean distance between  $t_{i,m}$  and  $t_{j,m}$ .

```

Based on these findings, this study proposes a method to improve the performance of existing forecasters by leveraging information from the nearest neighbors of each subsequence in the target variable. For each time point y_i of the target variable Y , a window of length w is constructed with y_i as the last point, then we retrieve the window's historical nearest neighbors and use their information to create new covariates for the window. The information includes the similarities between the window and its nearest neighbors, as well as the immediate subsequences of them. The similarity can be interpreted as a measure of confidence or weight in using the information from the corresponding nearest neighbor. The intuition is that, if the similarity of the window and a neighbor is high, then the future (i.e., immediate subsequence) of the neighbor should also be similar to the future of the window. The fundamental difference between this study and previous approaches [84, 83, 85] is that they directly use the subsequent points for prediction, whereas we use the nearest neighbor information for each subsequence as covariates,

1917 which are used as primitives for other forecasters. We explain this subtle difference by
1918 Figure 5.2. The previous approaches simply use the information of the nearest neighbors
1919 of the last look-back window, which consisted of the last time point and its lagged values
1920 (i.e., the right gray box), for prediction. In contrast, we use the information of the nearest
1921 neighbors of **all** of the windows.

1922 We use the Matrix Profile [86, 87] to annotate the nearest neighbor for each m -
1923 subsequence of a time series T of length n . The distance is the z-normalized Euclidean
1924 distance. It may seem computationally expensive to perform this annotation at first
1925 glance. Algorithm 6 shows the brute force approach to compute the matrix profile.
1926 The two for-loops and the computation of z-normalized Euclidean distance, which takes
1927 $\mathcal{O}(m)$, indicate that the computational complexity is $\mathcal{O}(n^2m)$. The space complexity is
1928 $\mathcal{O}(n^2)$ because of the pairwise distance of each subsequence with the other subsequence.
1929 However, the matrix profile can be computed in $\mathcal{O}(n^2)$ using an exact method, namely
1930 STOMP [86] or its community-open-sourced version, STUMP [88]. Besides, the running
1931 time can be further sped up by parallelization for a single machine with multiple compu-
1932 tation units, such as CPUs or GPUs. The tool also allows us to compute the left matrix
1933 profile to find the left nearest neighbor of each window. To note, the matrix profile an-
1934notates a time series with information about the nearest neighbor of each subsequence,
1935 including the similarity with its nearest neighbor and its location, as shown in Figure 5.2.
1936

In this study, we make the following contributions:

- 1937 • We are the first to propose leveraging the matrix profile to create meaningful co-
1938 variates that improve forecaster performance.

1939 The rest of this study is organized as follows. Section 5.2 presents the related-work.
1940 In Section 5.3, we introduce the necessary background knowledge, then introduce our
1941 method. Section 5.4 contains an empirical evaluation. Finally, we conclude this paper
1942 and provide future work in Section 5.5.

1943 5.2 Related Work

1944 Many methods have been developed for time series forecasting. Traditional methods in-
1945 clude rolling averages (RA), vector auto-regression (VAR) [73, 89], and auto-regressive
1946 integrated moving averages (ARIMA) [90, 91, 89]. Because of their rigorous statisti-
1947 cal properties, they have long been the standard. The shortcomings of ARIMA and
1948 its variants include their high computational cost [73]. In contrast, VAR is arguably
1949 the most widely used method, particularly in multivariate time series analysis, owing to
1950 its simplicity. However, most of these traditional approaches have certain limitations.
1951 They perform well when the data meet specific statistical assumptions, such as station-
1952 arity [92], which means that the mean and variance of the time series remain constant

over time. It motivates the community to develop machine learning methods, particularly deep learning methods for time series forecasting. Many deep learning models have been proposed, including RNN-based models, CNN-based models, GNN-based models, Transformer-based models, and compound models that incorporate different base models mentioned before [78]. The compound models are promising. For example, RNNs are well suited to capturing long-term dependencies, whereas CNNs are well suited to capturing short-term dependencies. A good way to improve performance is to compound them. For example, LSTnet [73] integrates CNN, RNN, and autoregressive [93] techniques to extract both short-term and long-term patterns. Using the occupancy rate of a freeway as an example [73] to explain these two patterns, the “short-term” patterns refer to the morning peaks against evening peaks, while the “long-term” patterns refer to the workday patterns against weekend patterns. Clearly, a good forecaster needs to capture and distinguish both kinds of patterns. Despite the superior performance deep learning methods have achieved, they tend to be overly complex, opaque, and incur high computational costs compared to traditional techniques.

5.3 Method

In this section, we first formulate the time series forecasting problem, followed by the evaluation method. We then explain how to use a Gradient Boosting Regression Tree (GBRT) for forecasting. Subsequently, we discuss how to leverage the nearest neighbors’ information of each subsequence to improve GBRT’s performance. Finally, we discuss how to compute those nearest neighbors using the Matrix Profile.

To begin, we define the data type of interest: time series.

Definition 10 (Time series). A *time series* $T = t_1, t_2, \dots, t_n$ is a sequence of real-valued numbers with length $= n$.

In Definition 10, T is a univariate time series where each entry is a scalar number. If each entry is a vector consisting of scalar numbers with size > 1 , T is a multivariate time series. A multivariate time series can be regarded as a sequence of vectors. It can also be represented as a vector of univariate time series, where each univariate time series is referred to as a channel. In a dataset with more than one time series, we use T_i to denote a time series in a dataset with N time series, where $1 \leq i \leq N$.

The local properties of T can be analyzed through its subsequences.

Definition 11 (Subsequence). A *subsequence* $T_{i,m} = t_i, t_{i+1}, \dots, t_{i+m-1} = t_{i:i+m-1}$ of a T is a sequence that consists of a continuous subset of the entries from T of length m starting from i .

1987 **5.3.1 Problem Formulation**

1988 Time series forecasting is the task of predicting h -future values $y_{t+1}, y_{t+2}, \dots, y_{t+h}$ of a
1989 target Y at the current time point t . In this study, there is only one target variable Y . h is
1990 the number of steps we want to predict in the future. The simplest case is one-step-ahead
1991 forecasting, where $h = 1$. The predicted value is denoted as \hat{y}_{t+1} where the actual value
1992 is y_{t+1} . It is preferable to predict multiple points in the future. It is called multi-horizon
1993 (multi-step) forecasting, where $h > 1$. The task of forecasting is encoded in Equation 5.1.

$$\hat{y}_{t+\tau} = f(y_{t-w+1:t}, x_{t-w+1:t}, u_{t-w+1:t+\tau}, \tau) \quad (5.1)$$

1994 where

- 1995 • $\hat{y}_{t+\tau}$ is a prediction of the target value at $t + \tau$, where $\tau \in \{1, 2, \dots, h\}$.
- 1996 • $y_{t-w+1:t}$ are the actual values consisting of the current value y_t and the lag values
1997 before it. y_{t-i} is called the lag of i or i -lag.
- 1998 • x_t are inputs that can only be known historically at time t . x_{t+1} is not known at t .
- 1999 • u_t are known inputs for all time. For example, the date information such as the
2000 day of the week or month [92]. Even at t , u_{t+i} where $1 \leq i \leq \infty$ are known.

2001 x_t and u_t are called covariates of y_t . The input of Equation 5.1 is a look-back window w .

2002 We explain the task of forecasting in terms of Equation 5.1. The forecasting process
2003 estimates the value of $y_{t+\tau}$, denoted by $\hat{y}_{t+\tau}$ with the aim to minimize the error function,
2004 typically represented as a function of $y_{t+\tau} - \hat{y}_{t+\tau}$ for each τ . It is obvious that date
2005 information is useful when the target variable depends on when the measurement is
2006 taken. For example, if the target variable is the electricity consumption rate, there is a
2007 clear pattern by month: consumption is higher during the winter and summer months,
2008 when air conditioners and heaters are used. x_t provides additional information about the
2009 state of y_t . For example, if the target variable is the body temperature, and x_t tells us
2010 the severity of the sore throat, we may guess the body temperature will raise tomorrow.

2011 **5.3.2 Evaluation Method**

2012 Given a dataset D of N time series T_i , where $1 \leq i \leq N$, we explain how to evaluate the
2013 performance of a forecaster on T_i . The error made by the forecaster on D is simply the
2014 summation of errors made by the forecaster on each T_i . We now focus on a single time
2015 series; hence, we drop the index i . T is divided into two subsequences, namely training
2016 subsequence T_{train} and test subsequence T_{test} .

2017 In our study, the forecaster is only allowed to train on T_{train} . Recall that we are
2018 predicting the h future values from the w values just before them. Hence, we use a

sliding window of length $w + h$ to generate the w -predictor- h -response pairs in T_{train} , enabling the forecaster to train on them. During the test (evaluation) phase, we do rolling forecasts. We predict based on the ground truth, not results generated from the model. It is used to prevent the accumulation of errors.

This concept is called “Teacher forcing” [94] because the teacher’s values are “force fed” into the forecaster when we “roll” the forecaster on the T_{test} [95]. The intuition is that, suppose each question (except the first one) in an exam depends on the answers to the previous questions, rather than simply grading every answer in the end, a teacher would grade (evaluate) the answer once it is given by the student, and provide the correct answer to the student so he can answer the next question based on the correct answer.

To evaluate the forecaster, we used the following three evaluation metrics defined as:

- Root Mean Square Error (RMSE)

$$\text{RMSE} = \sqrt{\frac{1}{n} \sum_{i=1}^n (y_i - \hat{y}_i)^2} \quad (5.2)$$

- Weighted Absolute Percentage Error (WAPE)

$$\text{WAPE} = \frac{\sum_{i=1}^n |y_i - \hat{y}_i|}{\sum_{i=1}^n |y_i|} \quad (5.3)$$

- Mean Absolute Error (MAE)

$$\text{MAE} = \frac{1}{n} \sum_{i=1}^n |y_i - \hat{y}_i| \quad (5.4)$$

where n is the length of the time series, y_i , \hat{y}_i is ground true value and predicted value, respectively. RMSE and MAE are widely used metrics. MAE can better reflect the actual error situation than RMSE [76]. WAPE was introduced by [96]. By rewriting Equation 5.3 to Equation 5.5, it is more obvious that it is a weighted absolute percentage error.

$$\text{WAPE} = \sum_{i=1}^n w_i \frac{|y_i - \hat{y}_i|}{|y_i|} \quad (5.5)$$

where the weights are given by

$$w_i = \frac{|y_i|}{\sum_{i=1}^n |y_i|} \quad (5.6)$$

For all of them, a lower value is better.

2040 5.3.3 Gradient Boosting Regression Tree (GBRT)

2041 Gradient boosting [97] is a boosting algorithm that ensembles a group of weak learners
2042 (usually decision trees) to make predictions. It sequentially adds learners to an ensemble,
2043 with each learner connecting its predecessor. It constructs weak learners in a way that
2044 each learner strategically corrects the predecessor’s mistakes by fitting the new learner
2045 to the residual errors made by the predecessor [98, 99]. It can be used in classification
2046 and regression. In this study, we focus on its use in regression. For the usage in regres-
2047 sion, the model is called “Gradient Boosting Regression Tree (GBRT)”. Some popular
2048 optimized implementations of gradient boosting are XGBoost [100], CatBoost [101], and
2049 LightGBM [102]. In this study, we use XGBoost.

2050 In order to apply GBRT into time series forecasting problem, we need to cast the
2051 input into an appropriate format to input into GBRT. The casting approach is similar to
2052 successful time-series forecasting models, which reconfigure the time series into windowed
2053 inputs [90]. Figure 5.1 presents the reconfiguration. For each entry of the target variable
2054 y_i , we retrieve its u_i , such as the day information from the calendar. Hence, for each y_i , it
2055 is associated with x_i and u_i . To simplify the notation, we absorb u_i into x_i , and it is called
2056 the covariates of y_i . The 2D window, as shown on the left-hand side in Figure 5.1, with
2057 size $w \times M$, where M is the total number of covariates, is flattened into a 1D array on the
2058 right-hand side with length $w + M$. To note, as suggested in the literature [90], only the
2059 covariates of the last time-point i are kept and appended to the final vector. By recon-
2060 figuration, we obtain the predictor-response pairs for training. In detail, the predictor is
2061 $y_{i-w+1}, y_{i-w+2}, \dots, y_i, x_i^1, x_i^2, \dots, x_i^M$ where the red part refers to the current target value
2062 y_i and its lag values, and the blue part refers to the covariates of y_i . The corresponding
2063 output is $y_{i+1}, y_{i+2}, \dots, y_{i+h}$, with length = h . We predict the h -horizon from the w -look
2064 back window (i.e., $w + M$ -flattened predictor). With this predictor-response formulation,
2065 the forecasting problem becomes a multi-output regression problem. Standard XGBoost
2066 cannot return a sequence of predicted values; it only returns a single number [90]. To
2067 note, a multi-output regression problem is simply a group of single-output regression
2068 problems. In other words, XGBoost internally simply treats the prediction of h -steps as
2069 h individual problems. Hence, the final output is produced by the h regressors rather
2070 than by a single model. One may argue that the h regressors operate individually and
2071 hence the temporal relationship in the output sequence is lost. However, as the individual
2072 regressors are trained on the same flattened input, the prediction would still preserve the
2073 temporal relationship [90].

5.3.4 Matrix Profile

2074

Definition 12 (Distance profile). A *distance profile* $D_i = d_{i,1}, d_{i,2}, \dots, d_{i,n-m+1}$ of a T is a vector of the Euclidean distances between a given subsequence $T_{i,m}$ and each subsequences in T , where $d_{i,j}$ is the distance between $T_{i,m}$ and $T_{j,m}$, $1 \leq i, j \leq n - m + 1$. 2075
2076
2077

The distances are measured between z-normalized time series. 2078

Definition 13 (Matrix profile). A *matrix profile* $P = \min(D_1), \min(D_2), \dots, \min(D_{n-m+1})$ of T is a vector of Euclidean distances between every subsequence $T_{i,m}$ of T and its nearest neighbor in T . 2079
2080
2081

Definition 14 (Matrix profile index). A *matrix profile index* $I = I_1, I_2, \dots, I_{n-m+1}$ of T is a vector of integers, where $I_i = j$ if $d_{i,j} = \min D_i$. 2082
2083

Definition 15 (Left distance profile). A *left distance profile* $D_i^L = d_{i,1}, d_{i,2}, \dots, d_{i,i-\lceil m/4 \rceil - 1}$ of T is a vector of Euclidean distances between a given subsequence $T_{i,m}$ and each subsequence that appears before $T_{i,m}$. To note, $i - \lceil m/4 \rceil - 1$ is the index location of the last eligible subsequence before $T_{i,m}$ because of the exclusion zone. 2084
2085
2086
2087

Definition 16 (Left matrix profile). A *left matrix profile* $P^L = \min(D_1^L), \min(D_2^L), \dots, \min(D_{n-m+1}^L)$ of T is a vector of Euclidean distances between every subsequence $T_{i,m}$ of T and its nearest neighbor in T before it. 2088
2089
2090

Definition 17 (Left matrix profile index). A *left matrix profile index* $I^L = I_1^L, I_2^L, \dots, I_{n-m+1}^L$ of T is a vector of integers, where $I_i^L = j$ if $d_{i,j} = \min D_i^L$. 2091
2092

5.4 Experiments

2093

Table 5.1: Dataset Statistics. N is the number of time series in the dataset, while $|T| = n$ is the length of each time series. “rate” refers to the measuring rate. w is the size of the look-back window. h is the size of the forecasting window, also known as the forecasting horizon. T_{train} is the training subsequence of T . T_{test} is the test subsequence of T . To note, $|T_{\text{train}}| + |T_{\text{test}}| = n$.

Dataset	Data			Forecasting Task		
	N	n	rate	w, h	$ T_{\text{train}} $	$ T_{\text{test}} $
Electricity [103]	70	26,136	hourly	24	25,968	168
Traffic [103]	90	10,560	hourly	24	10,392	168
PeMSD7(M) [103]	228	12,672	/5 mins	9	11,232	1,440
Exchange-Rate [73]	8	7,536	daily	24	6,048	1,488

2094 **5.5 Concluding Remarks**

2095 **5.5.1 Future Work**

2096 **Leveraging nearest neighbors' location information:** It would be beneficial to re-
2097 trieve the nearest neighbors for each subsequence in a specific range with respect to it.
2098 Real-world applications often require the separation of information of short-term and
2099 long-term repeating patterns for making accurate predictions [73]. Notably, the matrix
2100 profile also provides the locations of the nearest neighbors from the matrix profile in-
2101 dex. Using this location (index) information, we can retrieve the nearest neighbors of
2102 each subsequence in a specified range with respect to it to find those "short-term" and
2103 "long-term" patterns.

2104 **Extend to multidimensional case:** This study focuses on univariate time series fore-
2105 casting, where there is a single target and no exogenous inputs. It only requires us
2106 to find one-dimensional nearest neighbors. When there are multiple targets or a sin-
2107 gle target with multiple exogenous inputs, we need to identify multidimensional nearest
2108 neighbors [104] and leverage their information for forecasting.

2109 **Top- k motifs:** We can use motifs instead of neighbors to receive more stable "future"
2110 information for each window. Recall that a time series motif is a repeated pattern that
2111 consists of at least two occurrences. A motif can be considered as a family of nearest
2112 neighbors A nearest neighbor is a historical occurrence that instantiates this motif. The
2113 motif captures the ideal behavior. By finding the occurrences of a motif and considering
2114 their immediate subsequences, we can make a more confident guess about this motif. We
2115 outline the approach for finding members of a motif ¹ Given a subsequence A in a time
2116 series T , we denote the left-hand side of A in T as T_L . We find A 's nearest neighbor in
2117 T_L , denoted as B . They are the two members of a motif M . We want to identify other
2118 subsequences in T_L that belong to M . We define a threshold $\theta = r \times \text{ED}(A, B)$, where
2119 $r > 1$. The center M_C of M is defined as the average of A and B . Then, we compute
2120 the distance profile between M_C and T_L . Any part of the distance profile that is smarter
2121 than θ points to a member of M in T_L . These members can then be added to M . After
2122 identifying all the members of M and excluding these members in the next consideration,
2123 we can find the next left nearest neighbor of A in T_L , and repeat the same process for
2124 finding the next motif. Given a set of immediate subsequences of members (occurrences)
2125 of M , we can compute a more stable immediate subsequence (future) associated with M
2126 by excluding the outliers among them or using the ensemble value, such as the mean or
2127 median of them, to cancel the noise.

2128 **Identify outliers of immediate subsequences:** When we have a set of immediate
2129 subsequences, we can determine whether an immediate subsequence is an outlier or not

¹The idea has been mentioned in <https://www.cs.ucr.edu/~eamonn/TimeSeriesMotifs/>.

by comparing it with others. We provide a heuristic to identify an outlier as follows. 2130
 Recall that the length of a nearest neighbor and its immediate subsequence is m and h , 2131
 respectively. We concatenate all nearest neighbors into a single long time series T' . To 2132
 establish a clear boundary, we append a NaN value after each of them. It ensures that all 2133
 matrix profile computations do not consider subsequences that span multiple neighbors. 2134
 Then, we compute a distance profile of T' to find the nearest neighbor distance d_i of each 2135
 neighbor i . Let S_i be the sequence consisting of neighbor i of length m and its immediate 2136
 subsequence of length h . The expected nearest neighbor distance of S_i (found within the 2137
 set of all extended sequences) should be proportional to the increase in length: $d_i \times \frac{m+h}{m}$. 2138
 If the actual nearest neighbor distance of S_i is greater than $r' \times (d_i \times (m+h)/m)$ among 2139
 the others, where r' is a user-given value, the immediate subsequence in S_i is considered 2140
 as an outlier. 2141

Chapter 6

2142

Conclusion and Future Directions

2143

In this thesis, we contribute to time series analysis by addressing two aspects, with applications in bioinformatics. The first is to frame the prediction of biological sequence problems as time series classification tasks. The second addresses a fundamental limitation in existing time series distance measures.

2144
2145
2146
2147

In the first study, we investigate the prediction of human Dicer cleavage sites. This task is important for the biogenesis of microRNAs (miRNAs). Accurate prediction of Dicer cleavage sites is crucial for elucidating mechanisms of post-transcriptional gene regulation. Computationally, this task is a classification problem. First, we curate the dataset based on existing studies. The resulting datasets are 14-strings. Then, they are transformed into time series. We employ ROCKET-based classifiers for the classification. The main contributions are summarized as follows. We are the first to frame this problem as a multivariate time series classification problem. We introduced nine encoding methods for the transformation. In the transformation, to our surprise, we are the first to use the base-pair probabilities derived from the predicted secondary structure. We employ state-of-the-art time-series classifiers, namely ROCKET-based classifiers. They use random convolutional kernels to generate the summary statistics and then use a simple ridge classifier to generate the final results. Because of the simplicity of the transformation method and the classifiers we adopted, our framework, namely MTSCCleave, is fast. It achieved predictive performance comparable to or even better than deep learning-based state-of-the-art methods. Furthermore, MTSCCleave demonstrated substantial computational efficiency, with speedups ranging from 3.7X to 28.8X relative to existing methods. We carried out perturbation-based experiments to identify the subsequence that are important for the classification. We found that regions near the center of the pre-miRNA secondary structure are most critical for Dicer cleavage site determination. It aligns with the existing study. Future work for this study is as follows. We make use of the predicted secondary structure information to construct the complementary strand and the base pair probability sequence for the input strand. However, there is more than one predicted secondary structure for the given RNA sequence. One future work is to make

use of all potential secondary structures, each with its own pair probability sequence, and encode this data into a multivariate time series with more channels. Another area for future work is to use interpretable time series classifiers, such as those based on time series shapelets. By doing this, we can study which subsequence is critical for the definition of the classes, namely “5p cleav”, “5p non-cleav”, “3p leav”, and “3p non-cleav” because shapelets serve as the subsequence that has the most discriminating power between classes.

The second study develops a new distance measure framework, namely PSD. It aims to release a fundamental assumption that the prior studies have overlooked. There is only one scaling rate throughout the entire time series. However, there are much data that exhibits multiple rates. For example, human motion or music performance. They consist of phases. Each phase has its own expression rate. Existing distance measures cannot account for such variations. For example, DTW is designed for handling local distortions. US assumes that there is only one scaling factor in the whole series. To address this, we introduced the Piecewise Scaling Distance (PSD) framework, the first of its kind to account for multiple scaling factors. Recall that PSD is agnostic to the base measure we used. We can use any existing distance measure as the base measure. We studied the two instantiations of it. They are PSED (using Euclidean Distance as the base measure) and PSDTW (using DTW as the base measure). We provided an exact dynamic programming solution to compute PSD and three general ways to speed it up. In particular, we proposed a constrained version of it that limits the search space based on allowed segment lengths derived from scaling factor bounds. Besides, we use parallel computing and early abandoning to further accelerate it. For PSDTW, due to its quadratic complexity, we can further speed it up using lower-bounding techniques. Experiments show that PSD, and in particular PSED, perform best when the query contains multi-rate distortions, compared with ED, DTW and the other five DTW-based methods.

Future works on it are as follows. Currently, the number of segments P is given by users. It is preferable to develop a heuristic or algorithmic approach to automatically determine P . A simple heuristic is to test a range of possible P . Besides, while we have successfully applied a lower bound on PSDTW and accelerated it, the computational overhead of calculating a lower bound on PSED outweighs the pruning benefit and makes the computation slower eventually. Developing a specialized lower bound for PSED could further improve its running time. In addition, some existing works on speeding up DTW such as “incremental DTW” can reuse the accumulated cost matrix D . However, it is challenging to apply a similar method to USDTW and PSDTW due to time series interpolation.

The third study develops a new method to create covariates for time series data using the immediate subsequences of the left nearest neighbor of each forecasting windows. We

have studied the effect of the length of the immediate subsequences on the forecaster. ²²¹¹
Future work of this study includes finding nearest neighbors in a specific range to capture ²²¹²
the short pattern and long pattern, extending the framework to a multivariate time series ²²¹³
forecasting task, using motif family instead of simply top- k nearest neighbors, and how ²²¹⁴
to handle the outliers among the immediate subsequences. ²²¹⁵

Bibliography

2216

- [1] M. Middlehurst, P. Schäfer, and A. Bagnall, “Bake off redux: A review and experimental evaluation of recent time series classification algorithms,” *Data Mining and Knowledge Discovery*, vol. 38, no. 4, pp. 1958–2031, Jul. 2024. 2217
2218
2219
- [2] H. Sakoe and S. Chiba, “Dynamic programming algorithm optimization for spoken word recognition,” *IEEE Transactions on Acoustics, Speech, and Signal Processing*, vol. 26, no. 1, pp. 43–49, Feb. 1978. 2220
2221
2222
- [3] F. Itakura, “Minimum prediction residual principle applied to speech recognition,” *IEEE Transactions on Acoustics, Speech, and Signal Processing*, vol. 23, no. 1, pp. 67–72, Feb. 1975. 2223
2224
2225
- [4] E. J. Keogh and M. J. Pazzani, “Derivative Dynamic Time Warping,” in *Proceedings of the 2001 SIAM International Conference on Data Mining (SDM)*, ser. 2226
2227
Proceedings. Society for Industrial and Applied Mathematics, Apr. 2001, pp. 1–11. 2228
- [5] Y.-S. Jeong, M. K. Jeong, and O. A. Omitaomu, “Weighted dynamic time warping 2229
for time series classification,” *Pattern Recognition*, vol. 44, no. 9, pp. 2231–2240, 2230
Sep. 2011. 2231
- [6] J. Zhao and L. Itti, “shapeDTW: Shape Dynamic Time Warping,” *Pattern Recognition*, vol. 74, pp. 171–184, Feb. 2018. 2232
2233
- [7] E. Keogh, K. Chakrabarti, M. Pazzani, and S. Mehrotra, “Dimensionality Reduction 2234
for Fast Similarity Search in Large Time Series Databases,” *Knowledge and 2235
Information Systems*, vol. 3, no. 3, pp. 263–286, Aug. 2001. 2236
- [8] B.-K. Yi and C. Faloutsos, “Fast Time Sequence Indexing for Arbitrary L_p Norms,” 2237
in *Proceedings of the 26th International Conference on Very Large Data Bases*, ser. 2238
VLDB ’00. San Francisco, CA, USA: Morgan Kaufmann Publishers Inc., Sep. 2239
2000, pp. 385–394. 2240
- [9] J. Zhao and L. Itti, “Decomposing time series with application to temporal seg- 2241
mentation,” in *2016 IEEE Winter Conference on Applications of Computer Vision 2242
(WACV)*, Mar. 2016, pp. 1–9. 2243

- 2244 [10] M. Herrmann and G. I. Webb, "Amercing: An intuitive and effective constraint for
2245 dynamic time warping," *Pattern Recognition*, vol. 137, p. 109333, May 2023.
- 2246 [11] L. A. Urry, M. L. Cain, S. A. Wasserman, P. V. Minorsky, R. B. Orr, and N. A.
2247 Campbell, *Campbell Biology*, twelfth ed. New York, NY: Pearson, 2020.
- 2248 [12] B. Alberts, *Molecular Biology of the Cell*, 7th ed. New York: W. W. Norton &
2249 Company, 2022.
- 2250 [13] W. W. Cohen, *A Computer Scientist's Guide to Cell Biology: A Travelogue from a*
2251 *Stranger in a Strange Land*. New York, NY: Springer-Verl, 2007.
- 2252 [14] Y. Lee, K. Jeon, J.-T. Lee, S. Kim, and V. N. Kim, "MicroRNA maturation:
2253 Stepwise processing and subcellular localization," *The EMBO Journal*, vol. 21,
2254 no. 17, pp. 4663–4670, Sep. 2002.
- 2255 [15] S. Gu, L. Jin, Y. Zhang, Y. Huang, F. Zhang, P. N. Valdmanis, and M. A. Kay,
2256 "The Loop Position of shRNAs and Pre-miRNAs Is Critical for the Accuracy of
2257 Dicer Processing In Vivo," *Cell*, vol. 151, no. 4, pp. 900–911, Nov. 2012.
- 2258 [16] Y. Feng, X. Zhang, P. Graves, and Y. Zeng, "A comprehensive analysis of precursor
2259 microRNA cleavage by human Dicer," *RNA*, vol. 18, no. 11, pp. 2083–2092, Nov.
2260 2012.
- 2261 [17] I. J. MacRae, K. Zhou, and J. A. Doudna, "Structural determinants of RNA recogni-
2262 tion and cleavage by Dicer," *Nature Structural & Molecular Biology*, vol. 14,
2263 no. 10, pp. 934–940, Oct. 2007.
- 2264 [18] F. Ahmed, R. Kaundal, and G. P. Raghava, "PHDcleav: A SVM based method for
2265 predicting human Dicer cleavage sites using sequence and secondary structure of
2266 miRNA precursors," *BMC Bioinformatics*, vol. 14, no. 14, p. S9, Oct. 2013.
- 2267 [19] Y. Bao, M. Hayashida, and T. Akutsu, "LBSizeCleav: Improved support vector
2268 machine (SVM)-based prediction of Dicer cleavage sites using loop/bulge length,"
2269 *BMC Bioinformatics*, vol. 17, no. 1, p. 487, Nov. 2016.
- 2270 [20] P. Liu, J. Song, C.-Y. Lin, and T. Akutsu, "ReCGBM: A gradient boosting-based
2271 method for predicting human dicer cleavage sites," *BMC Bioinformatics*, vol. 22,
2272 no. 1, p. 63, Feb. 2021.
- 2273 [21] L. Mu, J. Song, T. Akutsu, and T. Mori, "DiCleave: A deep learning model for
2274 predicting human Dicer cleavage sites," *BMC Bioinformatics*, vol. 25, no. 1, p. 13,
2275 Jan. 2024.

- [22] L. Mu and T. Akutsu, “DiCleavePlus: A Transformer-Based Model to Detect Human Dicer Cleavage Sites Within Cleavage Patterns,” *Genes to Cells*, vol. 31, no. 1, p. e70074, 2026. 2276
2277
2278
- [23] S. Griffiths-Jones, H. K. Saini, and S. van Dongen, “miRBase: Tools for microRNA 2279
genomics,” *Nucleic Acids Research*, vol. 36, no. suppl_1, pp. D154–D158, Jan. 2008. 2280
- [24] T. Xu, N. Su, L. Liu, J. Zhang, H. Wang, W. Zhang, J. Gui, K. Yu, J. Li, and T. D. 2281
Le, “miRBaseConverter: An R/Bioconductor package for converting and retrieving 2282
miRNA name, accession, sequence and family information in different versions of 2283
miRBase,” *BMC Bioinformatics*, vol. 19, no. 19, p. 514, Dec. 2018. 2284
- [25] M. J. Zvelebil, J. O. Baum, and M. Zvelebil, *Understanding Bioinformatics*. New 2285
York: Garland Science, 2008. 2286
- [26] R. Lorenz, S. H. Bernhart, C. Höner zu Siederdissen, H. Tafer, C. Flamm, P. F. 2287
Stadler, and I. L. Hofacker, “ViennaRNA Package 2.0,” *Algorithms for Molecular 2288
Biology*, vol. 6, no. 1, p. 26, Nov. 2011. 2289
- [27] C. C. Aggarwal, *Data Mining: The Textbook*. Cham: Springer International Pub- 2290
lishing, 2015. 2291
- [28] G. Mendizabal-Ruiz, I. Román-Godínez, S. Torres-Ramos, R. A. Salido-Ruiz, and 2292
J. A. Morales, “On DNA numerical representations for genomic similarity compu- 2293
tation,” *PLOS ONE*, vol. 12, no. 3, p. e0173288, Mar. 2017. 2294
- [29] D. Anastassiou, “Genomic signal processing,” *IEEE Signal Processing Magazine*, 2295
vol. 18, no. 4, pp. 8–20, Jul. 2001. 2296
- [30] T. Rakthanmanon, B. Campana, A. Mueen, G. Batista, B. Westover, Q. Zhu, J. Za- 2297
karia, and E. Keogh, “Searching and mining trillions of time series subsequences 2298
under dynamic time warping,” in *Proceedings of the 18th ACM SIGKDD Interna- 2299
tional Conference on Knowledge Discovery and Data Mining*, ser. KDD ’12. New 2300
York, NY, USA: Association for Computing Machinery, Aug. 2012, pp. 262–270. 2301
- [31] P. D. Cristea, “Conversion of nucleotides sequences into genomic signals,” *Journal 2302
of Cellular and Molecular Medicine*, vol. 6, no. 2, pp. 279–303, 2002. 2303
- [32] N. Chakravarthy, A. Spanias, L. D. Iasemidis, and K. Tsakalis, “Autoregressive 2304
Modeling and Feature Analysis of DNA Sequences,” *EURASIP Journal on Ad- 2305
vances in Signal Processing*, vol. 2004, no. 1, pp. 1–16, Dec. 2004. 2306
- [33] J. Zhao, X. W. Yang, J. P. Li, and Y. Y. Tang, “DNA Sequences Classification 2307
Based on Wavelet Packet Analysis,” in *Wavelet Analysis and Its Applications*. 2308
Springer, Berlin, Heidelberg, 2001, pp. 424–429. 2309

- 2310 [34] T. Holden, R. Subramaniam, R. Sullivan, E. Cheung, C. Schneider, G. T. Jr,
2311 A. Flamholz, D. H. Lieberman, and T. D. Cheung, “ATCG nucleotide fluctuation
2312 of *Deinococcus radiodurans* radiation genes,” in *Instruments, Methods, and*
2313 *Missions for Astrobiology X*, vol. 6694. SPIE, Oct. 2007, pp. 402–411.
- 2314 [35] A. S. Nair and S. P. Sreenadhan, “A coding measure scheme employing electron-
2315 ion interaction pseudopotential (EIIP),” *Bioinformation*, vol. 1, no. 6, pp. 197–202,
2316 Oct. 2006.
- 2317 [36] M. Akhtar, J. Epps, and E. Ambikairajah, “On DNA Numerical Representations
2318 for Period-3 Based Exon Prediction,” in *2007 IEEE International Workshop on*
2319 *Genomic Signal Processing and Statistics*, Jun. 2007, pp. 1–4.
- 2320 [37] R. Zhang and C.-T. Zhang, “Z Curves, An Intutive Tool for Visualizing and An-
2321 alyzing the DNA Sequences,” *Journal of Biomolecular Structure and Dynamics*,
2322 vol. 11, no. 4, pp. 767–782, Feb. 1994.
- 2323 [38] J. A. Berger, S. K. Mitra, M. Carli, and A. Neri, “Visualization and analysis of DNA
2324 sequences using DNA walks,” *Journal of the Franklin Institute*, vol. 341, no. 1, pp.
2325 37–53, Jan. 2004.
- 2326 [39] A. Bagnall, J. Lines, A. Bostrom, J. Large, and E. Keogh, “The great time series
2327 classification bake off: A review and experimental evaluation of recent algorithmic
2328 advances,” *Data Mining and Knowledge Discovery*, vol. 31, no. 3, pp. 606–660, May
2329 2017.
- 2330 [40] A. P. Ruiz, M. Flynn, J. Large, M. Middlehurst, and A. Bagnall, “The great multi-
2331 variate time series classification bake off: A review and experimental evaluation
2332 of recent algorithmic advances,” *Data Mining and Knowledge Discovery*, vol. 35,
2333 no. 2, pp. 401–449, Mar. 2021.
- 2334 [41] A. Dempster, F. Petitjean, and G. I. Webb, “ROCKET: Exceptionally fast and
2335 accurate time series classification using random convolutional kernels,” *Data Mining*
2336 and *Knowledge Discovery*, vol. 34, no. 5, pp. 1454–1495, Sep. 2020.
- 2337 [42] A. Dempster, D. F. Schmidt, and G. I. Webb, “MiniRocket: A Very Fast (Almost)
2338 Deterministic Transform for Time Series Classification,” in *Proceedings of the 27th*
2339 *ACM SIGKDD Conference on Knowledge Discovery & Data Mining*, ser. KDD
2340 ’21. New York, NY, USA: Association for Computing Machinery, Aug. 2021, pp.
2341 248–257.
- 2342 [43] C. W. Tan, A. Dempster, C. Bergmeir, and G. I. Webb, “MultiRocket: Multiple
2343 pooling operators and transformations for fast and effective time series classifica-

- tion,” *Data Mining and Knowledge Discovery*, vol. 36, no. 5, pp. 1623–1646, Sep. 2022. 2344
2345
- [44] A. Dempster, D. F. Schmidt, and G. I. Webb, “Hydra: Competing convolutional 2346
kernels for fast and accurate time series classification,” *Data Mining and Knowledge 2347
Discovery*, vol. 37, no. 5, pp. 1779–1805, Sep. 2023. 2348
- [45] B. W. Matthews, “Comparison of the predicted and observed secondary structure 2349
of T4 phage lysozyme,” *Biochimica et Biophysica Acta (BBA) - Protein Structure*, 2350
vol. 405, no. 2, pp. 442–451, Oct. 1975. 2351
- [46] J. Gorodkin, “Comparing two K-category assignments by a K-category correlation 2352
coefficient,” *Computational Biology and Chemistry*, vol. 28, no. 5, pp. 367–374, Dec. 2353
2004. 2354
- [47] T.-c. Fu, “A review on time series data mining,” *Engineering Applications of Arti- 2355
ficial Intelligence*, vol. 24, no. 1, pp. 164–181, Feb. 2011. 2356
- [48] C. Rose, B. Guenter, B. Bodenheimer, and M. F. Cohen, “Efficient generation of 2357
motion transitions using spacetime constraints,” in *Proceedings of the 23rd Annual 2358
Conference on Computer Graphics and Interactive Techniques*, ser. SIGGRAPH 2359
'96. New York, NY, USA: Association for Computing Machinery, Aug. 1996, pp. 2360
147–154. 2361
- [49] Y. Li, T. Wang, and H.-Y. Shum, “Motion texture: A two-level statistical model 2362
for character motion synthesis,” *ACM Trans. Graph.*, vol. 21, no. 3, pp. 465–472, 2363
Jul. 2002. 2364
- [50] R. B. Dannenberg, W. P. Birmingham, G. P. Tzanetakis, C. P. Meek, N. P. Hu, 2365
and B. P. Pardo, “The MUSART Testbed for Query-by-Humming Evaluation,” 2366
Comput. Music J., vol. 28, no. 2, pp. 34–48, Jun. 2004. 2367
- [51] K.-C. Li, M. Yan, and S. Yuan, “A Simple Statistical Model for Depicting the 2368
Cdc15-Synchronized Yeast Cell-Cycle Regulated Gene Expression Data,” *Statistica 2369
Sinica*, vol. 12, no. 1, pp. 141–158, 2002. 2370
- [52] G. E. A. P. A. Batista, E. J. Keogh, O. M. Tataw, and V. M. A. de Souza, “CID: An 2371
efficient complexity-invariant distance for time series,” *Data Mining and Knowledge 2372
Discovery*, vol. 28, no. 3, pp. 634–669, May 2014. 2373
- [53] A. W.-C. Fu, E. Keogh, L. Y. H. Lau, C. A. Ratanamahatana, and R. C.-W. Wong, 2374
“Scaling and time warping in time series querying,” *The VLDB Journal*, vol. 17, 2375
no. 4, pp. 899–921, Jul. 2008. 2376

- 2377 [54] Y. Shen, Y. Chen, E. Keogh, and H. Jin, “Searching Time Series with Invariance to
 2378 Large Amounts of Uniform Scaling,” in *2017 IEEE 33rd International Conference*
 2379 *on Data Engineering (ICDE)*, Apr. 2017, pp. 111–114.
- 2380 [55] ——, “Accelerating Time Series Searching with Large Uniform Scaling,” in *Proceedings of the 2018 SIAM International Conference on Data Mining (SDM)*, ser.
 2381 Proceedings. Society for Industrial and Applied Mathematics, May 2018, pp.
 2382 234–242.
- 2383 [56] C. C. Aggarwal and C. K. Reddy, Eds., *Data Clustering: Algorithms and Applications*, 1st ed. Boca Raton: Chapman and Hall/CRC, Aug. 2013.
- 2384 [57] P. Esling and C. Agon, “Time-series data mining,” *ACM Computing Surveys*,
 2385 vol. 45, no. 1, pp. 1–34, Nov. 2012.
- 2386 [58] T. Rakthanmanon, B. Campana, A. Mueen, G. Batista, B. Westover, Q. Zhu,
 2387 J. Zakaria, and E. Keogh, “Addressing Big Data Time Series: Mining Trillions of
 2388 Time Series Subsequences Under Dynamic Time Warping,” *ACM Trans. Knowl.
 2389 Discov. Data*, vol. 7, no. 3, pp. 10:1–10:31, Sep. 2013.
- 2390 [59] C. W. Tan, F. Petitjean, and G. I. Webb, “Elastic bands across the path: A new
 2391 framework and method to lower bound DTW,” in *Proceedings of the 2019 SIAM
 2392 International Conference on Data Mining (SDM)*, ser. Proceedings. Society for
 2393 Industrial and Applied Mathematics, May 2019, pp. 522–530.
- 2394 [60] A. Shifaz, C. Pelletier, F. Petitjean, and G. I. Webb, “Elastic similarity and distance
 2395 measures for multivariate time series,” *Knowledge and Information Systems*, vol. 65,
 2396 no. 6, pp. 2665–2698, Jun. 2023.
- 2397 [61] S. Salvador and P. Chan, “Toward accurate dynamic time warping in linear time
 2398 and space,” *Intelligent Data Analysis*, vol. 11, no. 5, pp. 561–580, Oct. 2007.
- 2399 [62] E. Keogh, T. Palpanas, V. B. Zordan, D. Gunopoulos, and M. Cardle, “Indexing large
 2400 human-motion databases,” in *Proceedings of the Thirtieth International Conference*
 2401 *on Very Large Data Bases - Volume 30*, ser. VLDB ’04. Toronto, Canada: VLDB
 2402 Endowment, Aug. 2004, pp. 780–791.
- 2403 [63] D. Yankov, E. Keogh, J. Medina, B. Chiu, and V. Zordan, “Detecting time series
 2404 motifs under uniform scaling,” in *Proceedings of the 13th ACM SIGKDD Interna-*
 2405 *tional Conference on Knowledge Discovery and Data Mining*, ser. KDD ’07. New
 2406 York, NY, USA: Association for Computing Machinery, Aug. 2007, pp. 844–853.
- 2407 [64] Y. Zhu and D. Shasha, “Warping indexes with envelope transforms for query by
 2408 humming,” in *Proceedings of the 2003 ACM SIGMOD International Conference on*

- Management of Data*, ser. SIGMOD '03. New York, NY, USA: Association for Computing Machinery, Jun. 2003, pp. 181–192. 2411
2412
- [65] E. Keogh and C. A. Ratanamahatana, “Exact indexing of dynamic time warping,” 2413
Knowledge and Information Systems, vol. 7, no. 3, pp. 358–386, Mar. 2005. 2414
- [66] S.-W. Kim, S. Park, and W. Chu, “An index-based approach for similarity search 2415
supporting time warping in large sequence databases,” in *Proceedings 17th Interna- 2416
tional Conference on Data Engineering*, Apr. 2001, pp. 607–614. 2417
- [67] C. W. Tan, M. Herrmann, G. Forestier, G. I. Webb, and F. Petitjean, “Efficient 2418
search of the best warping window for Dynamic Time Warping,” in *Proceedings of 2419
the 2018 SIAM International Conference on Data Mining (SDM)*, ser. Proceedings. 2420
Society for Industrial and Applied Mathematics, May 2018, pp. 225–233. 2421
- [68] C. A. Ratanamahatana and E. Keogh, “Everything you know about Dynamic Time 2422
Warping is Wrong,” in *3 Rd International Workshop on Mining Temporal and 2423
Sequential Data (TDM-04)*. Citeseer, 2004. 2424
- [69] H. A. Dau, A. Bagnall, K. Kamgar, C.-C. M. Yeh, Y. Zhu, S. Gharghabi, C. A. 2425
Ratanamahatana, and E. Keogh, “The UCR time series archive,” *IEEE/CAA Jour- 2426
nal of Automatica Sinica*, vol. 6, no. 6, pp. 1293–1305, Nov. 2019. 2427
- [70] M. Middlehurst, A. Ismail-Fawaz, A. Guillaume, C. Holder, D. Guijo-Rubio, G. Bu- 2428
latova, L. Tsaprounis, L. Mentel, M. Walter, P. Schäfer, and A. Bagnall, “Aeon: 2429
A Python Toolkit for Learning from Time Series,” *Journal of Machine Learning 2430
Research*, vol. 25, no. 289, pp. 1–10, 2024. 2431
- [71] N. Tatbul, T. J. Lee, S. Zdonik, M. Alam, and J. Gottschlich, “Precision and Recall 2432
for Time Series,” in *Advances in Neural Information Processing Systems*, vol. 31. 2433
Curran Associates, Inc., 2018. 2434
- [72] M. Leodolter, C. Plant, and N. Brändle, “IncDTW: An R Package for Incremental 2435
Calculation of Dynamic Time Warping,” *Journal of Statistical Software*, vol. 99, 2436
pp. 1–23, Sep. 2021. 2437
- [73] G. Lai, W.-C. Chang, Y. Yang, and H. Liu, “Modeling Long- and Short-Term 2438
Temporal Patterns with Deep Neural Networks,” in *The 41st International ACM 2439
SIGIR Conference on Research & Development in Information Retrieval*, ser. SIGIR 2440
'18. New York, NY, USA: Association for Computing Machinery, Jun. 2018, pp. 2441
95–104. 2442
- [74] C. Chatfield, *The Analysis of Time Series: An Introduction*, Sixth ed. 2443
New York: Chapman and Hall/CRC, Jul. 2003. 2444

- 2445 [75] O. Y. Al-Jarrah, P. D. Yoo, S. Muhaidat, G. K. Karagiannidis, and K. Taha,
2446 “Efficient Machine Learning for Big Data: A Review,” *Big Data Research*, vol. 2,
2447 no. 3, pp. 87–93, Sep. 2015.
- 2448 [76] W. Li and K. L. E. Law, “Deep Learning Models for Time Series Forecasting: A
2449 Review,” *IEEE Access*, vol. 12, pp. 92 306–92 327, 2024.
- 2450 [77] N. I. Sapankevych and R. Sankar, “Time Series Prediction Using Support Vector
2451 Machines: A Survey,” *IEEE Computational Intelligence Magazine*, vol. 4, no. 2,
2452 pp. 24–38, May 2009.
- 2453 [78] Z. Chen, M. Ma, T. Li, H. Wang, and C. Li, “Long sequence time-series forecasting
2454 with deep learning: A survey,” *Information Fusion*, vol. 97, p. 101819, Sep. 2023.
- 2455 [79] J. F. Torres, D. Hadjout, A. Sebaa, F. Martínez-Álvarez, and A. Troncoso, “Deep
2456 Learning for Time Series Forecasting: A Survey,” *Big Data*, vol. 9, no. 1, pp. 3–21,
2457 Feb. 2021.
- 2458 [80] D. B. da Silva, D. Schmidt, C. A. da Costa, R. da Rosa Righi, and B. Eskofier,
2459 “DeepSigns: A predictive model based on Deep Learning for the early detection of
2460 patient health deterioration,” *Expert Systems with Applications*, vol. 165, p. 113905,
2461 Mar. 2021.
- 2462 [81] N. Wu, B. Green, X. Ben, and S. O’Banion, “Deep Transformer Models for Time
2463 Series Forecasting: The Influenza Prevalence Case,” Jan. 2020.
- 2464 [82] F. Martínez-Álvarez, G. Asencio-Cortés, J. F. Torres, D. Gutiérrez-Avilés,
2465 L. Melgar-García, R. Pérez-Chacón, C. Rubio-Escudero, J. C. Riquelme, and
2466 A. Troncoso, “Coronavirus Optimization Algorithm: A Bioinspired Metaheuristic
2467 Based on the COVID-19 Propagation Model,” *Big Data*, vol. 8, no. 4, pp. 308–322,
2468 Aug. 2020.
- 2469 [83] F. Martínez, M. P. Frías, M. D. Pérez, and A. J. Rivera, “A methodology for ap-
2470 plying k-nearest neighbor to time series forecasting,” *Artificial Intelligence Review*,
2471 vol. 52, no. 3, pp. 2019–2037, Oct. 2019.
- 2472 [84] S. Tajmouati, B. E. L. Wahbi, A. Bedoui, A. Abarda, and M. Dakkon, “Applying
2473 k-nearest neighbors to time series forecasting: Two new approaches,” *Journal of
2474 Forecasting*, vol. 43, no. 5, pp. 1559–1574, 2024.
- 2475 [85] D. T. Thi, N. T. Phong, and N. D. Bui, “Forecast Timeseries Based On Matrix
2476 Profile,” *Journal of Informatics and Innovative Technologies (JIIT)*, 2021.

- [86] C.-C. M. Yeh, Y. Zhu, L. Ulanova, N. Begum, Y. Ding, H. A. Dau, D. F. Silva, A. Mueen, and E. Keogh, “Matrix Profile I: All Pairs Similarity Joins for Time Series: A Unifying View That Includes Motifs, Discords and Shapelets,” in *2016 IEEE 16th International Conference on Data Mining (ICDM)*. Barcelona, Spain: IEEE, Dec. 2016, pp. 1317–1322. 2477
- [87] Y. Zhu, M. Imamura, D. Nikovski, and E. Keogh, “Matrix Profile VII: Time Series Chains: A New Primitive for Time Series Data Mining,” in *2017 IEEE International Conference on Data Mining (ICDM)*, Nov. 2017, pp. 695–704. 2482
2483
2484
- [88] S. M. Law, “STUMPY: A Powerful and Scalable Python Library for Time Series Data Mining,” *Journal of Open Source Software*, vol. 4, no. 39, p. 1504, Jul. 2019. 2485
2486
- [89] G. E. P. Box, G. M. Jenkins, G. C. Reinsel, and G. M. Ljung, *Time Series Analysis: Forecasting and Control*. John Wiley & Sons, May 2015. 2487
2488
- [90] S. Elsayed, D. Thyssens, A. Rashed, H. S. Jomaa, and L. Schmidt-Thieme, “Do We Really Need Deep Learning Models for Time Series Forecasting?” Oct. 2021. 2489
2490
- [91] G. E. P. Box and D. A. Pierce, “Distribution of Residual Autocorrelations in Autoregressive-Integrated Moving Average Time Series Models,” *Journal of the American Statistical Association*, vol. 65, no. 332, pp. 1509–1526, 1970. 2491
2492
2493
- [92] B. Lim and S. Zohren, “Time-series forecasting with deep learning: A survey,” *Philosophical Transactions of the Royal Society A: Mathematical, Physical and Engineering Sciences*, vol. 379, no. 2194, p. 20200209, Feb. 2021. 2494
2495
2496
- [93] G. U. Yule, “On a Method of Investigating Periodicities in Disturbed Series, with Special Reference to Wolfer’s Sunspot Numbers,” *Philosophical Transactions of the Royal Society of London. Series A, Containing Papers of a Mathematical or Physical Character*, vol. 226, pp. 267–298, 1927. 2497
2498
2499
2500
- [94] R. J. Williams and D. Zipser, “A Learning Algorithm for Continually Running Fully Recurrent Neural Networks,” *Neural Computation*, vol. 1, no. 2, pp. 270–280, Jun. 1989. 2501
2502
2503
- [95] K. P. Murphy, *Probabilistic Machine Learning: An Introduction*, ser. Adaptive Computation and Machine Learning. Cambridge, Massachusetts London, England: The MIT Press, 2022. 2504
2505
2506
- [96] S. Kolassa and W. Schütz, “Advantages of the MAD/Mean Ratio over the MAPE,” *Foresight: The International Journal of Applied Forecasting*, vol. 6, pp. 40–43, 2007. 2507
2508

- 2509 [97] J. H. Friedman, “Greedy function approximation: A gradient boosting machine.”
- 2510 *The Annals of Statistics*, vol. 29, no. 5, pp. 1189–1232, Oct. 2001.
- 2511 [98] L. G. Serrano and S. Thrun, *Grokking Machine Learning*. Shelter Island: Manning,
- 2512 2021.
- 2513 [99] A. Géron, *Hands-On Machine Learning with Scikit-Learn and PyTorch: Concepts,*
- 2514 *Tools, and Techniques to Build Intelligent Systems*. US: O'Reilly Media, 2025.
- 2515 [100] T. Chen and C. Guestrin, “XGBoost: A Scalable Tree Boosting System,” in *Proceedings of the 22nd ACM SIGKDD International Conference on Knowledge Discovery and Data Mining*, ser. KDD ’16. New York, NY, USA: Association for Computing Machinery, Aug. 2016, pp. 785–794.
- 2519 [101] A. V. Dorogush, V. Ershov, and A. Gulin, “CatBoost: Gradient boosting with
- 2520 categorical features support,” in *Workshop on ML Systems at NIPS 2017*, 2017.
- 2521 [102] G. Ke, Q. Meng, T. Finley, T. Wang, W. Chen, W. Ma, Q. Ye, and T.-Y. Liu,
- 2522 “LightGBM: A Highly Efficient Gradient Boosting Decision Tree,” in *Advances in*
- 2523 *Neural Information Processing Systems*, vol. 30. Curran Associates, Inc., 2017.
- 2524 [103] R. Sen, H.-F. Yu, and I. S. Dhillon, “Think Globally, Act Locally: A Deep Neural
- 2525 Network Approach to High-Dimensional Time Series Forecasting,” in *Advances in*
- 2526 *Neural Information Processing Systems*, vol. 32. Curran Associates, Inc., 2019.
- 2527 [104] C.-C. M. Yeh, N. Kavantzas, and E. Keogh, “Matrix Profile VI: Meaningful Multi-
- 2528 dimensional Motif Discovery,” in *2017 IEEE International Conference on Data*
- 2529 *Mining (ICDM)*, Nov. 2017, pp. 565–574.